Oxford Open Materials Science, 2022, 2(1): itac004

https://doi.org/10.1093/oxfmat/itac004
Advance Access Publication Date: 5 May 2022
Review

REVIEW

A review of ultrawide bandgap materials: properties, synthesis and devices

Mingfei Xu [1,†], Dawei Wang[2,†], Kai Fu[1,†], Dinusha Herath Mudiyanselage[2], Houqiang Fu[2] and Yuji Zhao [1,*]

[1]Department of Electrical and Computer Engineering, Rice University, Houston, TX 77005, USA and
[2]Department of Electrical and Computer Engineering, Iowa State University, Ames, IA 50011, USA

[*]Correspondence address. Department of Electrical and Computer Engineering, Rice University, Brockman Hall 338, Rice University, Houston, TX 77005, USA. Tel: 713-348-4392; fax: 713-348-5686; E-mail: yuji.zhao@rice.edu

[†]These authors contributed equally to this work as co-first authors

Abstract

Ultrawide bandgap (UWBG) materials such as diamond, Ga_2O_3, hexagonal boron nitride (h-BN) and AlN, are a new class of semiconductors that possess a wide range of attractive properties, including very large bandgap, high critical electric field, high carrier mobility and chemical inertness. Due to these outstanding characteristics, UWBG materials are promising candidates to enable high-performance devices for power electronics, ultraviolet photonics, quantum sensing and quantum computing applications. Despite their great potential, the research of UWBG semiconductors is still at a nascent stage and represents a challenging interdisciplinary research area of physics, materials science and devices engineering. In this review, the material properties, synthesis methods and device applications of UWBG semiconductors diamond, Ga_2O_3, h-BN and AlN will be presented and their recent progress, challenges and research opportunities will be discussed.

Key words: ultrawide bandgap materials; diamond; Ga_2O_3; h-BN; AlN; doping; power electronics; quantum technologies.

INTRODUCTION

Since the invention of transistors in 1947, the semiconductor community has witnessed the emergence of three generations of semiconductor materials that are driving our modern society, from the first-generation semiconductors such as Si and Ge to the second-generation semiconductors such as GaAs and InP [1], to the recent third-generation wide bandgap (WBG) materials such as GaN and SiC. In the last three decades, technologies for WBG materials have been advancing closer to maturity with successful commercialization in applications of light-emitting diodes (LEDs), RF electronics and power electronics [2, 3]. However, the WBG semiconductor-based devices are approaching the theoretical limit of their achievable performance. To be prepared for the future demanding electronic and photonic applications, the semiconductor community is investigating the next-frontier devices based on ultra WBG (UWBG) semiconductors, such as diamond, Ga_2O_3, Hexagonal boron nitride (h-BN) and AlN. Due to their unique material properties, including UWBG, ultrahigh critical electric field and chemical inertness, UWBG semiconductors have garnered considerable research interest in power conversions, RF amplifiers, quantum computing, quantum photonics and extreme-environment devices (e.g. radiation and high temperature). Diamond is an exceptional material for high-voltage, high-temperature and high-frequency applications due to its high electron and hole mobility and high thermal conductivity [4]. In addition, the diamond nitrogen-vacancy (NV) center is the leading candidate for qubits in quantum computing. With the availability of large-size high-quality melt-grown bulk substrates and versatile epitaxial thin-film growth methods, Ga_2O_3 is currently extensively researched

Submitted: 4 February 2022; **Received (in revised form):** 5 April 2022. **Accepted:** 5 April 2022

© The Author(s) 2022. Published by Oxford University Press.
This is an Open Access article distributed under the terms of the Creative Commons Attribution License (https://creativecommons.org/licenses/by/4.0/), which permits unrestricted reuse, distribution, and reproduction in any medium, provided the original work is properly cited.

Downloaded from https://academic.oup.com/ooms/article/2/1/itac004/6581087 by guest on 04 August 2022

for power, RF and deep ultraviolet (DUV) devices. BN possesses extraordinary electrical, optical, thermal and mechanical properties. It can serve as both passive components in devices such as dielectric layers, substrates and encapsulation materials and device active regions for various photonic [e.g. DUV, nonlinear optics and single-photon emission (SPE)] and electronic applications. Low thermal conductivity and electron mobility can be constraining factors for Ga_2O_3 electronics, where innovative materials and devices engineering have been proposed to mitigate these issues. AlN has the largest bandgap among the UWBG semiconductor family with large thermal conductivity, strong piezoelectric coefficient, high chemical stability and compatibility with traditional complementary metal-oxide semiconductor (CMOS) manufacturing. For electronics, AlN-based flexible electronics and power transistors and diodes have been demonstrated [5, 6]. For photonics, AlN point defect-based single-photon emitters and waveguides can be integrated on AlN-on-sapphire flatform for photonic integrated circuits (PICs). In this review, we will discuss the material properties, synthesis, devices and applications of diamond, Ga_2O_3, h-BN and AlN, and present the recent progress, challenges and opportunities in these UWBG semiconductors.

PART I DIAMOND

Diamond material properties

Diamond is constituted by carbon atoms with a structure that is face-centered cubic and belongs to the Fd3m space group, as shown in Fig. 1. The C–C bond length in diamond is 1.545 Å and the lattice constant of the diamond structure is 3.567 Å. Diamond has an indirect bandgap of 5.47 eV, a binding energy of 0.07 eV for the indirect exciton and an effective mass of electrons of 0.2 m_0 (where m_0 is the free electron mass) [7, 8]. The main properties of diamond and other UWBG materials are shown in Table 1. Diamond has excellent properties for electronics, including a breakdown field of >10 MV cm^{-1}, a high carrier mobility of >5000 $cm^2\ V^{-1}\ s^{-1}$, a large electron saturation velocity of $>2\times10^7$ cm s^{-1} and a high thermal conductivity of >2000 W m^{-1} K^{-1}. These properties render diamond an exceptional material for high-voltage [9], high-temperature [10] and high-frequency [11] applications. Its large bandgap, high carrier mobility, low atomic number and radiation hardness are also highly attractive for radiation detection [12, 13].

Diamond is composed of 98.9% ^{12}C with a hardness of 10 Mohs [17]. The calculated tensile strengths of diamonds are 225, 130 and 90 GPa for the [100], [110] and [111] directions, respectively [18]. The compressive strengths of diamond by calculation are 223.1, 469.0 and 470.4 GPa in the [100], [110] and [111] directions, respectively [19]. The calculated Young's moduli of diamond by chemical vapor deposition (CVD) are 1164, 1151 and 1106 GPa in the (111), (110) and (100) planes, respectively [20]. The elastic constants of diamond are 9.5–10.8, 1.3–3.9 and 4.3–5.8 cyn cm^{-2} for constants c_{11}, c_{12} and c_{44}, respectively [21–23]. The thermal conductivity of diamond at 300 K is around 20 W cm^{-1} K^{-1} and increases with decreasing temperature at >100 K, as shown in Fig. 2a. The thermal conductivity of diamond with 99.999% ^{12}C can be higher than 2000 W cm^{-1} K^{-1} at

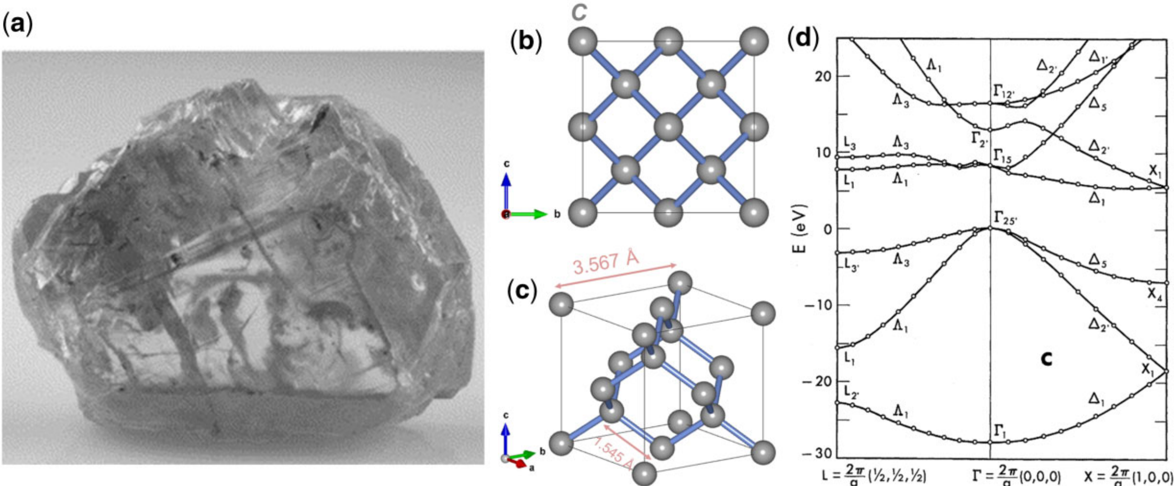

Figure 1: (a) Photograph of natural diamonds [14]. Reprinted from Ref. [14] with permission. Copyright 2003, Elsevier. Diamond crystal structure: (b) arrangement of atoms from [100] direction; (c) face-centered cubic structure. (d) Calculated electronic band structure of diamond [8]. Reprinted from Ref. [8] with permission. Copyright 1966, American Physical Society.

Table 1: Properties of diamond and other UWBG materials at room temperature [15, 16]

Parameters	AlN	β-Ga_2O_3	h-BN (2D)	Diamond
Bandgap (eV)	6	4.9	6.1	5.5
Breakdown field E_C (MV cm^{-1})	15.4	10.3	7	13
Electron drift mobility ($cm^2\ V^{-1}\ s^{-1}$)	426	180	48 ± 24 (Si doping)	7300
Hole drift mobility ($cm^2\ V^{-1}\ s^{-1}$)	/	/	/	5300
Saturated electron velocity υ_{sat} (10^7 cm/s)	1.3	1.1	/	2.3
Relative permittivity	9.76	10	4.97	5.7
Thermal conductivity (W m^{-1} K^{-1})	319	27	550 ± 75	2290

Downloaded from https://academic.oup.com/ooms/article/2/1/itac004/6581087 by guest on 04 August 2022

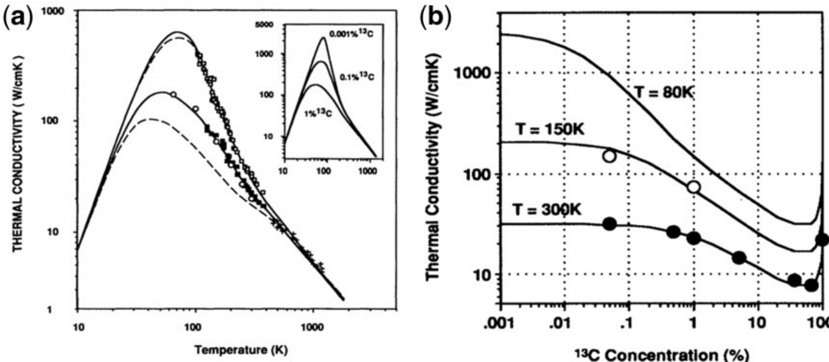

Figure 2: (a) Thermal conductivity of diamond with different ^{13}C concentrations [24]. The inset shows the calculated curves by the Callaway theory. Reprinted from Ref. [24] with permission. Copyright 1993, American Physical Society. (b) Thermal conductivity of diamond as a function of the percentage of ^{13}C at different temperatures [24]. Reprinted from Ref. [24] with permission. Copyright 1993, American Physical Society.

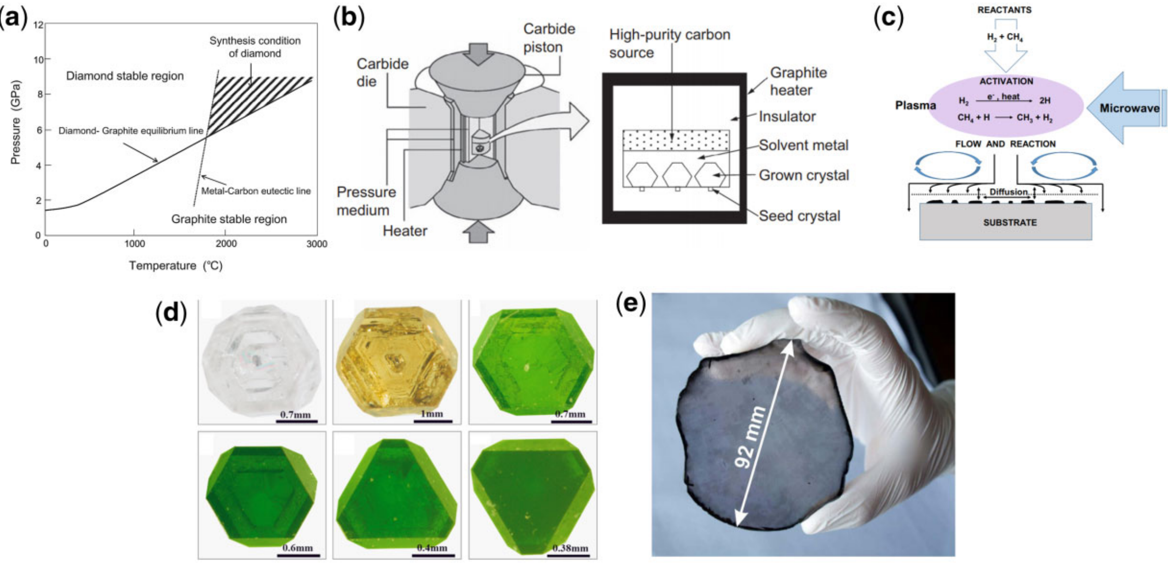

Figure 3: (a) Phase diagram of diamond growth [27]. Reprinted with permission from Ref. [27]. Copyright 2016, Elsevier. (b) HPHT method (temperature-gradient) [27]. Reprinted with permission from Ref. [27]. Copyright 2016, Elsevier Ltd. (c) Schematic of using the microwave plasma CVD to synthesize the diamond [27]. Reprinted with permission from Ref. [27]. Copyright 2016, Elsevier Ltd. (d) The image of the HPHT diamond single crystal [29]. Reprinted from Ref. [29] with permission. Copyright 2016, Elsevier. (e) As-grown diamond single crystal synthesized by CVD [34].

~80 K if not limited by point defect scattering [24]. Figure 2b indicates that the thermal conductivity of diamond at room temperature increases with the purity of ^{12}C until it is beyond 99.9%. However, at lower temperatures (e.g. 80 K), the thermal conductivity of diamond can be further enhanced for improved purity of ^{12}C.

Diamond synthesis and characterization

There are two main synthesis approaches for growing diamond single crystals, including high pressure and high-temperature (HPHT) method [25, 26] and CVD method [27, 28]. The HPHT and CVD methods are conducted under conditions in the diamond phase and graphite phase [27], respectively (Fig. 3a). The HPHT method can be categorized into solubility-gradient, temperature-gradient, no-catalyst conversion and shock compression methods. The schematic of the apparatus for the temperature-gradient method is shown in Fig. 3b, where the typical conditions include pressure of >5.5 GPa and temperature of 1300–1400°C (Fig. 3a). The growth rate can be tuned by changing the temperature difference between the carbon source and the seed crystal. A solution of molten metal such as Fe, Co and Ni is situated between them, dissolving the carbon. Due to the temperature difference (20–50°C) and the concentration difference, the solution with carbon becomes supersaturated at the seed crystal, resulting in diamond growth on the seed crystal [27]. Dislocations in HPHT diamonds mainly come from the seed crystals [26]. Figure 3d shows the as-grown HPHT diamond single crystals [29]. The CVD method can be categorized into DC-, microwave- or RF-plasma CVD depending on the plasma source [27, 30, 31]. A mixture of methane (CH_4) and hydrogen (H_2) is the source of the CVD growth of diamonds (Fig. 3f). H radicals play multiple roles during the CVD growth, including terminating the dangling carbon bonds on the diamond surface, maintaining the sp^3 coordination of the surface carbon atoms, etching the graphite phase, producing CH_3 radicals and activating the surface bond [27, 32]. One typical defect in CVD diamond is hillocks [27, 33]. Figure 3e shows the as-grown diamond single crystal synthesized by CVD [34].

The growth and devices based on diamond homoepitaxial layers are still hindered by the size of HPHT diamond substrates

Downloaded from https://academic.oup.com/ooms/article/2/1/itac004/6581087 by guest on 04 August 2022

[27, 34]. Commercial single-crystal diamonds are available up to 10 mm and can go to around 30 mm by the mosaic process [28]. The commercial type-Ib HPHT diamonds exhibit dislocation densities of 10^3–10^6 cm^{-2} [35] while the type-IIa has been reported to show a lower density of around 10^3 cm^{-2} [36]. A homoepitaxial single-crystal diamond mosaic wafer as large as 40×60 mm has been reported, which was formed by combining the cloning and overgrowth of tiled substrates [37, 38]. Diamond heteroepitaxy on other substrate materials can be an alternative route to solving the problem, but it also face challenges such as lattice mismatch, thermal expansion coefficient mismatch and substrate stability under CVD growth conditions [28]. To grow diamond films on foreign substrates, accurate control of nucleation/seeding is an important step. Various nucleation and seeding methods have been demonstrated [39], including electrostatic seeding [40–42], bias enhanced nucleation [43–45], chemical nucleation [46–49], surface roughening [50–52], interlayer for nucleation enhancement [53–56] and mixed technique. A large-size single-crystal diamond of 92 mm in diameter that was synthesized on Ir/YSZ/Si(001) by heteroepitaxy has been reported, which showed a dislocation density of $\sim 4 \times 10^7$ cm^{-2} [34]. The growth of diamonds of over 2-inch was also investigated on Ir/sapphire [57]. In addition to single crystals, a polycrystalline diamond can also be grown by CVD. The properties of polycrystalline diamond are influenced by the grain structure and impurity content [58, 59].

In terms of doping, boron is usually used in diamond as the p-type dopant (activation energy: 0.37 eV), whereas phosphorus is used as the n-type dopant (activation energy: 0.59 eV) [27, 28]. Besides, heavily boron-doped diamond is an example of Mott's metal. In a boron-doped superconducting diamond, the electron spin resonance of conduction electrons has been observed [60]. Surface transfer doping is another approach for doping by forming a quasi-2D hole channel a few nanometers below the surface [28, 61, 62]. Raman spectroscopy is used as a non-destructive tool to characterize carbon materials and estimate the sp^2-to-sp^3 bonding ratio [63–66]. Typical Raman spectra of carbon materials including diamond, graphite and microcrystalline graphite are shown in Fig. 4a–c for comparison [67]. Figure 4d–f shows the first-order Raman spectra of diamond thin films. The first-order Raman modes are triply degenerate TO(X) phonons of F2g symmetry [64]. Figure 4e and g shows the single-crystal diamond-dominated spectra with the first-order Raman line at 1332 cm^{-1} [64, 67]. The second-order and third-order peaks are also shown in Fig. 4g. The first-order peak for cubic diamond would show a redshift if ^{13}C is substituted for ^{12}C [64]. The first-order peak for hexagonal diamonds is 1325 cm^{-1} [64, 68].

Diamond devices and applications

Electronics

Diamond, like other WBG and UWBG materials, was once considered an insulator. However, the key property to define the semiconductor is not the value of the bandgap but is that the carriers (holes and electrons), thereby the resistivity, in the material or part of the material can be tuned, by approaches such as doping, polarization or surface transfer doping. Diamond shows great potential for next-generation power electronic devices due to its UWBG, ultrahigh critical electrical field and largest thermal conductivity among the UWBG semiconductor family. Figure 5a–e shows recent reported diodes based on diamond including unipolar and pseudo-vertical Schottky barrier diode (pVSBD) [69, 70], vertical SBD [71–73], Schottky pn diodes (SPNDs) [74], metal-intrinsic-p-type diodes (MiPDs) [75, 76] and bipolar diodes including p-type-intrinsic-n-type diodes (PiNDs) [77]. The highest breakdown voltage of >10 kV was obtained for a diamond PiND, while the highest breakdown field of >7 MV cm^{-1} was reported on a diamond pVSB diode [69, 70, 78]. Figure 5f–j shows the reported transistors based on diamond including metal–semiconductor field-effect transistors (MESFETs) [79], junction gate FETs (JFETs) [80, 81], hydrogen-terminated FETs (H-FET) [82–84], metal–oxide–semiconductor FETs (MOSFETs) [85] and bipolar junction transistor (BJT) [86]. The highest breakdown voltage of 2 kV was obtained on diamond MESFET and H-FET, while the highest breakdown field of >6 MV cm^{-1} was reported on a diamond JFET [78]. Edge-termination is always the key to designing high-voltage power devices and different kinds of defects in diamonds also need to be taken into consideration [78].

NV center

The NV center in diamond is a point defect with C_{3v} symmetry and consists of a substitutional NV pair orientated along the [111] direction [87, 88]. The NV center in diamond is very important in emerging quantum technologies [28, 88–90], including quantum metrology, quantum information processing, quantum communication and tests of entanglement in quantum mechanics, as well as nanoscale magnetometry [91–93], bio-

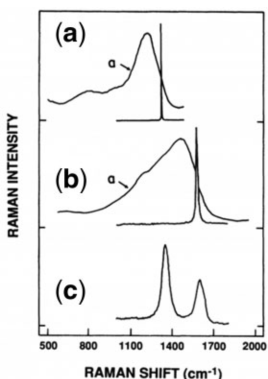

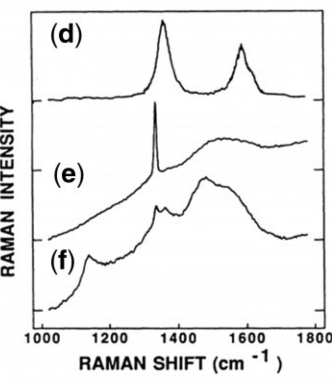

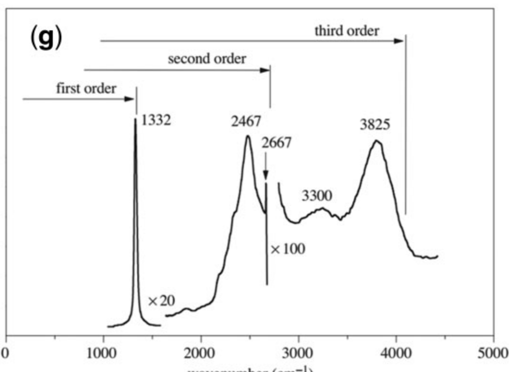

Figure 4: Raman spectra of carbon materials including (a) diamond, (b) graphite and (c) microcrystalline graphite [67]. The lines in (a) and (b) labeled *a* are the spectra of *a*-Si scaled to the diamond frequency. Reprinted with permission from Ref. [67]. Copyright 1990, American Physical Society. (d) A diamond-like film that is similar to microcrystalline graphite [67]. Reprinted with permission from Ref. [67]. Copyright 1990, American Physical Society. (e) and (f) The sharp feature at 1322 cm^{-1} indicates crystalline diamond, while features between 1350 and 1600 cm^{-1} are due to sp^2-bonded carbon [67]. Reprinted with permission from Ref. [67]. Copyright 1990, American Physical Society. (g) Raman spectrum of the gem-quality diamond at room temperature [64]. Reprinted with permission from Ref. [64]. Copy right 2004, The Royal Society (UK).

Downloaded from https://academic.oup.com/ooms/article/2/1/itac004/6581087 by guest on 04 August 2022

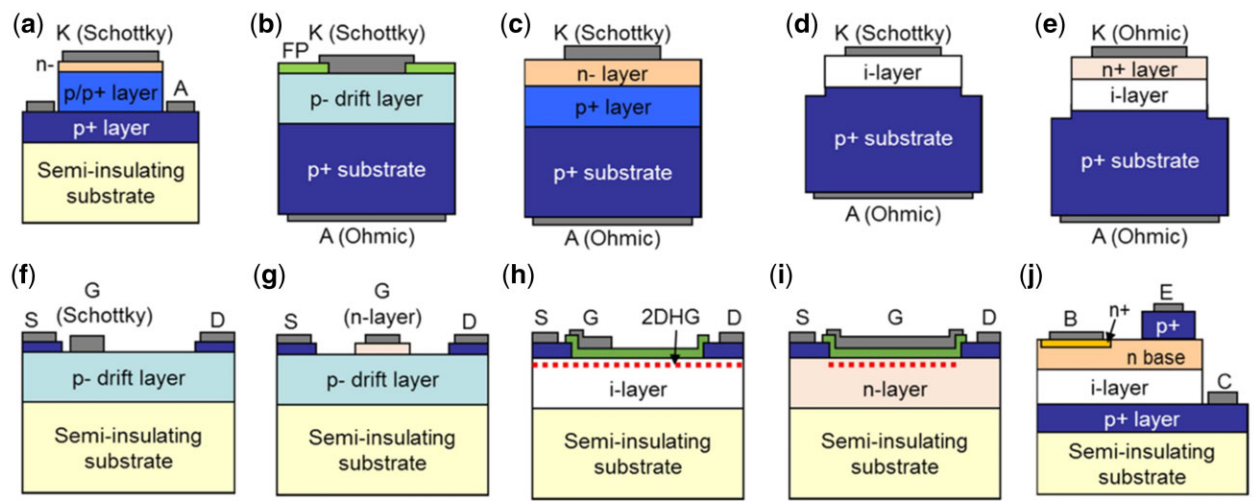

Figure 5: Schematics of diamond diodes and transistors [78]. (a) pVSD. (b) VSBD. (c) SPND. (d) MiPD. (e) PiN. (f) MESFET. (g) JFET. (h) H-FET. (i) MOSFET. (j) BJT. Reprinted with permission from Ref. [78]. Copyright 2018, Elsevier.

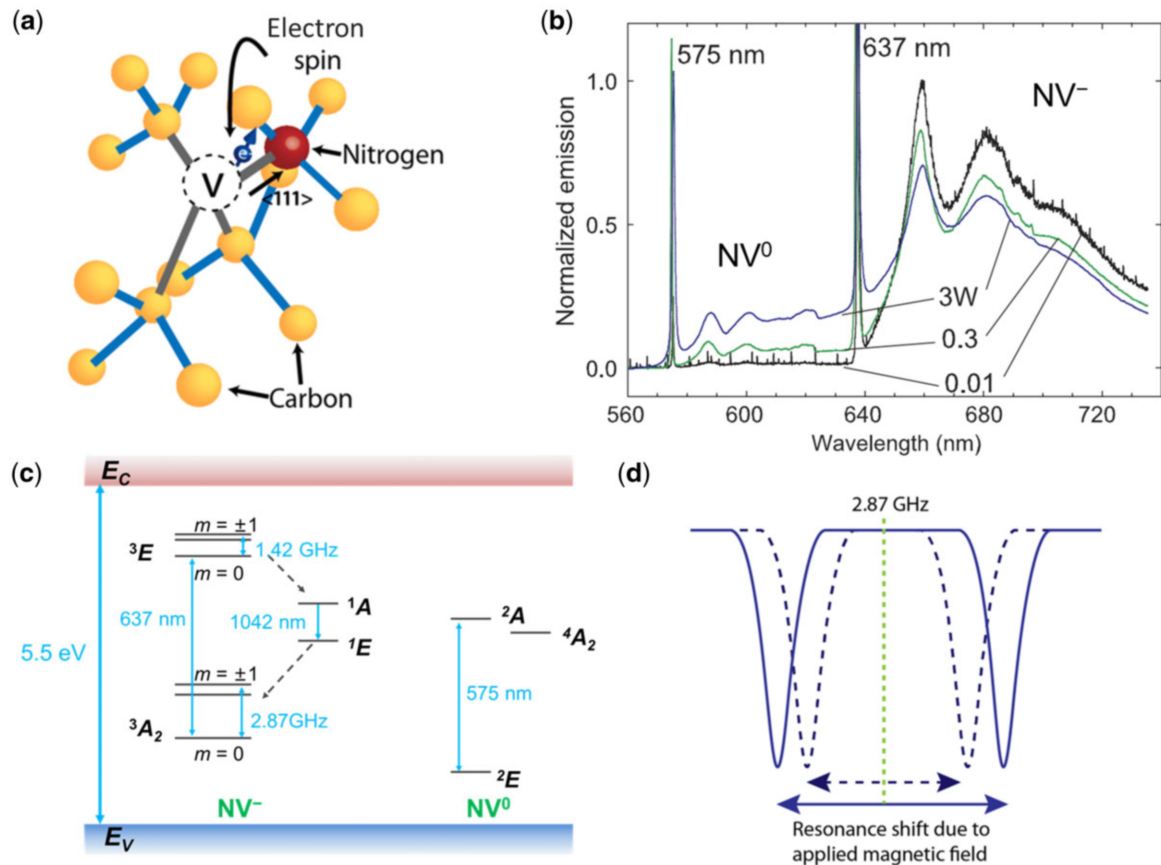

Figure 6: (a) NV center in diamond [90]. Reprinted with permission from Ref. [90]. Copyright 2021, Springer Nature. (b) Normalized emission spectra of NV^- and NV^0 centers at 10 K [88]. Reprinted with permission from Ref. [88]. Copyright 2013, Elsevier. (c) Energy level diagram of the NV^- center and NV^0 center [88, 100, 101]. (d) Zeeman shift due to applied magnetic field [90]. Reprinted with permission from Ref. [90]. Copyright 2021, Springer Nature.

magnetometry [94], electrometry [95] and decoherence microscopy [96, 97]. The diamond crystal structure with a NV center is shown in Fig. 6a. The center exists in the negative (NV^-) [98] and neutral (NV^0) [99] charge states with optical zero phonon lines (ZPLs) at 637 and 575 nm, respectively [88], as shown in Fig. 6b. The zero-field splitting (ZFS) of the NV^- center is 2.87 GHz which occurs between the $m_S = 0$ and $m_S = \pm 1$ spin sublevels of the spin-triplet ground state $^3A_2$ while it is 1.42 GHz for the spin-triplet excited state ^3E [88, 91, 100, 101]. Figure 6c shows the energy level diagrams for the NV^- and NV^0 centers. It is the

Downloaded from https://academic.oup.com/ooms/article/2/1/itac004/6581087 by guest on 04 August 2022

basis of all applications that are based on the diamond NV center. The applied magnetic field can cause a Zeeman shift (Fig. 6d) [90]. Electron-nuclear double resonance (ENDOR) study has also been reported based on the high NV^- concentrations that can be used for sensing the vector of magnetic fields [102].

Quantum computation and network

Building an optimal quantum computer needs to isolate a system from the environment while ensuring the greatest possible control over it [103]. According to quantum mechanical laws, both requirements are impossible to fulfill at the same time; therefore, a compromise solution is needed. Vacuum ($<10^{-12}$ mbar) is an optimal condition to shield the disturbance and the qubits can be controlled utilizing electromagnetic waves [103]. Another solid-state solution is diamond since its large bandgap ensures an unoccupied conduction band (CB) even at room temperature. So, no free electrons can unintentionally interact with the qubits. The NV center qubit has very good coherence times even at room temperature [104–107]. The corresponding fidelity is comparable to or even higher than that of a superconducting qubit system [103]. A brief schematic of a quantum network node that utilizes color centers in diamond is shown in Fig. 7a [108]. The node consists of an optically active (communication) qubit. Using the microwave, the state of the color center qubit can be swapped by the high-fidelity gates onto the nuclear spin (memory) qubits that are long-lived. The network nodes can be tuned to an optimal frequency operation point by the electric field. Photons that are entangled with the state of the communication qubit can be down-converted to telecommunication wavelengths. Recent experiments have shown the great potential of color centers in diamonds that can be used as quantum network node candidates. Figure 7b shows the layout of a three-node quantum network employing NV centers in diamond. A state-of-the-art study reported a 10-qubit solid-state spin register realized by using the decoherence-protected gates, containing 9 nuclear spins in diamond and the electron spin of an NV center [109] (Fig. 7c). The measured Bell state fidelities for all pairs of qubits in the 10-qubit register are shown in Fig. 7d.

PART II β-Ga_2O_3

β-Ga_2O_3 materials and synthesis

Ga_2O_3 has six phases, including α, β, γ, δ, ε and κ phases [117–120] with hexagonal, monoclinic, cubic, cubic, hexagonal and orthorhombic crystal structures, respectively [112].. As shown in Fig. 8a, these phases can be transformed into the most stable beta phase by different thermal processes [111–113], which offer an avenue to grow β-Ga_2O_3 by post-thermal annealing process [121]. β-Ga_2O_3 has a monoclinic crystal structure and has lattice constants of $a = 12.2$ Å, $b = 3.04$ Å, and $c = 5.80$ Å, and the angle between a- and c-axes is 104° (Fig. 8b) [114, 115]. β-Ga_2O_3 has a highly asymmetric monoclinic crystal structure, which results in anisotropic material properties. Different thermal, optical and electrical properties along different crystal orientations have been observed [122, 123]. Guo *et al.* [124] found that [010] direction has a thermal conductivity three times larger than [100] direction. Fu *et al.* [125] also observed anisotropic electrical properties in β-Ga_2O_3 SBDs, including Schottky barrier heights, turn-on voltages, on-resistance and electron mobilities. Li *et al.* [126] also showed that the sidewall orientation of β-Ga_2O_3 trench SBDs directly impacted the forward device characteristics due to different interface charge densities. Zhang *et al.* [127, 128] observed anisotropic wet etching of β-Ga_2O_3 with hot phosphoric acid, which is highly related to the atomic density, chemical reactivity and bonding of different planes. Mu *et al.* [129, 130] and Bhuiyan *et al.* [131] theoretically and experimentally demonstrated the orientation-dependent band offsets in β-$(Al_xGa_{1-x})_2O_3$ and β-Ga_2O_3 heterostructures. Furthermore, Montes *et al.* [132] reported different deep-level defects induced after irradiation on different crystal orientations, i.e. anisotropic radiation effects in β-Ga_2O_3. Chen *et al.* [133] also showed different nonlinear optical properties for (010) and (−201) β-Ga_2O_3, including Kerr nonlinear refractive index, two-photon absorption (TPA) coefficient and polarization dependence. Furthermore, due to the large lattice constants, β-Ga_2O_3 has two cleavage planes, i.e. (100) and (001) planes, which allow for mechanical exfoliation of β-Ga_2O_3 into thin-belts or nano-membranes [119, 120] for novel device applications. β-Ga_2O_3 has an UWBG of ~4.8 eV (Fig. 8c) and a high

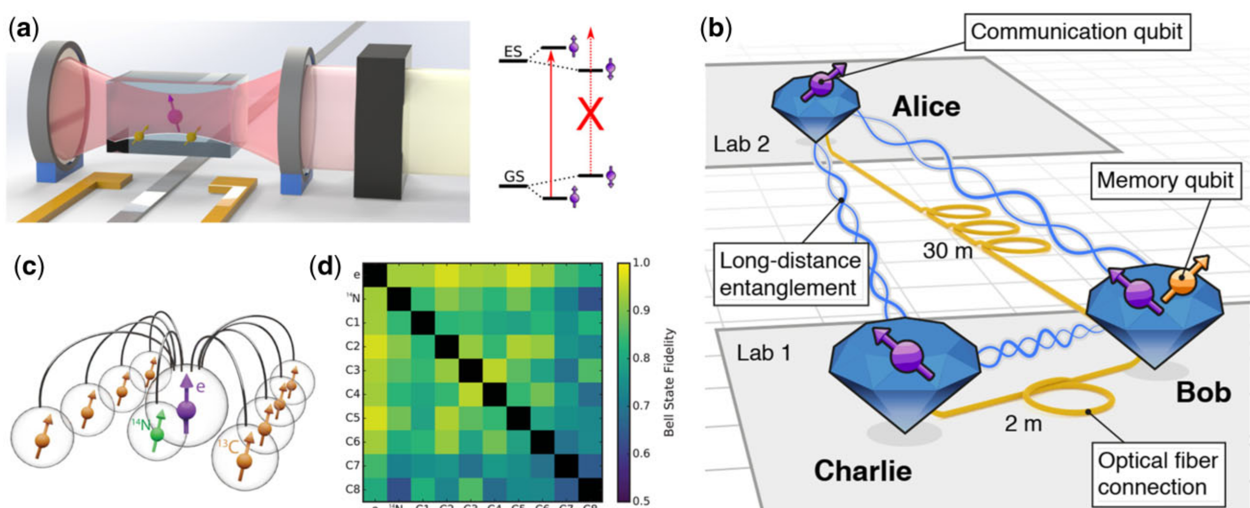

Figure 7: (a) Schematic of a quantum network node utilizing the qubit (purple) based on the color center in diamond [108]. Dedicated lines (gray) can generate microwave to change to qubit state while the electrodes (yellow) can produce a static electric field to tune the network nodes. Reprinted with permission from Ref. [108]. Copyright 2021, AIP publishing. (b) Layout of a three-node quantum network employing NV centers in diamond [110]. Reprinted with permission from Ref. [110]. Copyright 2021, The American Association for the Advancement of Science. (c) Schematic of a 10-qubit quantum register [109], including a central qubit, an intrinsic ^{14}N nuclear spin and 8 ^{13}C nuclear spins. (d) Measured Bell state fidelities showing entanglement generation in the 10-qubit register shown in (c).

Downloaded from https://academic.oup.com/ooms/article/2/1/itac004/6581087 by guest on 04 August 2022

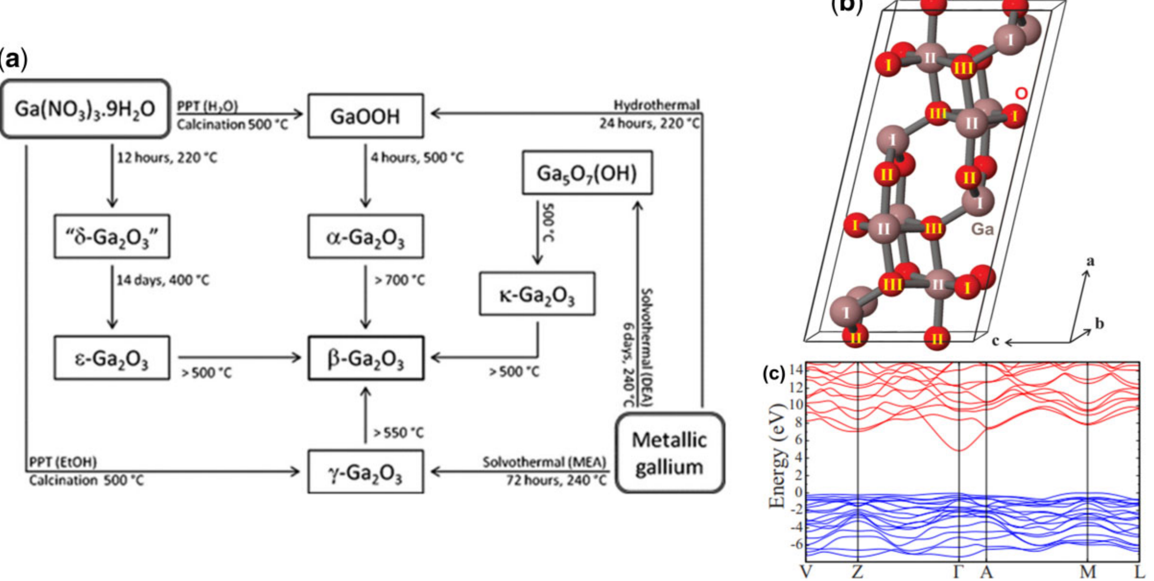

Figure 8: (a) Transformation relationships between different phases of Ga_2O_3 [111–113]. Reprinted with permission from Ref. [111]. Copyright 2018, AIP Publishing. (b) Crystal structure of monoclinic β-Ga_2O_3 [114, 115]. Reprinted with permission from Ref. [114]. Copyright 2020, AIP Publishing. (c) Simplified band structure of β-Ga_2O_3 [114, 116]. Reprinted with permission from Ref. [116]. Copyright 2010, AIP Publishing.

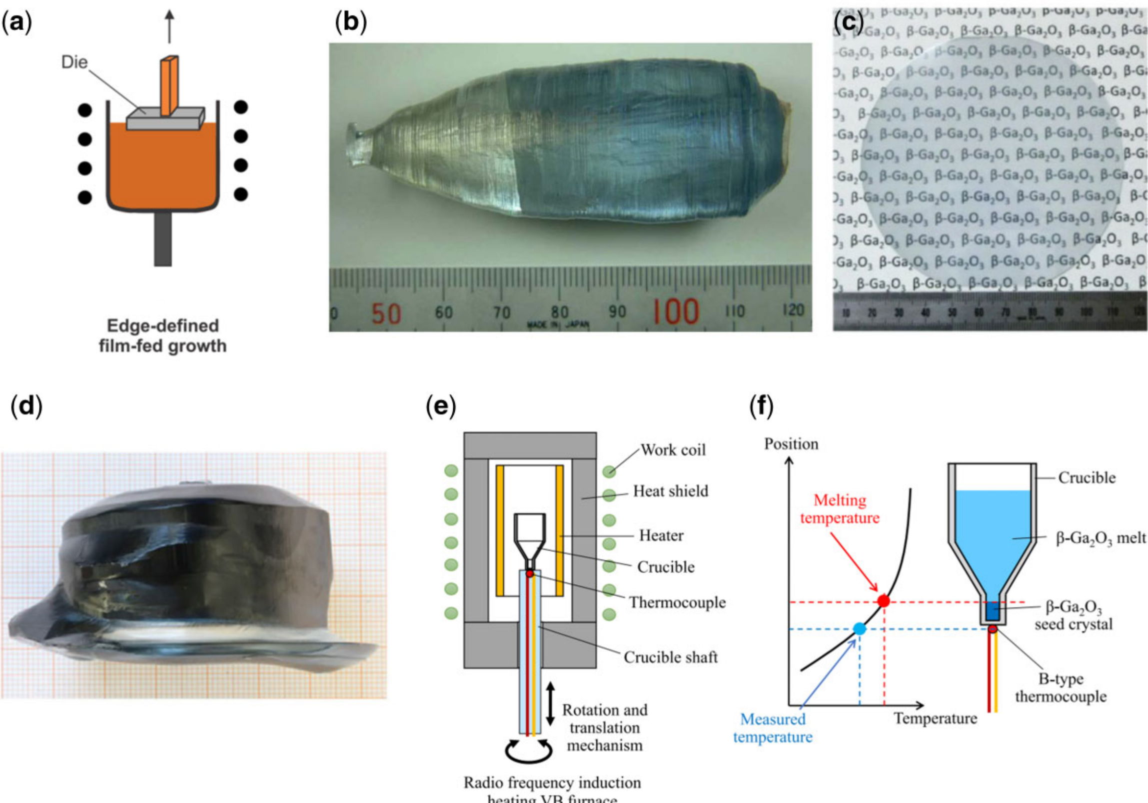

Figure 9: (a) Schematic of EFG method for growing β-Ga_2O_3 bulk crystal [135]. Reprinted with permission from Ref. [135]. Copyright 2020, AIP Publishing. (b) Images of EFG-grown β-Ga_2O_3 bulk crystal. The sample was cut perpendicular to the [010] direction and shaped into a flat hexagonal prism [138]. Reprinted with permission from Ref. [138]. Copyright 2004, Elsevier. (c) Photograph of 4-inch β-Ga_2O_3 substrates [136]. Reprinted with permission from Ref. [136]. Copyright 2020, AIP Publishing. (d) Photograph of high conductive 2-inch β-Ga_2O_3 bulk [139]. Reprinted with permission from Ref. [139]. Copyright 2022, AIP Publishing. (e) Schematic of vertical Bridgman method with inductive heating [137]. Reprinted with permission from Ref. [137]. Copyright 2016, Elsevier. (f) Temperature distribution versus position in the vertical Bridgman furnace [137]. Reprinted with permission from Ref. [137]. Copyright 2016, Elsevier.

Downloaded from https://academic.oup.com/ooms/article/2/1/itac004/6581087 by guest on 04 August 2022

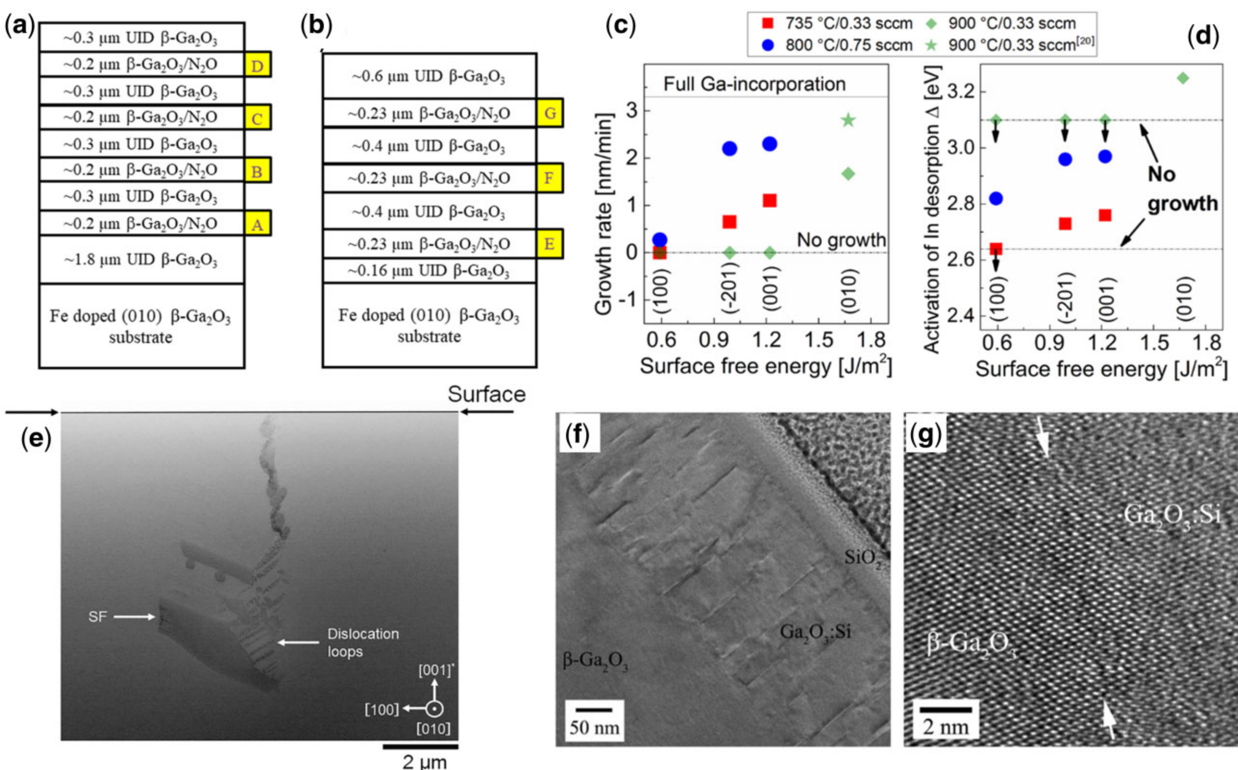

Figure 10: (a) and (b) Images of various MOCVD grown β-Ga_2O_3 stack structures using N_2O separated by oxygen grown UID β-Ga_2O_3 films for SIMS analysis [147]. From Ref. [147], licensed under a Creative Commons Attribution (CC BY) license. (c) Growth rates for (100), (−201), (001) and (010) homoepitaxy by In-mediated (MEXCAT-MBE) under three different synthesis conditions [155]. From Ref. [155], licensed under a Creative Commons Attribution (CC BY) license. (d) Activation energy of In desorption evaluated from the catalytic growth model, as a function of the theoretically predicted surface energy of the respective orientations [155]. From Ref. [155], licensed under a Creative Commons Attribution (CC BY) license. (e) Cross-sectional STEM image of a bright spot for HVPE grown β-Ga_2O_3 sample [161]. Reprinted with permission from Ref. [161]. Copyright 2021, AIP Publishing. (f) and (g) Cross-sectional TEM images of Ga_2O_3:Si film deposited on (010) β-Ga_2O_3 substrate [166]. The interface is indicated by arrows. Reprinted with permission from Ref. [166]. Copyright 2017, AIP Publishing.

critical electric field of ~8 MV [114, 116], which are promising for deep UV and power electronic applications.

Bulk β-Ga_2O_3 crystals can be grown by edge-defined film-fed growth (EFG), Czochralski (CZ) [134], float zone (FZ), vertical gradient freeze and vertical Bridgman methods [135–138]. Matthew [135] has extensively summarized the growth techniques of bulk β-Ga_2O_3 and the schematic of EFG is shown in Fig. 9a. The β-Ga_2O_3 melt goes up to the top of the chamber through the slit by capillary action. 1-inch [138] (Fig. 9b) and 4-inch β-Ga_2O_3 wafers have been commercialized [136] (Fig. 9c) and high conductive β-Ga_2O_3 bulk have been demonstrated [139]. Oishi *et al.* [140] reported one of the highest electron mobility of 153 $cm^2 V^{-1} s^{-1}$ at 300 K in β-Ga_2O_3 grown by the EFG method. For the carrier scattering, the ionized impurity scattering is dominant at low temperatures and the optical phonon scattering is dominant at high temperatures. There are three main defects in EFG-grown β-Ga_2O_3 [141–144], including dislocations (e.g. edge and screw dislocations), voids (e.g. nanopipes and grooves) and twins [136, 145], as shown in Fig. 9d. In addition, the defects in bulk β-Ga_2O_3 can be partly recovered via electron beam irradiation [141–144, 146]. Hoshikawa *et al.* [137] grew twin-free β-Ga_2O_3 crystals with (100), (010) and (001) orientations using the vertical Bridgman method with inductive heating (Fig. 9e and f). They also demonstrated the 2-inch β-Ga_2O_3 bulk crystal growth via resistive heating vertical Bridgman furnace in ambient air, enabling the growth of large β-Ga_2O_3 crystals with small weight loss of the crucible [137].

Several methods have been developed to epitaxially grow β-Ga_2O_3 films, including MOCVD, MBE, hydride vapor phase epitaxy (HVPE) and PLD. MOCVD has advantages for mass production and it is suitable to grow high-quality β-Ga_2O_3 films with an unintentional doping concentration from 1×10^{14} cm^{-3} to 3×10^{16} cm^{-3} [147, 148]. Alema *et al.* [148] reported that introducing a small amount of H_2O vapor into O_2 during MOCVD growth further reduced the background carrier concentration due to the generation of H_2 and compensation of defects. And they also demonstrated low free-carrier concentration in MOCVD-grown β-Ga_2O_3 by using N_2O for oxidation (Fig. 10a and b) [147]. To date, high room-temperature electron mobilities in the range of 150–200 $cm^2 V^{-1} s^{-1}$ and low-temperature electron mobilities of 12,400 $cm^2 V^{-1} s^{-1}$ at 46K and 23,400 $cm^2 V^{-1} s^{-1}$ at 23 K have been achieved [149–151] for MOCVD-grown β-Ga_2O_3 [152, 153]. Alema *et al.* [154] also reported a fast growth rate of ~10 μm/hr of β-Ga_2O_3 thin films using a close-coupled showerhead MOCVD reactor and separate injection of O_2 and MO precursors. The MBE is also widely used for growing ultra-high quality epilayers with sharp interfaces but usually has low growth rates. Mazzolini *et al.* [155] investigated the growth rate of β-Ga_2O_3 under different crystal orientations in the indium-mediated metal-exchange catalyzed molecular beam epitaxy (MEXCAT-MBE) method, which is an emerging technology for increasing the growth rate [156]. As shown in Fig. 10c and d, the growth rates increased with the surface free energy of different orientations, i.e. (100) $<$ (−201) $<$ (001) $<$ (010) [155]. In addition, increasing growth temperature can also increase the growth rate [155, 156]. HVPE has the advantages of high growth rates, low cost and decent film quality. Therefore, it is commonly used for producing thick epilayers for high voltage

Downloaded from https://academic.oup.com/ooms/article/2/1/itac004/6581087 by guest on 04 August 2022

vertical β-Ga_2O_3 devices [157–159]. Higashiwaki *et al.* [160] reported HVPE-grown (001) β-Ga_2O_3 Schottky barrier diodes (SBDs) with low on-state resistance (R_{ON}) of 2.4 mΩ·cm^2 and a high breakdown voltage of >500 V. But the breakdown voltage was still far below the theoretical limit mainly due to killer defects (Fig. 10e) generated during the fast growth of the film [161, 162]. PLD method is a common deposition technique for oxide materials and has the capability of control over material stoichiometry and film thickness, surface morphology and quality [163]. Shen *et al.* [164] comprehensively investigated β-Ga_2O_3 film properties with different laser energy and the number of laser shots by the PLD technique. Khartsev *et al.* [165] also demonstrated Si-doped β-Ga_2O_3 films with a high free carrier concentration of 2.5×10^{19} cm^{-3} using SiO_2-containing Ga_2O_3 target via PLD process (Fig. 10f and g). PLD growth of β-Ga_2O_3 films also has the advantages of low-temperature growth, which can be useful for low thermal budget devices and the regrowth process for the ohmic contacts in β-Ga_2O_3 devices.

Current status of β-Ga_2O_3 doping

n-Type doping in β-Ga_2O_3 can be obtained using various donors such as Si, Sn, Zr, Hf and Nb [167–170] with ionization energy in the range of 7–30 meV. Among them, Si and Sn are the most widely used shallow donors with free-electron concentrations up to $\sim 1 \times 10^{19}$ cm^{-3} and low resistivity down to 5 mΩ cm. With increasing n-type doping concentration from 1×10^{17} to 1×10^{19} cm^{-3}, the electron mobility in the β-Ga_2O_3 decreased from 130 to 25 cm^2 V^{-1} s^{-1} at room temperature due to electron scattering by polar optical phonons. For bulk β-Ga_2O_3, the doping concentration of Si and Sn was usually limited up to 2×10^{19} cm^{-3} due to crystal quality degradation and the high evaporation rate of Sn [138, 171]. For epitaxially grown β-Ga_2O_3 using MOCVD and MBE, a high concentration of n-type doping of over 10^{20} cm^{-3} can be achieved. In addition, precise control doping such as 3 nm delta-doping width has also been demonstrated in MOCVD [172]. For p-type doping, it is very challenging for β-Ga_2O_3 due to large ionization energy, large hole effective mass caused by flat valance band and self-trapping of holes [173]. Nevertheless, several candidates have been explored for β-Ga_2O_3. It was found that Mg, Fe, Zn, Co and Ti are deep acceptors in β-Ga_2O_3 that can effectively increase the resistivity of β-Ga_2O_3 films [159, 173–178]. Feng *et al.* [177] investigated the electrical insulating property of the Mg-doped MOCVD-grown β-Ga_2O_3 films varying Mg MO flow rate and growth temperature (Fig. 11a and b). In addition, the Mg-doped buffer layer grown at the substrate–epilayer interface could effectively compensate for the charge accumulation at the interface, which is critical for lateral devices. It should be noted that a high Mg MO flow rate could also result in surface morphology deterioration due to strong surface segregation, as shown in Fig. 11c and d. Although Mg doping was realized in β-Ga_2O_3, p-type doing was not observed due to the low mobility of self-trapped holes. Recent work demonstrated the possibility for p-type doping via hydrogen incorporation in β-Ga_2O_3 [179]. In addition to Mg at Ga sites (Fig. 11e), N at O sites can also induce deep acceptor levels (Fig. 11f), where the former binds the hole to a next-nearest O neighbor and the latter binds the hole unto itself [180]. The transition levels of other impurities such as Be, Ga, Sr, Zn and Cd are also calculated using hybrid density function calculations and shown in Fig. 11g [180].

β-Ga_2O_3 electronic and photonic devices

UWBG semiconductor β-Ga_2O_3 has garnered significant research interest for power conversion, RF and deep UV applications. Due to its large bandgap, high critical breakdown field and large Baliga's figure of merit (BFOM), β-Ga_2O_3 is a promising candidate for high-voltage power electronics. Various β-Ga_2O_3-based power devices have been demonstrated, including SBDs

Downloaded from https://academic.oup.com/ooms/article/2/1/itac004/6581087 by guest on 04 August 2022

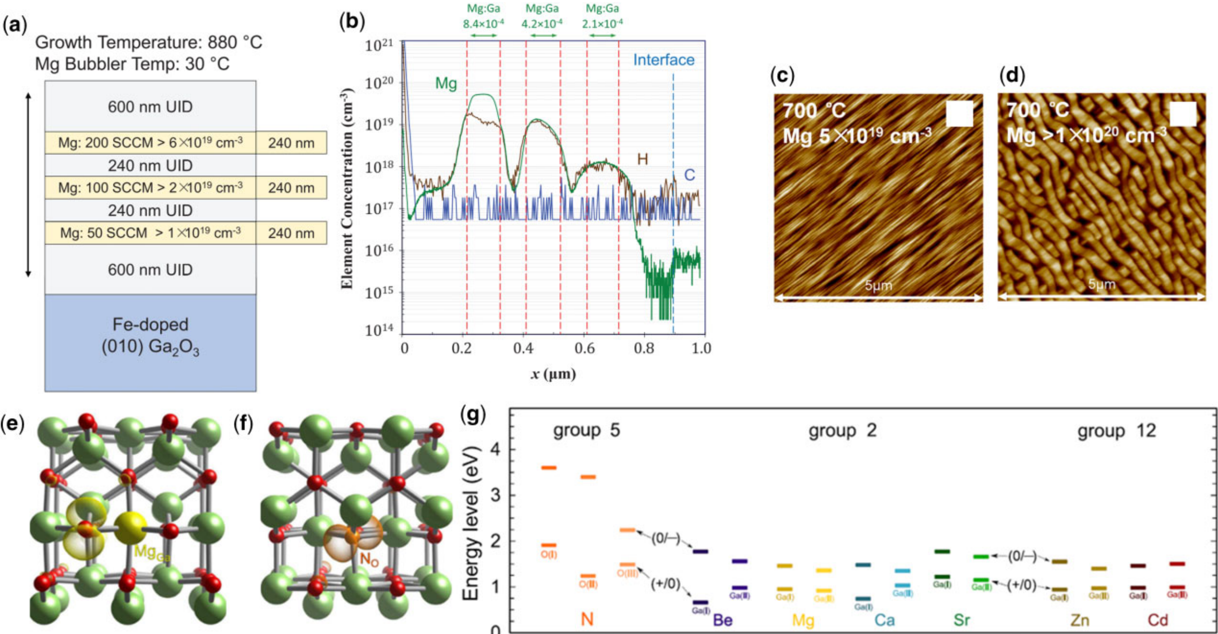

Figure 11: (a) Schematic of the sample layer stack and (b) SIMS profile of Mg-doped β-Ga_2O_3 by MOCVD [177]. Reprinted with permission from Ref. [177]. Copyright 2020, AIP Publishing. (c) and (d) Surface AFM images of Mg-doped β-Ga_2O_3 with different Mg doping concentrations [177]. Reprinted with permission from Ref. [177]. Copyright 2020, AIP Publishing. (e) and (f) Mg on the Ga(II) site and N on the O(III) coordinated O site [180]. Reprinted with permission from Ref. [180]. Copyright 2018, IOP Science. (g) Transition levels for the nitrogen group 12, group 5 and group 2 elements in β-Ga_2O_3 [180]. Reprinted with permission from Ref. [180]. Copyright 2018, IOP Science.

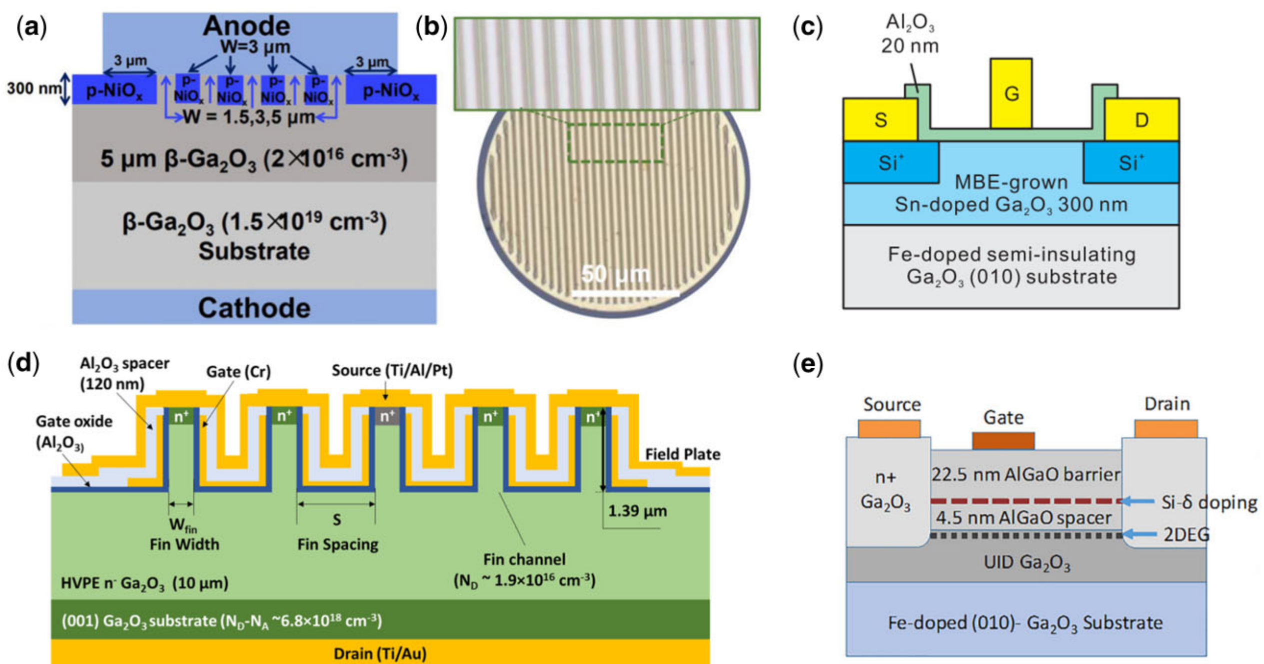

Figure 12: (a) Schematic and (b) microscopy image of lateral β-Ga_2O_3 SBD with field plate structure [120]. Reprinted with permission from Ref. [120]. Copyright 2021, AIP Publishing. (c) depletion-mode β-Ga_2O_3 MOSFET [188]. Reprinted with permission from Ref. [188]. Copyright 2012, AIP Publishing. (d) β-Ga_2O_3 vertical FinFET [191]. Reprinted with permission from Ref. [191]. Copyright 2021, AIP Publishing. (e) Delta-doped β-$(Al_xGa_{1-x})_2O_3$/β-Ga_2O_3 HEMTs [189]. Reprinted with permission from Ref. [189]. Copyright 2018, AIP Publishing.

[120, 181–184], MOSFETs [185–187], high electron mobility transistors (HEMTs) [188, 189], current-aperture vertical electron transistors (CAVETs) [157, 158, 190] and Fin-FET [158, 186, 191]. Due to low turn-on voltage, fast switching speed, and high efficiency, β-Ga_2O_3 SBDs are important components of power electronics such as high-power inverters and converters for power supplies and power factor corrections. Yan *et al.* [120] showed field-plated lateral β-Ga_2O_3 SBDs (Fig. 12a and b) with a breakdown voltage of >3 kV and DC power FOM of 370 MW cm^{-2}, which is compared with previous reports [192–198]. Higashiwaki *et al.* [187] first demonstrated the D-mode β-Ga_2O_3 MOSFET (Fig. 12c) and the β-Ga_2O_3 vertical transistor called CAVET [157]. However, the β-Ga_2O_3 CAVET had a relatively low breakdown voltage of <300 V, possibly due to the deficiency of current blocking capability in nitrogen implanted regions. Chatterjee *et al.* [191] fabricated E-mode vertical β-Ga_2O_3 Fin-FETs (Fig. 12d) with a breakdown voltage of 2.66 kV, a specific on-resistance of 25.2 mΩ·cm^2 and a BFOM of 280 MW cm^{-2}. Zhang *et al.* [189] demonstrated delta-doped β-$(Al_xGa_{1-x})_2O_3$/β-Ga_2O_3 HEMTs (Fig. 12e) to improve the relatively low bulk mobility of β-Ga_2O_3 by forming two-dimensional electron gas (2DEG) [151, 199–202]. The confined sheet carrier density at the 2DEG channel was as high as 3×10^{12} cm^{-2} [203] with a record room-temperature electron mobility of 184 cm^2 V^{-1} s^{-1} [151]. The design space of delta-doped β-$(Al_xGa_{1-x})_2O_3$/β-Ga_2O_3 HEMT has been comprehensively investigated by Wang *et al.* [204]. Furthermore, the low thermal conductivity of β-Ga_2O_3 is also a limiting factor for high power devices. Thermal management approaches such as superlattice structures, high thermal conductivity substrates and double-side packaging have been developed [205, 206] to improve thermal dissipation. In addition to power electronics, β-Ga_2O_3 has also been investigated for RF electronics [199, 207, 208] and the recent progress is summarized in Moser's work [207]. An extrinsic cutoff frequency of 27 GHz was achieved for the small-signal operation of the transistors [209] and Green *et al.* [200] demonstrated the β-Ga_2O_3 MOSFET with an extrinsic cutoff frequency of 3.3 GHz and output power of 0.23 W mm^{-1}.

Due to the lack of p-type β-Ga_2O_3, most of the β-Ga_2O_3 electronic devices are unipolar devices. In order to avoid this issue, other p-type materials were used as a heterojunction with β-Ga_2O_3, such as p-Si, NiO, Cu_2O and GaN [210–213]. Montes *et al.* [212] demonstrated GaN/β-Ga_2O_3 p–n heterojunctions via mechanical exfoliation (Fig. 13a–i). Hao *et al.* [213] demonstrated the low defect density NiO/β-Ga_2O_3 p–n diode (Fig. 13j) with a high FOM of 0.65 GW cm^{-2} and a good ideality factor of 1.27, and enhanced breakdown voltage via thermal annealing (Fig. 13k). Furthermore, β-Ga_2O_3 is also being explored for photonic devices in applications such as all-optical switch supercontinuum, frequency comb and material characterization [214]. Basic nonlinear optical properties of β-Ga_2O_3 have been characterized including optical photoluminescence, Kerr effect, TPA and Raman scattering [215]. Due to its broadband transparency and small TPA coefficient, β-Ga_2O_3 is promising for high-performance, low-loss waveguides for integrated photonics [216–222]. Zhou *et al.* [215] demonstrated a low-loss 3.7 dB cm^{-1} β-Ga_2O_3 waveguide at 810 nm (Fig. 13l–m), which is comparable to the state of the art. They also comprehensively studied various loss mechanisms, including TPA and scattering from the sidewall, top surface and bulk, and revealed that waveguide geometry and operation wavelength could impact loss and dominant loss mechanisms. In addition, β-Ga_2O_3 has a small lattice mismatch with the III-N material system; therefore, β-Ga_2O_3 photonic devices can be integrated with III-N lasers and detectors. In addition, Ga_2O_3 is also suitable for deep UV photodetection [223–229] with self-power capability in heterojunction-based devices (Fig. 13n) [230].

Downloaded from https://academic.oup.com/ooms/article/2/1/itac004/6581087 by guest on 04 August 2022

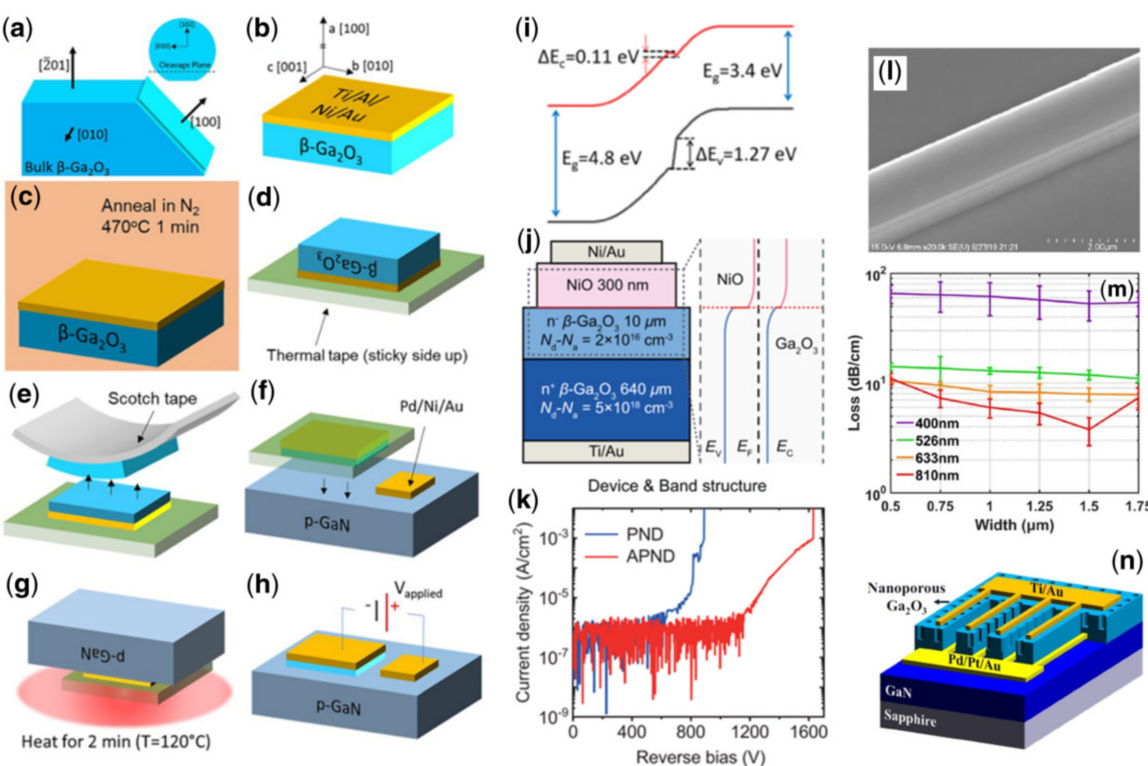

Figure 13: (a) The bulk (201) wafers of β-Ga_2O_3 can be cleaved and the (100) plane is exposed. The fabrication methods of GaN/β-Ga_2O_3 p–n diodes [212]; (b) metal deposition of the n-contact [212]; (c) annealing [212]; (d) thermal tape placement [212]; (e) mechanical exfoliation [212]; (f) β-Ga_2O_3 placed on p-type GaN [212]; (g) treatment on a hot plate [212]; (h) the finished device [212]. Reprinted with permission from Ref. [212]. Copyright 2019, AIP Publishing. (i) Simulated band diagram of GaN/β-Ga_2O_3 p–n junction [212]. Reprinted with permission from Ref. [212]. Copyright 2019, AIP Publishing. (j) Schematic structure and energy band diagram of vertical NiO/β-Ga_2O_3 heterojunction p–n diode [212]. (k) Reverse breakdown characteristics of the NiO/β-Ga_2O_3 devices [212]. Reprinted with permission from Ref. [212]. Copyright 2021, AIP Publishing. (l) SEM images of waveguide sidewall with optimized dry etching [212]. (m) Measured propagation loss of β-Ga_2O_3 waveguides with different widths and different wavelengths [212]. Reprinted with permission from Ref. [212]. Copyright 2021, SpringerLink. (n) Schematic structure of the Ga_2O_3/GaN heterojunction photodetectors [226]. From Ref. [226], licensed under a Creative Commons Attribution (CC BY) license.

PART III h-BN

h-BN material properties

Crystal structure

h-BN has a honeycomb structure, consisting of B and N atoms. The B and N atoms within the same hexagonal basal plane are bonded by sp^2 hybridized covalent bonds, while van der Waals forces connect adjacent layers, making h-BN a highly anisotropic material. The B–N bonds are also partial ionic because of the different electronegativity of B and N [231], resulting in the electrical insulation, high chemical stability and excellent mechanical properties of h-BN. The lattice constants of h-BN are $a = b = 2.5$ Å, $c = 6.6$ Å, whereas the B–N bond length is 1.45 Å and the spacing between two layers is 3.3 Å [232, 233]. Three different stacking modes of h-BN layers have been overserved with twist angles of $\theta = 0°$, $\theta = 60°$ and $\theta = 30°$, as shown in Fig. 14a and b [234]. The typical stacking of h-BN layers is AA′ with a twist angle of 60°, in which each B atom and N atom are exactly on top of the N atom and B atom in the bottom layer, respectively. The AB stacking is also observed in some h-BN samples with a twist angle of 0°. The stacking with a 30° twist angle, however, is rarely observed. The different stacking patterns can alter the electronic band structures of h-BN due to the different interlayer interactions [235]. Based on theoretical calculations, adjacent BN layers may have a nearly free slide path from AA′ stacking to AB stacking with a bandgap shrinking of 0.6 eV [236].

The orientation of the atoms in a layer can be divided into a zigzag configuration and an armchair configuration as shown in Fig. 14c [237]. Based on first-principle calculations, Du *et al.* [238] reported that the edge configurations might also have an influence on the bandgap of h-BN. The bandgap of h-BN can transform from indirect to direct bandgap with a transition from zigzag edge to armchair edge. The morphology and structure of h-BN can be characterized by a series of techniques, including optical microscope, X-ray photoelectron microscopy, Raman spectroscopy, electron energy loss spectroscopy, transmission electron microscopy (TEM), atomic force microscopy (AFM) and scanning electron microscopy (SEM) [239–242].

Electronic properties

H-BN is a UWBG material that can be used as an insulator owing to the partial ionic B–N bonds. The bandgap of h-BN has been both predicted by theoretical calculations and characterized by experiments. Early theoretical calculations based on the tight-binding method suggested h-BN was a direct bandgap material [243] while the density functional theory (DFT) method indicated an indirect bandgap and the values of the bandgap also varied from 4.027 to 4.47 eV [244–246]. Later, a more accurate method, GW calculations, yielded an indirect bandgap of 6.0 eV [247]. Early experimental work showed that h-BN was a direct bandgap material with a strong luminescence peak at 5.76 eV [248]. In 2016, Cassabois *et al.* [249] demonstrated the indirect nature of the

Downloaded from https://academic.oup.com/ooms/article/2/1/itac004/6581087 by guest on 04 August 2022

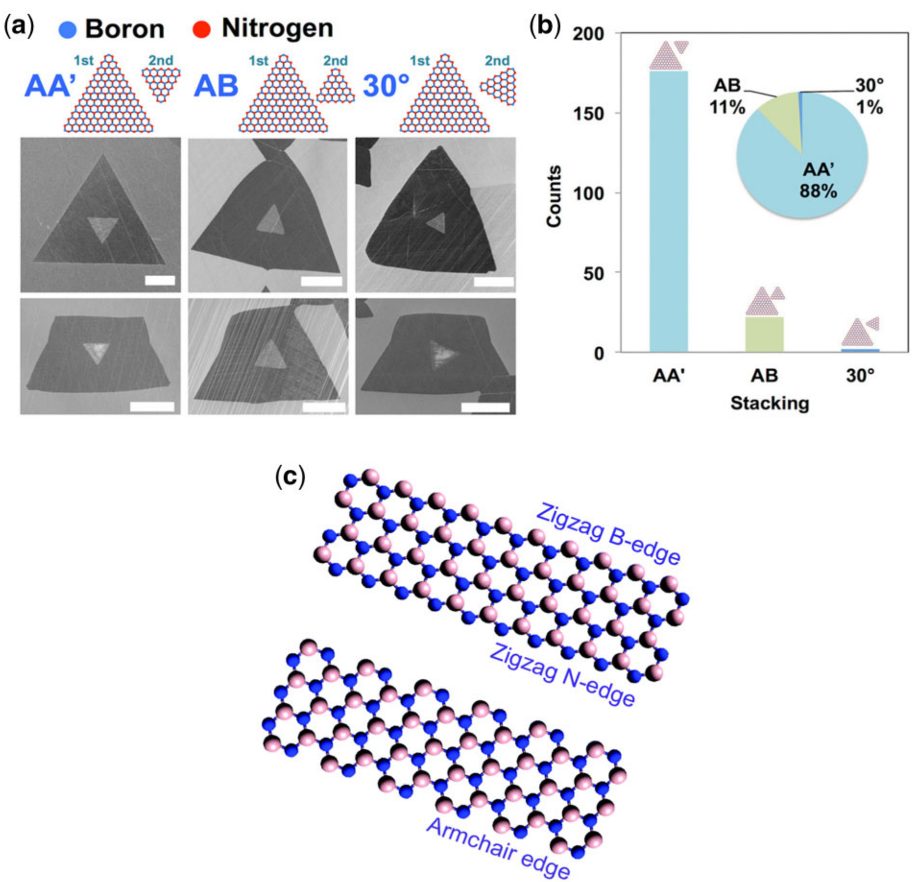

Figure 14: (a) Schematics and SEM images of the different stacking configurations of h-BN [234]. Reprinted with permission from Ref. [234]. Copyright 2017, American Chemical Society. (b) Statistics of three different stacking configurations [234]. Reprinted with permission from Ref. [234]. Copyright 2017, American Chemical Society. (c) Schematics of zigzag and armchair edge configurations of h-BN [237]. Reprinted with permission from Ref. [237]. Copyright 2014, Royal Society of Chemistry.

bandgap at 5.955 eV. The discrepancies may be attributed to the different stacking methods and edge termination [250, 251]. In addition, h-BN possesses a relatively large dielectric constant [252, 253]. The dielectric constant in the in-plane direction is higher than that in the out-of-plane direction due to the polar in-plane B–N bonding. Laturia *et al.* [252] demonstrated that the in-plane dielectric constant is independent of the number of layers while the out-of-plane dielectric constant increases with the increase of the number of layers. Hattori *et al.* [254, 255] extensively studied the dielectric breakdown of h-BN. Using C-AFM, they reported that the electric field strength along the *c*-axis of h-BN was around 12 MV cm^{-1}, similar to traditional dielectric material SiO_2. However, the electric field strength of h-BN perpendicular to the *c*-axis was only around 3 MV cm^{-1} due to the anisotropic property of h-BN.

Optical properties

h-BN nanosheets have no optical absorption in the range of visible light, which makes them highly transparent [239, 256, 257]. As for the DUV range, a strong peak around 200 nm could be observed, corresponding to an optical bandgap around 6 eV [256, 257]. h-BN also possesses strong DUV emission by a phonon-assisted recombination process, as shown in Fig. 15a [249]. Similar to PL emission, h-BN exhibits a strong CL emission in the DUV range, which makes it an excellent candidate for UV photonics, as shown in Fig. 15b [258–260]. As shown in Fig. 15c and d, the Raman spectrum of h-BN nanosheets is around 1366 cm^{-1} and the Fourier-transform infrared spectroscopy (FTIR) spectrum of the BN nanosheet displays a strong absorption peak at 811 cm^{-1} and a broad absorption band in-between 1350 and 1520 cm^{-1} [259, 261].

There are many types of defects existing in h-BN, such as boron vacancies, NVs and antisite defects. While these defects may be detrimental to some properties of h-BN, it makes h-BN a promising platform for quantum photonics. In 2015, Tran *et al.* [262] first reported SPEs from a point defect, N_BV_N in h-BN. Linearly polarized SPEs have been observed in h-BN with high brightness and quantum efficiency, which are optically stable even at room temperature. The defects in h-BN can form naturally during the growth of crystals or be engineered by electron beam irradiation, plasma processing and thermal annealing [263, 264]. Generally, SPEs in h-BN can be excited by blue and green lasers. However, UV emissions can also be obtained by using cathodoluminescence with extremely bright emissions at 4.1 eV [265].

Nonlinear optical properties of h-BN are also their important features, including second-harmonic generation (SHG) and TPA. SHG can be detected in h-BN with AB stacking due to the breaking of inversion symmetry [266]. Only h-BN flakes with an odd number of layers have a strong SHG signal, while h-BN samples with an even number of layers exhibit negligible signals due to the cancelation of signals [267]. Kumbhakar *et al.* [268] first reported TPA in h-BN nanosheets by using laser radiation with the Z-scan technique. The highest value of the TPA cross-section of h-BN nanosheets is ≈52 times larger than an efficient

Downloaded from https://academic.oup.com/ooms/article/2/1/itac004/6581087 by guest on 04 August 2022

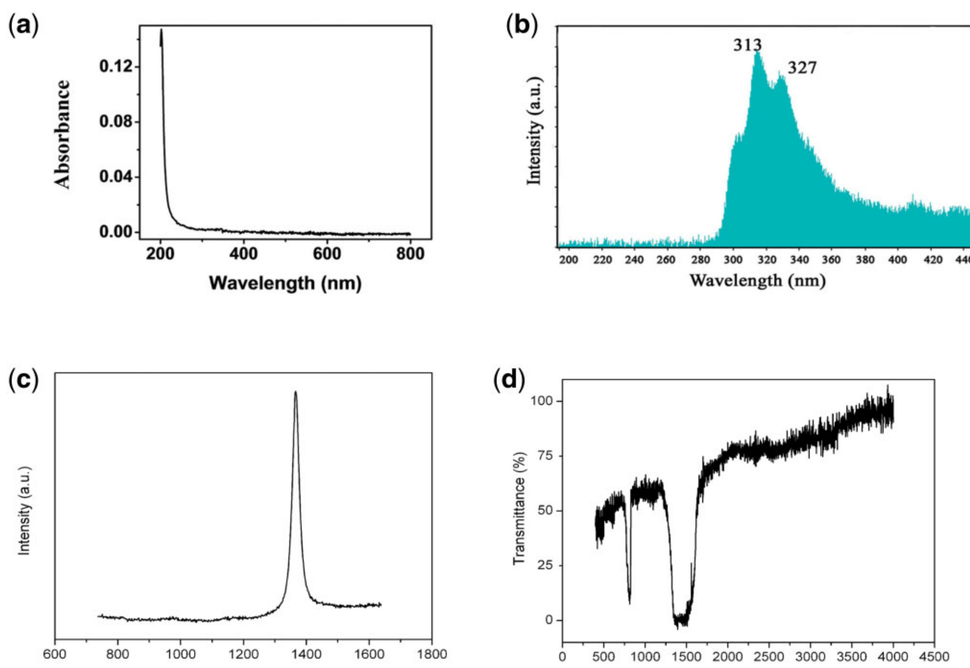

Figure 15: (**a**) Absorption spectrum of the h-BN thin film [257]. Reprinted with permission from Ref. [257]. Copyright 2010, American Chemical Society. (**b**) CL spectrum from the BN nanosheets [258]. Reprinted with permission from Ref. [258]. Copyright 2009, American Chemical Society. (**c**) Raman and (**d**) FTIR spectra of h-BN nanosheets [259]. Reprinted with permission from Ref. [259]. Copyright 2010, American Chemical Society.

TPA active material. Attaccalite *et al.* [269] calculated the TPA process in single-layer and bulk h-BN with an *ab initio* real-time Bethe–Salpeter method and a tight-binding approach, demonstrating that TPA is capable of detecting the lowest 1s exciton in the monolayer and bulk h-BN.

Thermal and mechanical properties

The thermal conductivity of monolayer h-BN and bulk h-BN has been calculated by the Boltzmann transport equation [270]. Superior thermal conductivity k at room temperature of more than 600 W m^{-1} K^{-1} has been predicted for single-layer h-BN, which is less than graphene but larger than bulk h-BN. With increasing layer numbers, bulk h-BN has a stronger scattering phonon–phonon scattering than single-layer h-BN, which can reduce the thermal conductivity. Moreover, compared with monolayer h-BN, bulk h-BN has smaller out-of-plane vibrations due to the interlayer coupling, causing decreased thermal conductivity [237, 271]. Except for its extraordinary thermal properties, the mechanical properties of h-BN have also been well investigated by theoretical calculations such as DFT as well as experimental techniques like AFM. Peng *et al.* [272] reported the in-plane Young's modulus of 279.2 N m^{-1} for single-layer h-BN using DFT calculations. The tensile rigidity from 0.184 to 0.328 Tpa nm and the shear rigidity from 0.171 to 0.184 Tpa nm for h-BN nanosheets were predicted by an analytical molecular mechanics approach [273]. The modulus of h-BN is affected by both layer numbers and defects. Song *et al.* [239] measured the mechanical properties of h-BN by nanoindentation and theoretical simulation, demonstrating that the stiffness and the breaking strength of h-BN can be reduced by vacancy defects. Both DFT calculations and AFM measurements have shown that the modulus of h-BN increases with decreasing sheet thickness [274, 275].

h-BN synthesis

Exfoliation

Mechanical cleavage or mechanical exfoliation using the pulling force to separate layered materials bonded by vdW force was first employed to obtain graphene monolayers by the 'Scotch tape method' in 2004 [276]. It could also be applied to other two-dimensional thin films like BN, MoS_2 and $NbSe_2$ [277]. Novoselov *et al.* [277] demonstrated the first successful realization of h-BN layers by mechanical exfoliation, where h-BN layers were peeled off with tape and then transferred to a substrate. h-BN layers obtained using this method have high crystallinity, paving the way to understanding the fundamental physical properties and mechanisms in h-BN [278–280]. However, the h-BN flake size was less than several micrometers because the source material was BN powders of a few micrometers. Another drawback of this method was that it was hard to get few-layer and monolayer h-BN owing to the strong lip–lip interactions between BN layers. Instead of using pulling forces, another method called ball milling uses shear forces to break the vdW bonding between adjacent layers. One of the pioneer works was achieved by Li *et al.* [281] in 2011, where they mixed the h-BN powder with benzyl benzoate to diminish the ball impacts and contamination, as shown in Fig. 16. Some important parameters in this process are milling ball size, milling speed, milling agent and ball-to-powder ratio [281, 282]. For example, high-energy ball mills can produce strong forces to break particles and crystalline structures. On the contrary, a planetary mill can only apply shear forces on the milling materials [281]. In 2008, Han *et al.* [283] first exploited the growth of mono- and few-layer h-BN nanosheets by a chemical-solution-derived method. They put h-BN single crystals into a 5-ml 1,2-dichloroethane solution of poly (*m*-phenylenevinylene-co-2,5-dictoxy-*p*-phenylenevinylene) for sonication, which could disperse and fracture the crystals into h-BN nanosheets. To effectively exfoliate h-BN nanosheets, a variety of solvents have been applied to sonicate

Downloaded from https://academic.oup.com/ooms/article/2/1/itac004/6581087 by guest on 04 August 2022

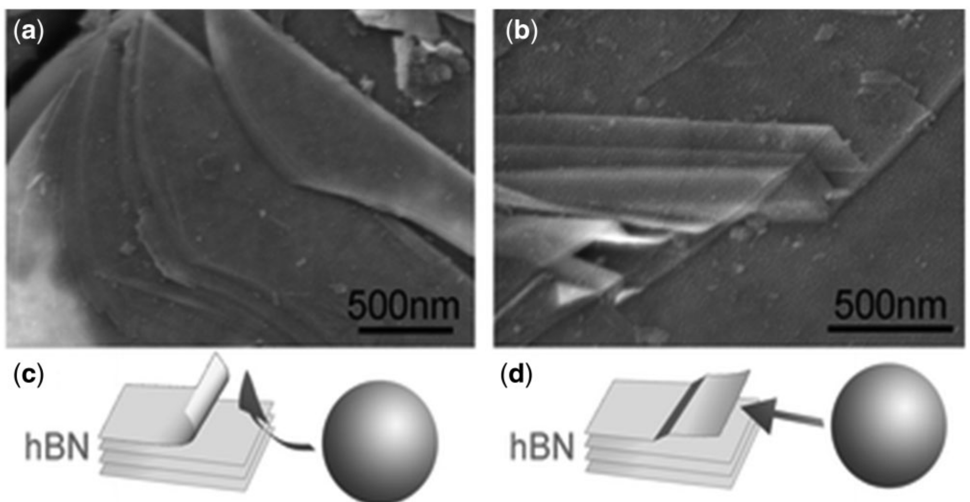

Figure 16: (a) and (b) SEM images of h-BN nanosheets produced by two different exfoliating mechanisms. (c) and (d) h-BN nanosheets exfoliated from the edge and h-BN nanosheets cleavage from the top surface, respectively [281]. Reprinted with permission from Ref. [281]. Copyright 2011, Royal Society of Chemistry.

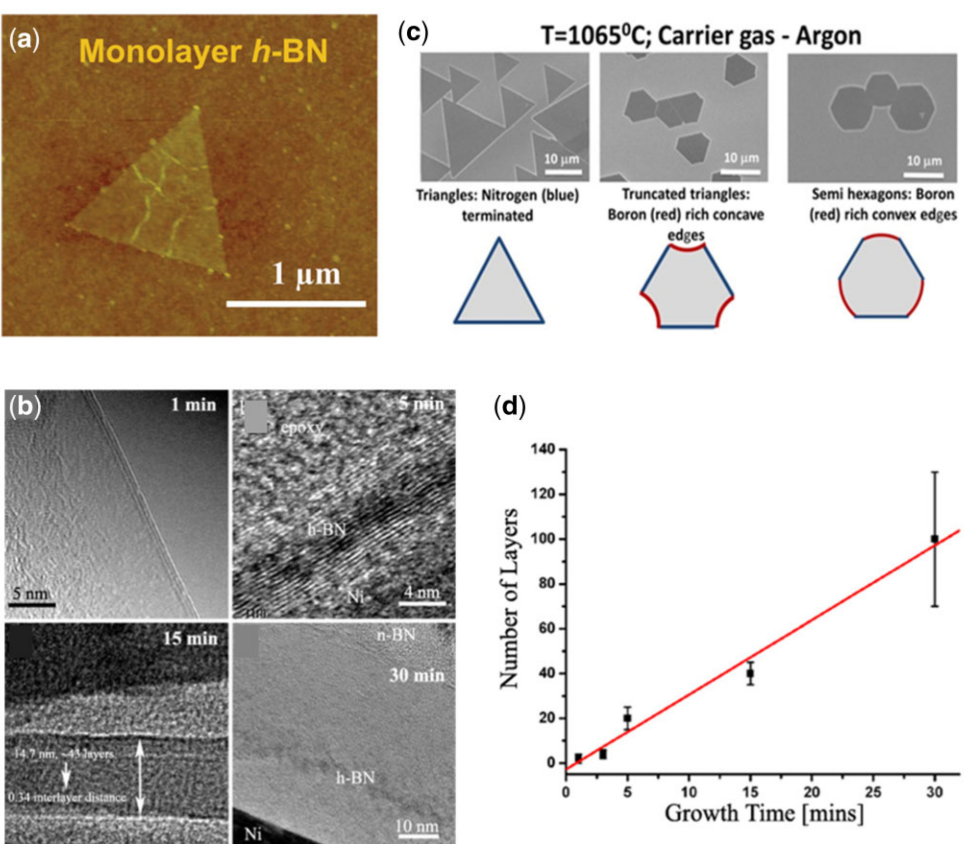

Figure 17: (a) Monolayer h-BN with a triangular shape [256]. Reprinted with permission from Ref. [256]. Copyright 2012, American Chemical Society. (b) Top: SEM images of h-BN grown at 1065°C. Bottom: Schematic of the shape and termination of the correlated h-BN [294]. Reprinted with permission from Ref. [294]. Copyright 2015, American Chemical Society. (c) TEM images of h-BN thin films grown by CVD for 1, 5, 15 and 30 min. Reprinted with permission from Ref. [298]. Copyright 2012, American Chemical Society. (d) Number of h-BN layers as a function of growth time [298]. Reprinted with permission from Ref. [298]. Copyright 2012, American Chemical Society.

the h-BN crystals, including *N*,*N*-dimethylformamide (DMF), 1,2-dichloroethane and molten salts [241, 284, 285]. For example, DMF, a strong polar solvent whose surface energy can overcome the van der Waals forces, can efficiently exfoliate h-BN via the interactions between the DMF molecules and the h-BN [241].

Chemical vapor deposition

CVD is one of the most popular methods to fabricate 2D materials, including graphene, transition metal dichalcogenides (TMDs) and h-BN [286–288]. The pioneering work of h-BN grown by CVD was done by Paffett *et al.* [289] in 1990, where they grew

Downloaded from https://academic.oup.com/ooms/article/2/1/itac004/6581087 by guest on 04 August 2022

h-BN on Pt(111) and Ru(111) surfaces by the adsorption and decomposition of borazine. Other metal substrates have also been widely applied for the growth of h-BN, including Cu [239, 256, 290], Ni [291–293], Au [294] and Cu–Ni alloy [295]. Kim *et al.* [256] exploited the low-pressure CVD growth of monolayer h-BN on Cu substrate, in which h-BN preferred to form a triangular shape because N-terminated edges are more energetically favored, as shown in Fig. 17a. The ratio of N and B can determine the shape of h-BN crystals. Stehle *et al.* [294] reported that the evolution of h-BN shape from triangular shape to truncated triangles and finally to hexagonal shape is controlled by the distance between the precursor and the Cu substrate along with the increased ratio of B to N (Fig. 17b). The size, shape and number of layers of h-BN crystals can be readily tuned during CVD growth. To increase the size of h-BN, it is essential to reduce the nucleation density on the substrates. Lu *et al.* [295] suggested that the nucleation density can be greatly reduced by using rational designed Cu–Ni alloy. When adding 10–20 atom% Ni, the growth is controlled by the surface-mediated mechanism on Cu substrates. With increased Ni concentration, the growth is decided by the solid–gas reactions of Ni–B and Ni–N. Lee *et al.* [296] reported the synthesis of wafer-scale single-crystal h-BN on molten Au anchored on W foil. During the growth process, the h-BN grains merge into a hexagonal structure without the formation of grain boundaries. The feeding rate of precursor gases also plays an important role in the enlargement of h-BN. Song *et al.* [297] successfully prepared large single-crystal h-BN domains up to 72 μm by using a folded Cu-foil, which reduced the feeding rate of the precursor and the nucleation density. Ismach *et al.* [298] showed that the thickness of h-BN can be tuned by parameters such as temperature, time and gas precursors. They used ammonia and diborane as gas precursors for N and B and performed the CVD growth above 800°C. Under such a condition, the number of layers has a linear relationship with time, which can facilitate the thickness control of h-BN (Fig. 17c and d).

Physical vapor deposition

There are several types of physical vapor deposition methods used in growing h-BN, including pulsed laser deposition (PLD) [299, 300], atomic layer deposition (ALD) [301], sputtering [302–306] and MBE [307, 308]. Sajjad *et al.* systematically studied the synthesis of single-crystal and polycrystalline h-BN nanosheets via CO_2-PLD with a size up to $50 \times 50\ \mu m^2$, as indicated in Fig. 18a. They used carbon-doped h-BN nanosheets to fabricate Schottky diode with reserve breakdown voltage around −70 V and gas sensors for CH_4 [299, 300]. Orlander *et al.* [301] grew h-BN thin films by both ALD and laser-assisted ALD (LALD) while LALD offered a higher growth rate and better stability. Sputtering growth of h-BN has been achieved on different substrates including Ru, Au, Ni, Cu and AlN [302–306]. Sutter *et al.* [302] used magnetron sputtering to deposit h-BN films with controllable thickness on Ru(0001) substrates (Fig. 18b). Nakhaie *et al.* [307] demonstrated the synthesis of h-BN thin films on Ni foil by MBE with temperatures around 730–835°C. Later, they have achieved the h-BN/graphene heterostructures by MBE, which offers a pave for the production of large-area uniform 2D heterostructures [308].

h-BN devices and applications

Electronics

Owing to its UWBG, relatively large dielectric constant and high breakdown electric field, h-BN serves as an outstanding dielectric material in transistors and capacitors. h-BN has long been used as a gate dielectric in diamond field-effect transistors (FETs). Diamond FETs suffer greatly from the defects in the amorphous gate dielectric and poor dielectric/diamond interface, which degrade the carrier mobilities. h-BN, on the other hand, possesses a flat and defect-free surface, which largely reduces the defect densities at the interface when used in diamond FETs. Sasama *et al.* [309] fabricated such FETs with high mobility (>300 $cm^2\ V^{-1}\ s^{-1}$) and low sheet resistance (<3 kΩ), as shown in Fig. 19a and b. Recently, Yang *et al.* [310] deposited h-BN in AlGaN/GaN metal–insulator–semiconductor high electron mobility transistors (MISHEMTs) as a gate dielectric, resulting in extremely low off-state current of 10^{-8} mA $mm^{-1}$and high on/off ratio of 10^9. Bendable capacitors using h-BN as the insulator layer were achieved by Guo *et al.* [311] where they transferred the h-BN thin film to a polyethylene terephthalate (PET) film with Au electrodes. The capacitors have stable performance under bending and have a dielectric strength of around 9 MV cm^{-1}.

Having a flat and inert surface with few defects and dangling bonds, h-BN is an outstanding substrate and an excellent encapsulation material, especially for low-dimensional materials such as graphene and TMDs. Dean *et al.* [312] fabricated graphene-on-h-BN devices with extremely high hall mobility of 40,000 $cm^{-2}\ V^{-1}\ s^{-1}$ at room temperature by transferring bilayer graphene onto the h-BN substrate. Yang *et al.* [313] demonstrated the direct epitaxial growth of large-area single-crystal graphene on h-BN substrates with a fixed stacking order by a remote plasma-enhanced CVD method. Lee *et al.* [314] encapsulated MoS_2 with h-BN to form MoS_2 FETs, which improved the stabilities of the devices with little mobility degradation and

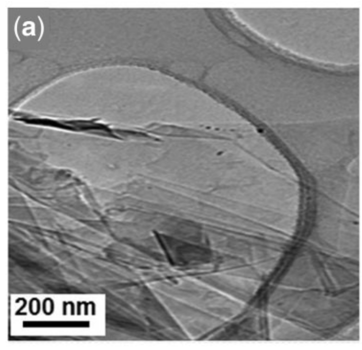

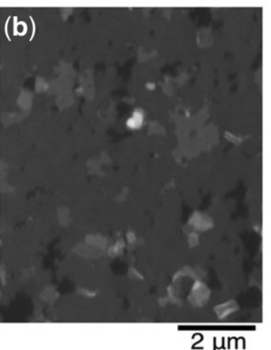

Figure 18: (a) A TEM image of h-BN made by CO_2-PLD [300]. Reprinted with permission from Ref. [300]. Copyright 2013, American Chemical Society. (b) SEM image of a three-layer h-BN film on Ru(0001)/Al_2O_3 by magnetron sputtering [302]. Reprinted with permission from Ref. [302]. Copyright 2013, American Chemical Society.

Downloaded from https://academic.oup.com/ooms/article/2/1/itac004/6581087 by guest on 04 August 2022

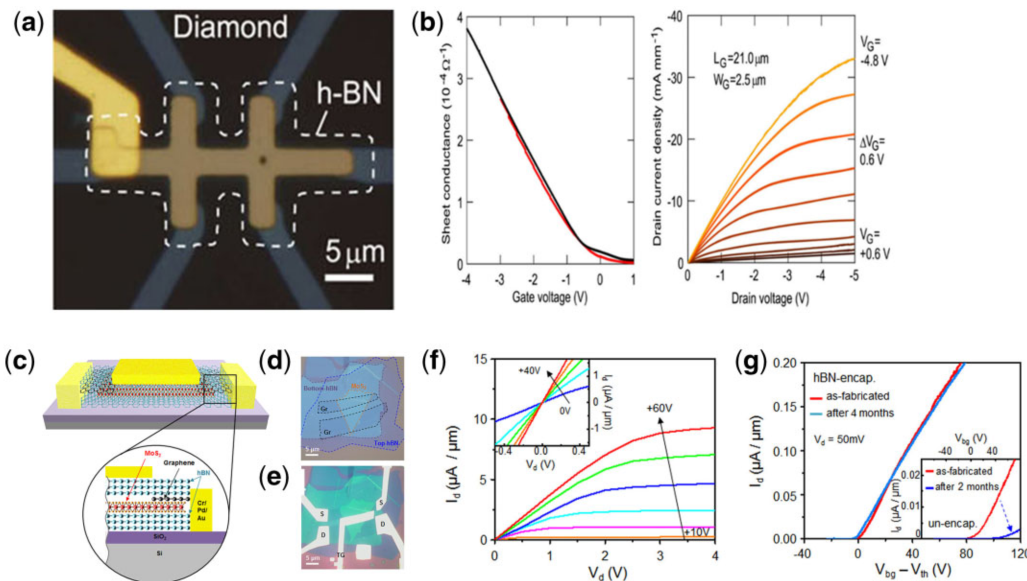

Figure 19: (a) Optical micrograph image of diamond FETs using h-BN as gate dielectric [309]. (b) Transfer and output characteristics of diamond FETs [309]. From Ref. [309], licensed under a Creative Commons Attribution (CC BY) license. (c) Schematic of the MoS_2 FET encapsulated by h-BN [314]. (d) The optical image of h-BN/graphene/MoS_2/h-BN heterostructure [314]. (e) The optical image of the MoS_2 FET encapsulated by h-BN [314]. (f) Output characteristics of the MoS_2 FET. The inset shows the Ohmic contact between graphene and MoS_2 [314]. (g) Transfer characteristics of the MoS_2 FET encapsulated by h-BN without degradation after 2 months. The inset shows the transfer characteristics of the MoS_2 FET without encapsulation [314]. Reprinted from Ref. [314] with permission. Copyright 2015, American Chemical Society.

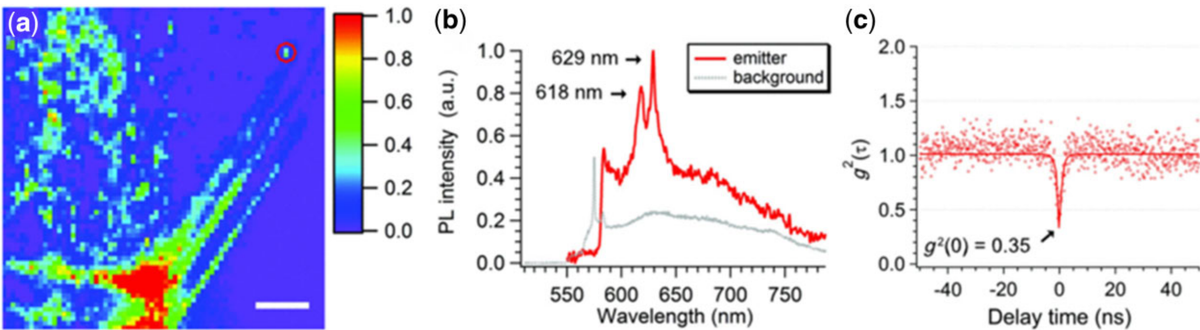

Figure 20: (a) A confocal map of bulk h-BN displaying an isolated emission center and other ensemble emissions [318]. (b) A photoluminescence spectrum of the isolated emission center circled in the confocal map at room temperature [318]. (c) A second-order autocorrelation measurement from the emitter center in (b) shows a dip of ~0.35 [318]. Reprinted with permission from Ref. [318]. Copyright 2016, American Physical Society.

threshold voltage shifts in the ambient for 2 months, as shown in Fig. 19c–g.

Photonics

Due to its excellent optical properties, h-BN serves as a promising platform for photonic applications. With an UWBG (~6.0 eV) and strong UV absorption and emission, h-BN is an outstanding material for optoelectronics in the DUV range, including DUV detectors, emitters and lasers [283, 315–317]. Li *et al.* [316] fabricated h-BN epilayer-based metal–semiconductor–metal detectors with a cut-off wavelength at 230 nm and a breakdown electric field of about 4.4 MV cm^{-1}. Watanabe *et al.* used the HPHT method to grow h-BN single crystals, which showed a sharp UV luminescence peak at 215 nm and lased under electron-beam excitation [283]. The defects in h-BN provide a platform for exploring exciting quantum properties and applications. As mentioned above, h-BN is extremely suitable for SPE. Besides their work in quantum emission of h-BN monolayers [295], Tran *et al.* [318] also observed room temperature SPE in bulk h-BN in the visible and the near-infrared spectrum with a lifetime near 1.0 ns, as shown in Fig. 20. Furthermore, Gottscholl *et al.* [319] realized the room-temperature optical initialization and read-out of V_B^- defect centers with D_{3h} group symmetry in h-BN. Based on electron paramagnetic resonance (EPR) spectroscopy and optically detected magnetic resonance (ODMR) measurements, they found that the defect in h-BN has a triplet ground state and a ZFS of ~3.5 GHz. They also achieved the optical polarization by optical pump, which is a primary step for coherent spin manipulation.

Other applications

With extraordinary thermal conductivity and excellent mechanical properties, h-BN is a crucial material to combine with polymers to enhance their thermal and mechanical performance. h-BN has been widely introduced into polymers as nanofillers to produce thermal conductive composites and improve their mechanical strength [241, 320–324]. For example, with the incorporation of only 0.3 wt% h-BN nanosheets, the coefficient of

Downloaded from https://academic.oup.com/ooms/article/2/1/itac004/6581087 by guest on 04 August 2022

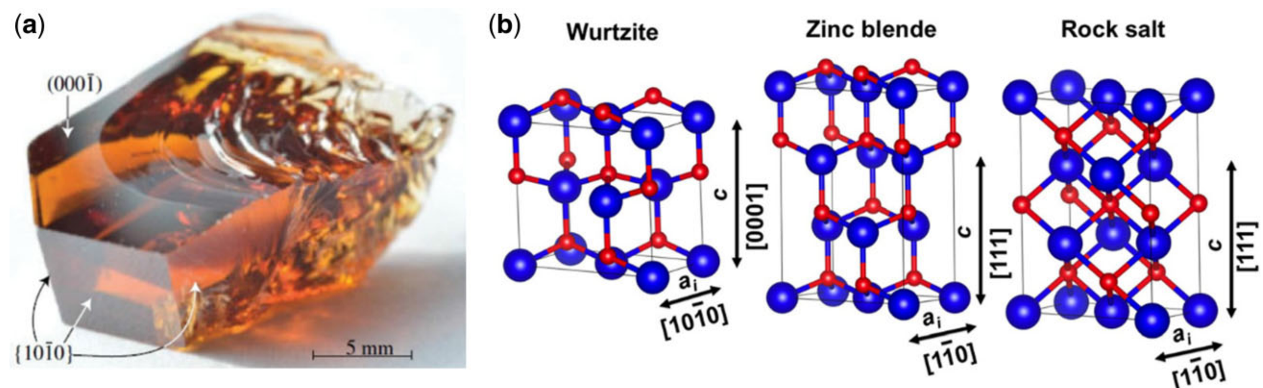

Figure 21: (a) Photograph of a bulk AlN crystal [327, 328]. Reprinted with permission from Ref. [327]. Copyright 2013, IOP Science. (b) Schematics of wurtzite, zinc blend and rock salt structures of AlN [326]. Reprinted with permission from Ref. [326]. Copyright 2016, AIP Publishing.

thermal expansion of PMMA was largely reduced from 184 to 160 ppm $^{\circ}C^{-1}$, and the elastic modulus was enhanced from 1.74 to 2.13 GPa [241]. The orientation of h-BN nanosheets can influence the thermal conductivity of composites owing to the anisotropic nature of h-BN. Cho *et al.* [322] used magnetic fields to obtain vertically or horizontally aligned h-BN nanosheets in polysiloxane/BN nanosheets composite films. Both the thermal conductivity and the transmittance of composite films were improved due to the preferred orientation.

PART IV ALN

AlN materials and synthesis

AlN has an UWBG of 6.1 eV [325], wide spectral transparency from UV to mid-infrared wavelength and a high critical electric field of ~12 MV cm^{-1}. AlN has three crystal structures (Fig. 21), including cubic zinc blende, hexagonal wurtzite and rock salt [326]. With the largest bandgap (~6.1 eV) among the commonly used semiconductors, the hexagonal AlN is the most widely studied and is relatively easy to grow. The cubic zinc blende and rock salt AlN are metastable and require extreme growth conditions. In the following section, we will introduce wurtzite AlN due to its wide applications.

To date, both bulk AlN crystals and epitaxial AlN thin films have been demonstrated. For bulk AlN growth, the common single crystal growth technologies such as hot melt and solution growth methods are challenging [328–331], because AlN crystals have an ultra-high melting point of ~2800°C and a high dissociation pressure of 20 MPa [328]. Currently, bulk AlN crystals are usually grown by physical vapor transport (PVT) method [332–336] with a low dislocation density of $<10^4$ cm^{-2} and no low-angle grain boundaries. There are usually two substrates used for the large-size AlN PVT growth process: small-size AlN seeds through multi-step iterative growth and large-size SiC seeds [337–340]. The former has a very low growth rate and the latter might be a potential substrate for growing large-area AlN crystals [341]. However, there are some challenges to using SiC seeds, including contamination of silicon and carbon, cracking [336, 342–344], thermal expansion coefficient mismatch and defect generation. Hu *et al.* [342] optimized PVT growth parameters for growing AlN layers on SiC, where SiC substrates with off-axis angles and Si-face were beneficial for improving surface morphology and crystalline quality. Gamov *et al.* [345] investigated the point defect and the resultant photochromism in PVT-grown AlN using UV irradiation and observed pairs of complementary absorption bands 2.6–4.8 and 3.4–4.5 eV along with several different absorption bands.

For epitaxially grown AlN films, many substrates have been utilized, including SiC [344, 350–353], Si [354, 355], AlN [356–359], sapphire [346, 350–364], diamond [365] and polyimide [366, 367]. Sapphire is a widely used substrate for AlN epitaxial growth due to its relatively low cost. However, AlN on sapphire exhibits high threading dislocation density (TDD), which can increase current leakage and compensate free carriers in doped layers, especially for n-type AlN film [361, 368]. SiC and Si substrates are usually used for large-area AlN growth via self-seeds technology [341]. But high-temperature growth methods would lead to the formation of an interfacial layer between AlN and SiC or Si substrates and degraded interfaces. Several epitaxy methods, including MOCVD, MBE, PLD and sputtering, have been demonstrated for the AlN epitaxial growth. When AlN films are grown on sapphire substrates using MOCVD, the TDD of the films is usually ~10^8–10^{10} cm^{-2}. This high TDD can be reduced below ~10^8 cm^{-2} by epitaxial lateral overgrowth (ELO) with low-temperature MOCVD [346, 369]. Long *et al.* [370] reported crack- and strain-free AlN epilayers with a thickness of up to 10.6 μm using MOCVD on patterned sapphire substrates. Demir *et al.* [346] explored a sandwich temperature method to grow thick AlN epilayers with improved crystal quality and surface morphology, where a relatively low-temperature thick AlN layer was sandwiched between two high-temperature thin AlN layers (Fig. 22a). Washiyama *et al.* [371] revealed that post-growth thermal annealing could further reduce the defect density via the dislocation climbing through vacancy core diffusion processes. Moreover, the MOCVD-grown AlN epilayers on AlN single-crystal substrates have a low TDD of ~10^3 cm^{-2} [372], which is close to that of the bulk AlN crystals.

MBE growth of AlN has been demonstrated since 1998 using sapphire substrates [337]. And the modification of nitridated sapphire surface before the AlN growth that combines the deposition of a small amount of Al (1–2 monolayers) and a subsequent surface treatment under ammonia flux was the key to the improvement of surface morphology [373]. Yin *et al.* [347] grew AlN thin films on Si by MBE on a nanowire template under a nitrogen (N)-rich environment (Fig. 22b–d). Nemoz *et al.* [374] studied the effect of high-temperature post-annealing in N_2 on AlN films, where the annealing conditions had a strong influence on the surface roughness and morphology of AlN films. The optimized post-annealing process can lead to a significant reduction in both edge and mixed threading dislocations. When

Downloaded from https://academic.oup.com/ooms/article/2/1/itac004/6581087 by guest on 04 August 2022

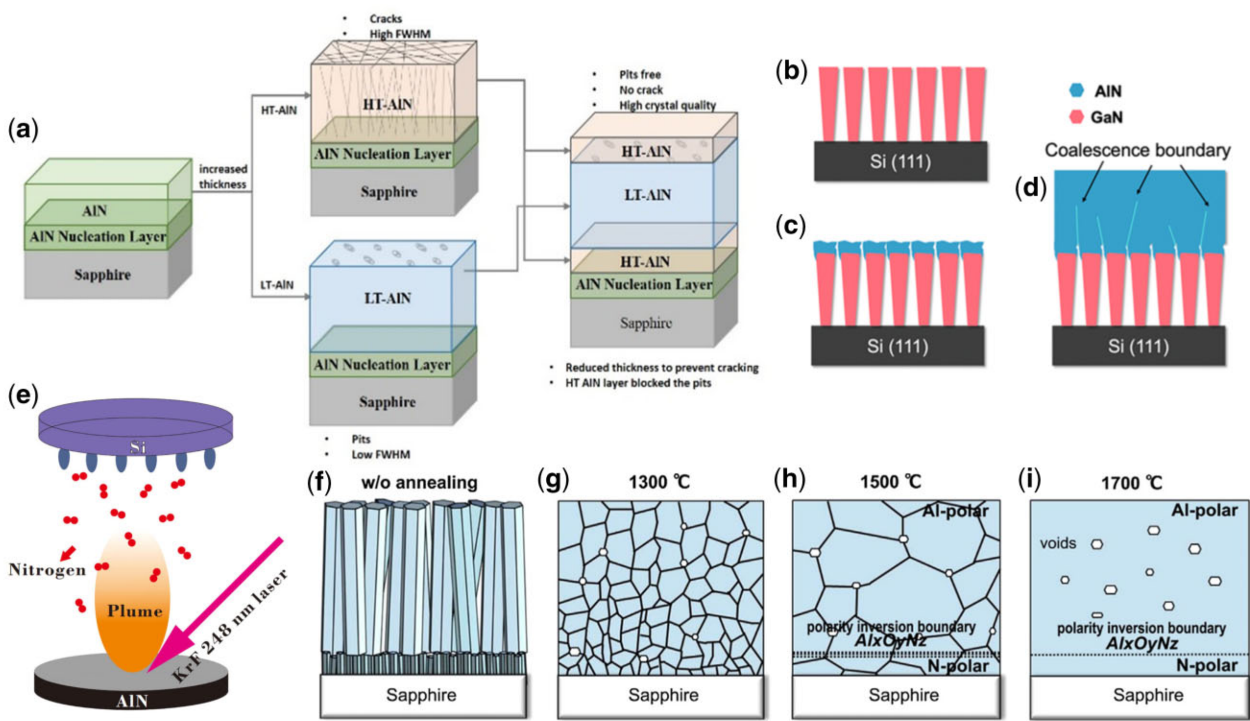

Figure 22: (a) Schematic of sandwiched low-temperature (LT) AlN between high-temperature (HT) AlN layers [346]. Reprinted with permission from Ref. [346]. Copyright 2018, IOP Publishing, Ltd. (b)–(d) MBE growth of nanoscale AlN crystals on the GaN nanowire template [347]. Reprinted with permission from Ref. [347]. Copyright 2021, American Physical Society. (e) Illustration of PLD growth of AlN film [348]. (f)–(i) Mechanism of sputtered AlN film quality improvement at different annealing temperatures [349]. Reprinted with permission from Ref. [349]. Copyright 2018, Elsevier.

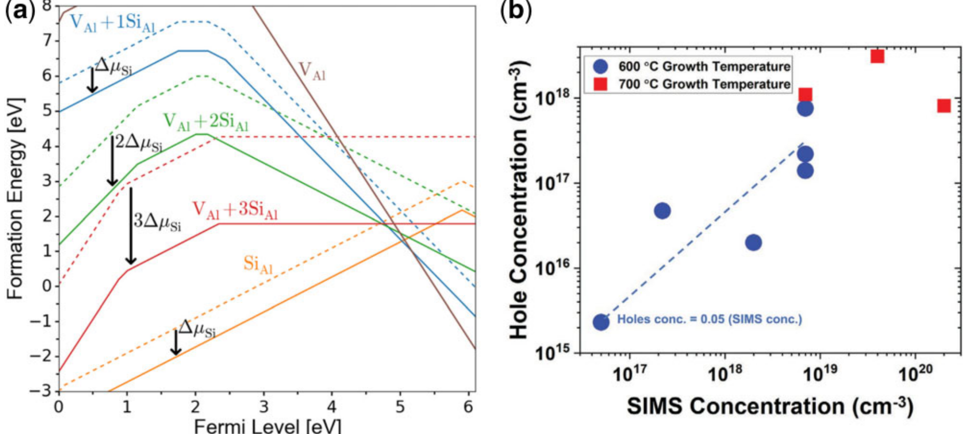

Figure 23: (a) Formation energy as a function of Fermi level for V_{Al}, Si_{Al} and $V_{Al} + nSi_{Al}$ complexes. The dotted and solid lines represent the low and high [Si] sides of the compensation knee, respectively [384]. Reprinted with permission from Ref. [384]. Copyright 2018, AIP Publishing. (b) Hole concentration as a function of SIMS concentration in Be doped AlN [392]. Reprinted with permission from Ref. [392]. Copyright 2021, John Wiley and Sons.

using Si or SiC substrates, PLD is a preferable choice for improving interface quality due to the lower growth temperature [348, 360, 375–377], where its schematic is shown in Fig. 22e. The interfacial reactions between AlN films and Si or SiC substrates can be effectively controlled by reducing the amorphous interfacial layer (e.g. SiAlN) between AlN and the substrate [348]. For the sputtering growth of AlN films, Shojiki's group used a sintered AlN target and high-temperature face-to-face annealing and reduced dislocation density with increasing AlN film thickness [378]. Liu *et al.* [379] demonstrated the polarity tunning between N-polar AlN and Al-polar AlN with different gases during sputtering. And the improvement mechanism by high-temperature annealing in nitrogen ambient was revealed [349], as shown in Fig. 22f–i.

Current status of AlN doping

Effective n-type doping in AlN is critical to realizing AlN-based devices for various electronic and photonic applications. In the last two decades, silicon has been the most common donor in AlN [380–383]. In GaN, Si is a shallow donor. However, with increasing Al, silicon is always not a shallow donor in AlGaN [384]

Downloaded from https://academic.oup.com/ooms/article/2/1/itac004/6581087 by guest on 04 August 2022

due to the DX transition near the CB edge with ionization energy up to 150–200 meV [385]. Furthermore, a compensation knee phenomenon was observed in AlN with increasing Si doping. At low Si doping, an increase in the Si concentration leads to a commensurate increase in free electrons; however, increasing Si concentrations reduces free electron concentrations at high Si doping. Harris *et al.* [384] proposed a mechanism to explain the compensation knee observed in the Si doping in AlN, where the $V_{Al} + nSi_{Al}$ complexes (*n* is the number of Si atoms in the complex) play a key role. As shown in Fig. 23a, the formation energies of the $V_{Al} + nSi_{Al}$ complexes change with Si chemical potential at different rates controlled by *n* values. The $V_{Al} + 2Si_{Al}$ and $V_{Al} + 3Si_{Al}$ complexes are more impacted by changes in Si availability than $V_{Al} + 1Si_{Al}$ and Si_{Al} [384]. In low Si doping, the dominant Si_{Al} and V_{Al} determine the Fermi level, where the Fermi level (free electron concentration) increases with increasing Si doping. In high Si doping, $V_{Al} + 2Si_{Al}$ and $V_{Al} + 3Si_{Al}$ complexes dominate and the Fermi level (free electron concentration) decreases with increasing Si doping. To date, high n-type conductivity and free electron concentration of Si-doped AlN film can only be achieved when the TDD of the film is extremely low, such as in bulk AlN or AlN epitaxially grown on single-crystal AlN substrates. Breckenridge *et al.* [386] demonstrated Si implanted AlN film on single-crystal AlN with a free electron concentration of 5×10^{18} cm^{-3} and ionization energy of 70 meV by a non-equilibrium annealing process. In addition, it is also important to suppress the self-compensation process, which can be realized via V_{Al}–nSi_{Al} complexes by defect quasi-Fermi level (dQFL) control [386]. Mg, Be and Na are potential acceptors in AlN by first-principle calculations [387]. Mg is the most commonly used acceptor in GaN [388], but the ionization energy of Mg in AlN is 500–630 meV, which makes it difficult to realize high conductivity p-type AlN films [389–391]. Recently, Be-doped p-type AlN was experimentally demonstrated with a high hole concentration of 5×10^{18} cm^{-3} [392]. As shown in Fig. 23b, the average Be activation efficiency in AlN films was 5% at 600°C and 12% at 700°C. In addition, Wahl *et al.* [393] reported Na implanted AlN and annealing of implanted AlN at 600–900°C played an important role in the interstitial Na to the cation substitutional sites, although no p-type conductivity was observed.

AlN devices and applications

Due to AlN's excellent piezoelectric and dielectric properties, various AlN-based functional devices have been demonstrated, including micro-electromechanical systems (MEMS) [366, 394–397], energy harvesters [394], ultrasonic transducers [395] and resonators [398]. Figure 24a and b shows the schematic of the device cross-section and the image of AlN flexible energy harvester, respectively [395]. This device could generate electrical energy from human motion at a very low moving speed with a generated voltage of as high as 0.7 V (Fig. 24c), which can be used for flexible skin as wearable energy harvesters. AlN also has great potential for power devices due to AlN's large critical electric field of 12 MV cm^{-1} and thermal conductivity of 340 W m^{-1} K^{-1} [6]. Irokawa *et al.* [359] reported lateral Pt/AlN SBDs on undoped AlN single-crystal substrates (Fig. 24d) with a turn-on voltage of 2.6 V, a breakdown voltage of <50 V and an ideality factor of 12. The unintentionally doped AlN substrates showed n-type conductivity, possibly due to the unintentionally doped oxygen. The high ideality factor was attributed to defects and/or interfacial states at the metal/semiconductor interface. Kinoshita *et al.* [399] demonstrated vertical AlN SBDs on homo-epitaxially grown AlN layers (Fig. 24e) with a turn-on voltage of 2.2 V, a breakdown voltage of 550–770 V and an ideality factor of 8. The Si-doped AlN layer was grown by HVPE on the AlN substrate that was subsequently removed for ohmic contact formation. Fu *et al.* [362] demonstrated the first 1-kV class AlN SBD on low-cost sapphire substrates by MOCVD. As shown in Fig. 24f, the epitaxy structure consisted of an AlN buffer layer, a

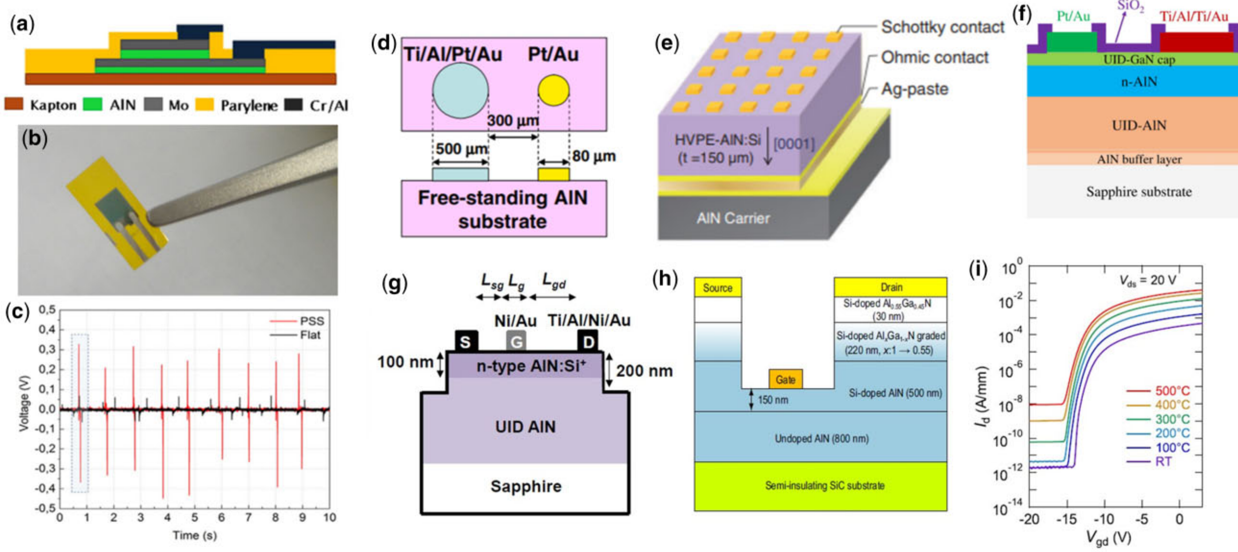

Figure 24: (**a**) Cross-section and (**b**) image of the flexible device for energy harvesting [395]. Reprinted with permission from Ref. [395]. Copyright 2016, Elsevier. (**c**) Generated off-state voltage for the flexible devices with a pre-stressed structure (PSS, red line) and a flat structure (black line) in folding/unfolding states [395]. Reprinted with permission from Ref. [395]. Copyright 2016, Elsevier. (**d**) Schematic of the lateral AlN SBDs on bulk AlN single-crystal substrate [359]. Reprinted with permission from Ref. [359]. Copyright 2012, IOP Science. (**e**) Schematic of AlN SBDs fabricated on an HVPE-AlN: Si substrate via substrate removal [399]. Reprinted with permission from Ref. [399]. Copyright 2015, IOP Science. (**f**) Schematic of fabricated AlN SBDs on sapphire by MOCVD [362]. Reprinted with permission from Ref. [362]. Copyright 2017, IEEE Xplore. (**g**) Schematic of AlN MESFETs by Si ion implantation [6]. Reprinted with permission from Ref. [6]. Copyright 2018, IOP Science. (**h**) Schematic and (**i**) temperature-dependent transfer characteristics of AlN MESFETs with epitaxially grown AlN channel and AlGaN contact layers [5]. Reprinted with permission from Ref. [5]. Copyright 2019, AIP Publishing.

Downloaded from https://academic.oup.com/ooms/article/2/1/itac004/6581087 by guest on 04 August 2022

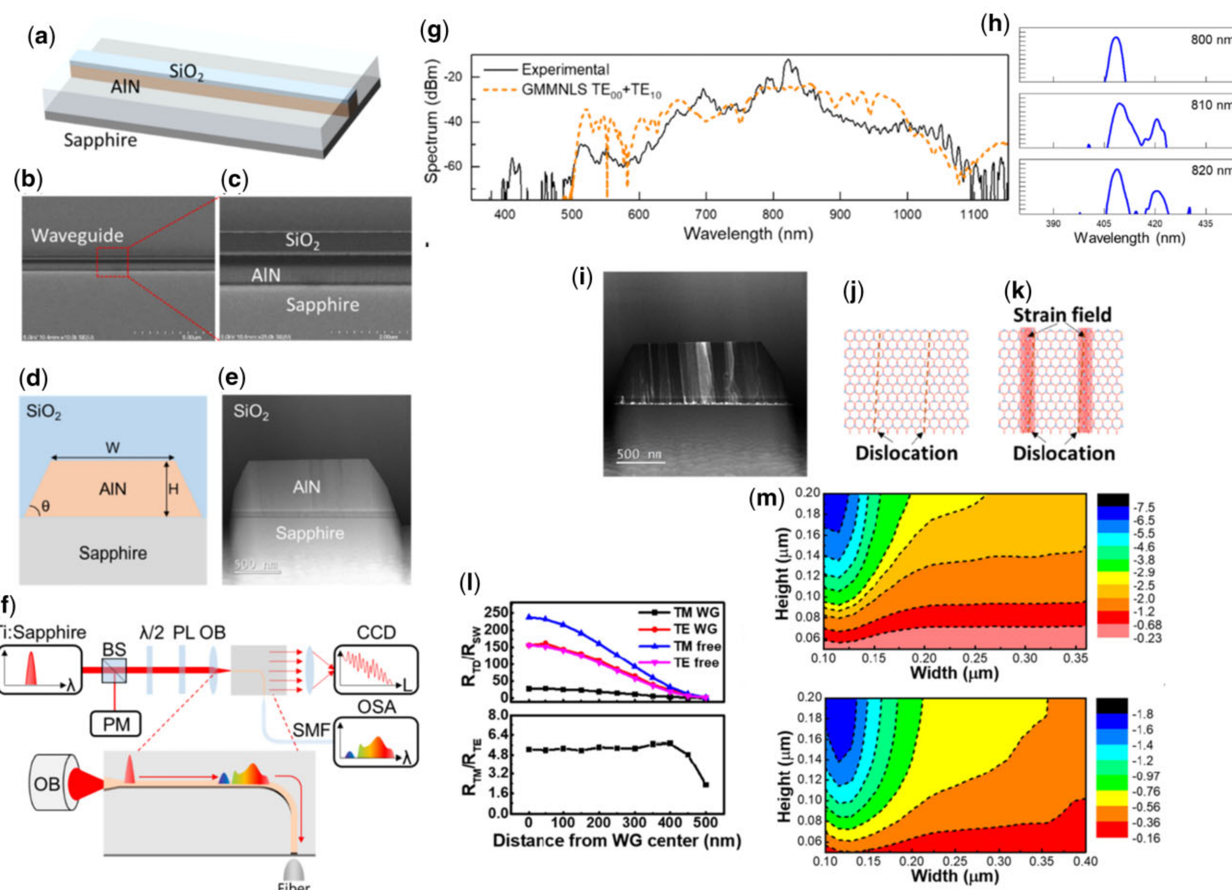

Figure 25: (a) Schematic of the AlN waveguide fabricated on sapphire. The coating and cladding layer is semitransparent for illustration purposes [401]. (b) and (c) SEM images of the AlN waveguides [401]. (d) Cross-sectional schematic of the AlN waveguide [401]. (e) TEM image of a typical AlN waveguide. (f) Testing setup for characterizing the AlN waveguide. BS, λ/2, PL, PM and OB are beam splitters, half-wavelength plates, polarizers, power meters and optical objective lenses, respectively [401]. (g) The experimental supercontinuum spectrum and the simulated spectrum for the AlN waveguide. (h) SHG signal near 400 nm at different pumping wavelengths [401]. Reprinted with permission from Ref. [401]. Copyright 2021, American Physical Society. (i) Cross-sectional TEM image of AlN waveguides [400]. (j) and (k) The dielectric equivalent of threading dislocation for scattering analysis [400]. (l) Threading dislocation scattered power versus sidewall non-ideality scattered power R_{TD}/R_{SW} and scattered power ratio between TM and TE mode R_{TM}/R_{TE} as a function of distance from waveguide center [400]. (m) The loss map for threading dislocation induced scattering loss for TE and TM modes [400].

1-μm-thick resistive UID AlN underlayer, a 300-nm Si-doped n-AlN layer and a 2-nm UID GaN capping layer. The AlN SBDs had a turn-on voltage of 1.2 V, an on/off ratio of $\sim 10^5$, an ideality factor of 5.5 and a record breakdown voltage of 1 kV. Recently, AlN MESFETs were demonstrated on implanted n-type AlN and epitaxially grown AlN with excellent high-temperature performance (Fig. 24g–i) [5, 6].

III-nitrides-based integrated resonators and photonic waveguides have enabled a wide variety of applications, including harmonic generations, comb generations, modulators and quantum emitters [400]. Due to its UWBG and good integration capability, III-nitrides have recently attracted growing attention for applications in UV-visible photonics. Chen *et al.* [401] demonstrated supercontinuum generation using dispersion engineered AlN waveguides with ultralow input power. The schematics and electron microscopy images of the AlN waveguide are shown in Fig. 25a–e and the testing setup is schematically shown in Fig. 25f. The main supercontinuum spectrum ranged from 490 nm to over 1100 nm, with a secondary SHG spectrum from 407 to 425 nm (Fig. 25g and h). Later, Chen *et al.* [400] also studied the threading dislocation-induced optical scattering loss inside AlN waveguides since AlN on sapphire is still highly defective (Fig. 25i). In the vicinity of threading dislocations, the abnormal atom arrangement (Fig. 25j) results in strain fields near its neighboring sites (Fig. 25k). The effects of single threading dislocation and threading dislocation array on the performance of AlN waveguides were comprehensively studied (Fig. 25l and m). It was found that threading dislocation can dramatically increase the scattering loss and crystallinity improvement of AlN materials is key to high-performance AlN waveguides. In addition, AlN waveguide geometry and light polarization also play in role in the scattering loss of AlN waveguides, where TM modes and multimode large core AlN waveguides are more susceptible to threading dislocations.

Single deep-level point defects or color centers in AlN are promising candidates for quantum sensing, quantum optics and quantum information processing due to atomic-scale SPE and optically active spin properties [402–405]. Xue *et al.* [404] first observed the SPEs from point defects in AlN films from visible to near-infrared regimes. AlN-on-sapphire platform is also enabling AlN-based PICs, with a wide variety of nonlinear optical effects such as electro-optic modulation, sum/difference frequency generation, parametric frequency conversion and frequency comb generation [405–407]. Lu *et al.* [408] reported an integrated scalable AlN-on-sapphire PIC platform (Fig. 26a and b) based on several pioneering works [409–411]. Quantum emitters

Downloaded from https://academic.oup.com/ooms/article/2/1/itac004/6581087 by guest on 04 August 2022

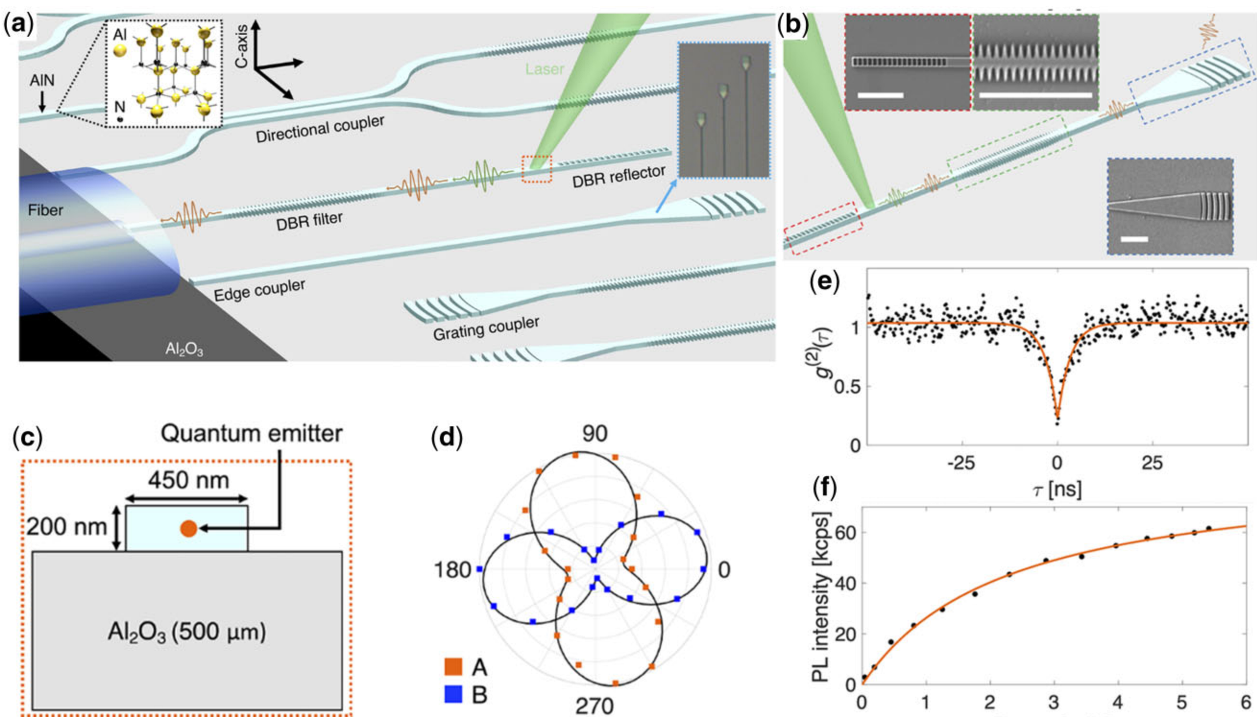

Figure 26: (a) Scalable AlN-on-sapphire PICs with integrated quantum emitters [408]. (b) AlN PIC with distributed Bragg reflectors as a filter (green) and a directional reflector (red), as well as a grating coupler (blue) for the dense population of read-out channels on a single chip. The insets are SEM images of the structures, with scale bars of 2 μm in each [408]. (c) Cross-section of the single-mode AlN waveguide on sapphire [408]. (d) Polar plots of PL as a function of linear excitation laser polarization [408]. (e) Autocorrelation measurement of the emitter via waveguide collection only, with $g^{(2)}(0) = 0.21 \pm 0.08$. (f) PL intensity saturation response of an emitter with waveguide collection [408]. Reprinted with permission from Ref. [408]. Copyright 2020, American Physical Society.

based on AlN point defects could be embedded within the AlN waveguide for integration (Fig. 26c) with their optical characterizations shown in Fig. 26d–f. These results indicate that the AlN point defect quantum emitters can be integrated with AlN waveguides using conventional AlN fabrication processes, demonstrating the potential of the AlN-on-sapphire platform for PICs.

SUMMARY AND FUTURE DIRECTIONS

With unique and remarkable properties, UWBG semiconductors are becoming a promising material platform for various devices and applications, including power electronics, photonics, high-frequency applications, MEMS and quantum computation. However, due to their immature status, significant research efforts are still required to understand the basic properties and to develop associate processing techniques for the UWBG materials. First, it is important to realize the large-scale and high-quality synthesis of UWBG single crystals and thin films. A deeper understanding of the growth mechanisms, such as grain size, crystal shape, orientation and defects, is required for effective control and engineering of UWBG material properties. Innovations in synthesis techniques are also critical to scaling up the production of high-purity UWBG crystals. Second, effective doping strategies are still lacking for UWBG materials, which greatly hinders the performance of UWBG devices. To date, it is still very challenging to achieve n-type doping in diamond, p-type doping in Ga_2O_3, p-type doping in AlN and both p-type and n-type doping in BN. The choice of proper dopants and the precise control of doping concentrations and positions should be a topic of comprehensive investigation for UWBG materials, where the possible contamination and damage to the materials should also be considered. Third, fundamental understanding and associated fabrication techniques of the UWBG heterostructures are crucial for the development of high-performance electronic devices. This research requires collective efforts on topics such as epitaxial growth, defects, interface states, band alignment and charge transfer process. The possible integration of UWBG materials with other electronic materials such as Si, GaN and 2D materials such as graphene, TMDs, can lead to new device concepts in power electronics, flexible electronics and high-frequency devices. Forth, benefiting from the UWBGs, UWBG materials are especially suitable for UV photonics applications, which will significantly extend the capabilities of the current III–V- and Si-integrated photonics from visible and IR to UV and DUV applications. Finally, UWBG materials are excellent candidates for emerging quantum applications. For example, diamond has been widely researched for quantum sensing and quantum computing applications, while single-photon emitters were developed on BN. With more advanced synthesis techniques, high-quality UWBG crystals with controllable defects can expedite the development of these areas. In summary, UWBG semiconductors represent a new class of functional materials that have remarkable material properties. With further research and innovations, the new understandings and new material processing techniques will enable high-performance devices for a wide range of applications in power electronics, UV photonics and quantum sensing and computing.

FUNDING

This research is supported as part of ULTRA, an Energy Frontier Research Center funded by the US Department of

Downloaded from https://academic.oup.com/ooms/article/2/1/itac004/6581087 by guest on 04 August 2022

Energy (DOE), Office of Science, Basic Energy Sciences (BES), under Award No. DE-SC0021230. This work is also partially supported by the grant from Army Research Office (ARO) PECASE Grant No. W911NF-19-1-0089 and the ARO DURIP Grant No. W911NF-19-1-0129 monitored by Dr. Michael Gerhold.

AUTHORS' CONTRIBUTIONS

M.X., K.F. and Y.Z. led the writing of diamond and h-BN. D.W., D.H.M. and H.F. led the writing of Ga_2O_3 and AlN. All authors read through the paper and made significant contributions.

CONFLICT OF INTEREST STATEMENT

The authors declare no conflicts of interest.

REFERENCES

1. Choi S, Graham S, Chowdhury S *et al.* A perspective on the electro-thermal co-design of ultra-wide bandgap lateral devices. *Appl Phys Lett* 2021;**119**:170501.
2. Chen J, Du X, Luo Q *et al.* A review of switching oscillations of wide bandgap semiconductor devices. *IEEE Trans Power Electron* 2020;**35**:13182–13199.
3. Morya AK, Gardener MC, Anvari B *et al.* Wide bandgap devices in AC electric drives: opportunities and challenges. *IEEE Trans Transport Electrif* 2019;**5**:3–20.
4. Angelone M, Verona C. Properties of diamond-based neutron detectors operated in harsh environments. *J Nucl Eng* 2021;**2**:422–470.
5. Hiroki M, Kumakura K. Ohmic contact to AlN:Si using graded AlGaN contact layer. *Appl Phys Lett* 2019;**115**:192104.
6. Okumura H, Suihkonen S, Lemettinen J *et al.* AlN metal–semiconductor field-effect transistors using Si-ion implantation. *Jap J Appl Phys* 2018;**57**.
7. Clark CD, Dean PJ, Harris PV *et al.* Intrinsic edge absorption in diamond. *Proc R Soc Lond Ser A Math Phys Sci* 1964;**277**: 312–329.
8. Saslow W, Bergstresser TK, Cohen ML. Band structure and optical properties of diamond. *Phys Rev Lett* 1966;**16**:354–356.
9. Suzuki M, Sakai T, Makino T *et al.* Electrical characterization of diamond PiN diodes for high voltage applications. *Phys Status Solidi (A) Appl Mater Sci* 2013;**210**:2035–2039.
10. Ueda K, Kawamoto K, Asano H. High-temperature and high-voltage characteristics of Cu/diamond Schottky diodes. *Diam Relat Mater* 2015;**57**:28–31.
11. Fujii S. High-frequency surface acoustic wave filter based on diamond thin film. *Phys Status Solidi (A) Appl Mater Sci* 2011; **208**:1072–1077.
12. Kania DR, Landstrass MI, Plano MA *et al.* Diamond radiation detectors. *Diam Relat Mater* 1993;**2**:1012–1019.
13. Kaneko JH, Tanaka T, Imai T *et al.* Radiation detector made of a diamond single crystal grown by a chemical vapor deposition method. *Nucl Instrum Methods Phys Res A* 2003;**505**: 187–190.
14. Wang W, Moses TM, Shigley JE. Physical and chemical features of a large coated natural diamond crystal. *Diam Relat Mater* 2009;**12**:330–335.
15. Tsao JY, Chowdhury S, Hollis MA *et al.* Ultrawide-bandgap semiconductors: research opportunities and challenges. *Adv Electron Mater* 2018;**4**:1600501.
16. Roy S, Zhang X, Puthirath AB *et al.* Structure, properties and applications of two-dimensional hexagonal boron nitride. *Adv Mater* 2021;**33**:2101589.
17. Aggarwal RL, Ramdas AK. Physical Properties of Diamond and Sapphire. CRC Press, 2019.
18. Telling RH, Pickard CJ, Payne MC *et al.* Theoretical strength and cleavage of diamond. *Phys Rev Lett* 2000;**84**:5160.
19. Luo X, Liu Z, Xu B *et al.* Compressive strength of diamond from first-principles calculation. *J Phys Chem C* 2010;**114**: 17851–17853.
20. Klein CA, Cardinale GF. Young's modulus and Poisson's ratio of CVD diamond. *Diam Relat Mater* 1993;**2**:918–923.
21. Bhagavantam S, Bhimasenachar J. Elastic constants of diamond. *Proc R Soc Lond Ser A Math Phys Sci* 1946;**187**:381–384.
22. Grimsditch MH, Ramdas AK. Brillouin scattering in diamond. *Phys Rev B* 1975;**11**:3139.
23. Wang SQ, Ye HQ Ab initio elastic constants for the lonsdaleite phases of C, Si and Ge. *J Phys Condens Matter* 2003;**15**: 5307.
24. Wei L, Kuo PK, Thomas RL *et al.* Thermal conductivity of isotopically modified single crystal diamond. *Phys Rev Lett* 1993; **70**:3764.
25. Bundy FP, Hall HT, Strong HM *et al.* Man-made diamonds. *Nature* 1955;**176**:51–55.
26. Sumiya H, Satoh S. High-pressure synthesis of high-purity diamond crystal. *Diam Relat Mater* 1996;**5**:1359–1365.
27. Kasu M. Diamond epitaxy: basics and applications. *Prog Cryst Growth Charact Mater* 2016;**62**:317–328.
28. Arnault J-C, Saada S, Ralchenko V. Chemical vapor deposition single-crystal diamond: a review. *Phys Status Solidi Rapid Res Lett* 2021;2100354.
29. Fang C, Jia X, Chen N *et al.* HPHT synthesis of N–H co-doped diamond single crystals. *J Cryst Growth* 2016;**436**:34–39.
30. Friel I, Clewes SL, Dhillon HK *et al.* Control of surface and bulk crystalline quality in single crystal diamond grown by chemical vapour deposition. *Diam Relat Mater* 2009;**18**: 808–815.
31. Kobashi K, Nishimura K, Kawate Y *et al.* Synthesis of diamonds by use of microwave plasma chemical-vapor deposition: morphology and growth of diamond films. *Phys Rev B* 1988;**38**:4067–4084.
32. Ashfold MNR, May PW, Rego CA *et al.* Thin film diamond by chemical vapour deposition methods. *Chem Soc Rev* 1994;**23**: 21–30.
33. Tallaire A, Kasu M, Ueda K *et al.* Origin of growth defects in CVD diamond epitaxial films. *Diam Relat Mater* 2008;**17**: 60–65.
34. Schreck M, Gsell S, Brescia R *et al.* Ion bombardment induced buried lateral growth: the key mechanism for the synthesis of single crystal diamond wafers. *Sci Rep* 2017;**7**:44462.
35. Mehmel L, Issaoui R, Brinza O *et al.* Dislocation density reduction using overgrowth on hole arrays made in heteroepitaxial diamond substrates. *Appl Phys Lett* 2021;**118**:061901.
36. Tallaire A, Mille V, Brinza O *et al.* Thick CVD diamond films grown on high-quality type IIa HPHT diamond substrates from New Diamond Technology. *Diam Relat Mater* 2017;**77**: 146–152.
37. Ohmagari S, Yamada H, Tsubouchi N *et al.* Schottky barrier diodes fabricated on diamond mosaic wafers: dislocation reduction to mitigate the effect of coalescence boundaries. *Appl Phys Lett* 2019;**114**:082104.
38. Yamada H, Chayahara A, Mokuno Y *et al.* 2-in. mosaic wafer made of a single-crystal diamond. *Appl Phys Lett* 2014;**104**: 102110.

Downloaded from https://academic.oup.com/ooms/article/2/1/itac004/6581087 by guest on 04 August 2022

39. Mandal S. Nucleation of diamond films on heterogeneous substrates: a review. *RSC Adv* 2021;**11**:10159–10182.
40. Williams OA, Douhéret O, Daenen M *et al*. Enhanced diamond nucleation on monodispersed nanocrystalline diamond. *Chem Phys Lett* 2007;**445**:255–258.
41. Hees J, Kriele A, Williams OA. Electrostatic self-assembly of diamond nanoparticles. *Chem Phys Lett* 2011;**509**:12–15.
42. Yoshikawa T, Zuerbig V, Gao F *et al*. Appropriate salt concentration of nanodiamond colloids for electrostatic self-assembly seeding of monosized individual diamond nanoparticles on silicon dioxide surfaces. *Langmuir* 2015;**31**: 5319–5325.
43. Yugo S, Kanai T, Kimura T *et al*. Generation of diamond nuclei by electric field in plasma chemical vapor deposition. *Appl Phys Lett* 1991;**58**:1036–1038.
44. Stoner BR, Ma GHM, Wolter SD *et al*. Characterization of bias-enhanced nucleation of diamond on silicon by invacuo surface analysis and transmission electron microscopy. *Phys Rev B* 1992;**45**:11067–11084.
45. Bade JP, Sahaida SR, Stoner BR *et al*. Highly oriented, textured diamond films on silicon via bias-enhanced nucleation and textured growth. *J Mater Res* 1993;**8**:1334–1340.
46. Tsugawa K, Ishihara M, Kim J *et al*. Nucleation enhancement of nanocrystalline diamond growth at low substrate temperatures by adamantane seeding. *J Phys Chem C* 2010;**114**: 3822–3824.
47. Tiwari RN, Chang L. Growth, microstructure, and field-emission properties of synthesized diamond film on adamantane-coated silicon substrate by microwave plasma chemical vapor deposition. *J Appl Phys* 2010;**107**:103305.
48. Tiwari RN, Tiwari JN, Chang L. The synthesis of diamond films on adamantane-coated Si substrate at low temperature. *Chem Eng J* 2010;**158**:641–645.
49. Mandal S, Thomas ELH, Jenny TA *et al*. Chemical nucleation of diamond films. *ACS Appl Mater Interfaces* 2016;**8**: 26220–26225.
50. Fujimori N, Imai T, Doi A. Characterization of conducting diamond films. *Vacuum* 1986;**36**:99–102.
51. Yugo S, Kimura T, Kanai H *et al*. Growth of diamond films by plasma CVD. *MRS Online Proc Library* 1987;**97**:327–332.
52. Chang CP, Flamm DL, Ibbotson DE *et al*. Diamond crystal growth by plasma chemical vapor deposition. *J Appl Phys* 1988;**63**:1744–1748.
53. Morrish AA, Pehrsson PE. Effects of surface pretreatments on nucleation and growth of diamond films on a variety of substrates. *Appl Phys Lett* 1991;**59**:417–419.
54. Ravi KV, Koch CA. Nucleation enhancement of diamond synthesized by combustion flame techniques. *Appl Phys Lett* 1990;**57**:348–350.
55. Singh J. Nucleation and growth mechanism of diamond during hot-filament chemical vapour deposition. *J Mater Sci* 1994;**29**:2761–2766.
56. Kobayashi K, Nakano T, Mutsukura N *et al*. Characterization of diamond nucleation on Fe/Si substrate by hot-filament chemical vapor deposition. *Vacuum* 1993;**44**:1–5.
57. Dai Z, Bednarski-Meinke C, Golding B Heteroepitaxial diamond film growth: the a-plane sapphire–iridium system. *Diam Relat Mater* 2004;**13**:552–556.
58. Morelli DT, Hartnett TM, Robinson CJ. Phonon-defect scattering in high thermal conductivity diamond films. *Appl Phys Lett* 1991;**59**:2112–2114.
59. Koidl P, Klages CP. Optical applications of polycrystalline diamond. *Diam Relat Mater* 1992;**1**:1065–1074.
60. Szirmai P, Fabian G, Koltai J *et al*. Observation of conduction electron spin resonance in boron-doped diamond. *Phys Rev B* 2013;**87**:195132.
61. Geis MW, Wade TC, Wuorio CH *et al*. Progress toward diamond power field-effect transistors. *Phys Status Solidi (A) Appl Mater Sci* 2018;**215**:1800681.
62. Crawford KG, Maini I, Macdonald DA *et al*. Surface transfer doping of diamond: a review. *Prog Surf Sci* 2021;**96**:100613.
63. Ferrari AC, Robertson J. Raman spectroscopy of amorphous, nanostructured, diamond-like carbon, and nanodiamond. *Phil Trans R Soc Lond Ser A Math Phys Eng Sci* 2004;**362**: 2477–2512.
64. Prawer S, Nemanich RJ. Raman spectroscopy of diamond and doped diamond. *Phil Trans R Soc Lond Ser A Math Phys Eng Sci* 2004;**362**:2537–2565.
65. Ferrari AC. Determination of bonding in diamond-like carbon by Raman spectroscopy. *Diam Relat Mater* 2002;**11**: 1053–1061.
66. Solin SA, Ramdas AK. Raman spectrum of diamond. *Phys Rev B* 1970;**1**:1687–1698.
67. Shroder RE, Nemanich RJ, Glass JT. Analysis of the composite structures in diamond thin films by Raman spectroscopy. *Phys Rev B* 1990;**41**:3738–3745.
68. Knight DS, White WB. Characterization of diamond films by Raman spectroscopy. *J Mater Res* 2011;**4**:385–393.
69. Volpe P-N, Muret P, Pernot J *et al*. Extreme dielectric strength in boron doped homoepitaxial diamond. *Appl Phys Lett* 2010; **97**:223501.
70. Traoré A, Muret P, Fiori A *et al*. Zr/oxidized diamond interface for high power Schottky diodes. *Appl Phys Lett* 2014;**104**: 052105.
71. Umezawa H, Nagase M, Kato Y *et al*. High temperature application of diamond power device. *Diam Relat Mater* 2012;**24**: 201–205.
72. Kumaresan R, Umezawa H, Shikata S. Vertical structure Schottky barrier diode fabrication using insulating diamond substrate. *Diam Relat Mater* 2010;**19**:1324–1329.
73. Bormashov VS, Terentiev SA, Buga SG *et al*. Thin large area vertical Schottky barrier diamond diodes with low on-resistance made by ion-beam assisted lift-off technique. *Diam Relat Mater* 2017;**75**:78–84.
74. Makino T, Kato H, Tokuda N *et al*. Diamond Schottky-pn diode without trade-off relationship between on-resistance and blocking voltage. *Phys Status Solidi (A)* 2010;**207**: 2105–2109.
75. Brezeanu M, Rashid SJ, Amaratunga GAJ *et al*. On-state behaviour of diamond M-i-P structures. In: 2006 International Semiconductor Conference, 2006. IEEE, Sinaia, Romania. pp. 311–314. https://doi.org/10.1109/SMICND.2006.284006.
76. Rashid SJ, Tajani A, Twitchen DJ *et al*. Numerical parameterization of chemical-vapor-deposited (CVD) single-crystal diamond for device simulation and analysis. *IEEE Trans Electron Dev* 2008;**55**:2744–2756.
77. Suzuki M. High voltage diamond pin diodes: feasibility study on ultimate properties of diamond toward ultimate power devices. *Oyo Buturi* 2016;**85**:218–222.
78. Umezawa H. Recent advances in diamond power semiconductor devices. *Mater Sci Semiconduct Process* 2018;**78**:147–156.
79. Umezawa H, Matsumoto T, Shikata S-i. Diamond metal–semiconductor field-effect transistor with breakdown voltage over 1.5 kV. *IEEE Electron Dev Lett* 2014;**35**:1112–1114.
80. Iwasaki T, Hoshino Y, Tsuzuki K *et al*. High-temperature operation of diamond junction field-effect transistors with lateral p-n junctions. *IEEE Electron Dev Lett* 2013;**34**:1175–1177.

Downloaded from https://academic.oup.com/ooms/article/2/1/itac004/6581087 by guest on 04 August 2022

81. Iwasaki T, Kato H, Makino T *et al*. High-temperature bipolar-mode operation of normally-off diamond JFET. *IEEE J Electron Dev Soc* 2017;**5**:95–99.
82. Hirama K, Sato H, Harada Y *et al*. Diamond field-effect transistors with 1.3 A/mm drain current density by Al_2O_3 passivation layer. *Jap J Appl Phys* 2012;**51**:090112.
83. Kitabayashi Y, Kudo T, Tsuboi H *et al*. Normally-off C–H diamond MOSFETs with partial C–O channel achieving 2-kV breakdown voltage. *IEEE Electron Dev Lett* 2017;**38**:363–366.
84. Kawarada H, Yamada T, Xu D *et al*. Durability-enhanced two-dimensional hole gas of C–H diamond surface for complementary power inverter applications. *Sci Rep* 2017;**7**:42368.
85. Pham T, Pernot J, Perez G *et al*. Deep-depletion mode boron-doped monocrystalline diamond metal oxide semiconductor field effect transistor. *IEEE Electron Dev Lett* 2017;**38**:1571–1574.
86. Prins JF Bipolar transistor action in ion implanted diamond. *Appl Phys Lett* 1982;**41**:950–952.
87. Davies G, Hamer MF, Price WC. Optical studies of the 1.945 eV vibronic band in diamond. *Proc R Soc Lond A Math Phys Sci* 1976;**348**:285–298.
88. Doherty MW, Manson NB, Delaney P *et al*. The nitrogen-vacancy colour centre in diamond. *Phys Rep* 2013;**528**:1–45.
89. Gruber A, Dräbenstedt A, Tietz C *et al*. Scanning confocal optical microscopy and magnetic resonance on single defect centers. *Science* 1997;**276**:2012–2014.
90. Shishir D, Saha K. Nitrogen vacancy centre-based diamond microscope for investigating quantum materials. *Bull Mater Sci* 2021;**44**:276.
91. Rondin L, Tetienne JP, Hingant T *et al*. Magnetometry with nitrogen-vacancy defects in diamond. *Rep Prog Phys* 2014;**77**:056503.
92. Balasubramanian G, Chan IY, Kolesov R *et al*. Nanoscale imaging magnetometry with diamond spins under ambient conditions. *Nature* 2008;**455**:648–651.
93. Zhao N, Hu J-L, Ho S-W *et al*. Atomic-scale magnetometry of distant nuclear spin clusters via nitrogen-vacancy spin in diamond. *Nat Nanotechnol* 2011;**6**:242–246.
94. McGuinness LP, Yan Y, Stacey A *et al*. Quantum measurement and orientation tracking of fluorescent nanodiamonds inside living cells. *Nat Nanotechnol* 2011;**6**:358–363.
95. Dolde F, Fedder H, Doherty MW *et al*. Electric-field sensing using single diamond spins. *Nat Phys* 2011;**7**:459–463.
96. Hall LT, Cole JH, Hill CD *et al*. Sensing of fluctuating nanoscale magnetic fields using nitrogen-vacancy centers in diamond. *Phys Rev Lett* 2009;**103**:220802.
97. Cole JH, Hollenberg LCL. Scanning quantum decoherence microscopy. *Nanotechnology* 2009;**20**:495401.
98. Loubser JHN, van Wyk JA. Electron spin resonance in the study of diamond. *Rep Prog Phys* 1978;**41**:1201–1248.
99. Mita Y. Change of absorption spectra in type-Ib diamond with heavy neutron irradiation. *Phys Rev B* 1996;**53**:11360–11364.
100. Subedi SD, Fedorov VV, Peppers J *et al*. Laser spectroscopic characterization of negatively charged nitrogen-vacancy (NV^-) centers in diamond. *Opt Mater Exp* 2019;**9**:2076–2087.
101. Jarmola A, Berzins A, Smits J *et al*. Longitudinal spin-relaxation in nitrogen-vacancy centers in electron irradiated diamond. *Appl Phys Lett* 2015;**107**:242403.
102. Kollarics S, Simon F, Bojtor A *et al*. Ultrahigh nitrogen-vacancy center concentration in diamond. *Carbon* 2022;**188**:393–400.
103. Pezzagna S, Meijer J Quantum computer based on color centers in diamond. *Appl Phys Rev* 2021;**8**:011308.
104. Jelezko F, Wrachtrup J. Read-out of single spins by optical spectroscopy. *J Phys Condens Matter* 2004;**16**:R1089–R1104.
105. Jelezko F, Gaebel T, Popa I *et al*. Observation of coherent oscillations in a single electron spin. *Phys Rev Lett* 2004;**92**:076401.
106. Maurer PC, Kucsko G, Latta C *et al*. Room-temperature quantum bit memory exceeding one second. *Science* 2012;**336**:1283–1286.
107. Balasubramanian G, Neumann P, Twitchen D *et al*. Ultralong spin coherence time in isotopically engineered diamond. *Nat Mater* 2009;**8**:383–387.
108. Ruf M, Wan NH, Choi H *et al*. Quantum networks based on color centers in diamond. *J Appl Phys* 2021;**130**:070901.
109. Bradley CE, Randall J, Abobeih MH *et al*. A ten-qubit solid-state spin register with quantum memory up to one minute. *Phys Rev X* 2019;**9**:031045.
110. Pompili M, Hermans SLN, Baier S *et al*. Realization of a multinode quantum network of remote solid-state qubits. *Science* 2021;**372**:259–264.
111. Pearton SJ, Yang J, Cary PH *et al*. A review of Ga_2O_3 materials, processing, and devices. *Appl Phys Rev* 2018;**5**:011301.
112. Guo D, Guo Q, Chen Z *et al*. Review of Ga_2O_3-based optoelectronic devices. *Mater Today Phys* 2019;**11**:100157.
113. Chen X, Ren F, Gu S *et al*. Review of gallium-oxide-based solar-blind ultraviolet photodetectors. *Photon Res* 2019;**7**:381.
114. McCluskey MD. Point defects in Ga_2O_3. *J Appl Phys* 2020;**127**:101101.
115. Johan H, Svensson G, Albertsson J A reinvestigation of β-gallium oxide. *Acta Crystallogr C* 1996;**52**:1336–1338.
116. Varley JB, Weber JR, Janotti A *et al*. Oxygen vacancies and donor impurities in β-Ga_2O_3. *Appl Phys Lett* 2010;**97**:142106.
117. Zhou H, Maize K, Noh J *et al*. Thermodynamic studies of beta-Ga_2O_3 nanomembrane field-effect transistors on a sapphire substrate. *ACS Omega* 2017;**2**:7723–7729.
118. Ahn S, Ren F, Kim J *et al*. Effect of front and back gates on β-Ga_2O_3 nano-belt field-effect transistors. *Appl Phys Lett* 2016;**109**:013504.
119. Zhou H, Maize K, Qiu G *et al*. β-Ga_2O_3 on insulator field-effect transistors with drain currents exceeding 1.5 A/mm and their self-heating effect. *Appl Phys Lett* 2017;**111**:092102.
120. Yan Q, Gong H, Zhang J *et al*. β-Ga_2O_3 hetero-junction barrier Schottky diode with reverse leakage current modulation and BV^2/Ron,sp value of 0.93 GW/cm^2. *Appl Phys Lett* 2021;**118**:122102.
121. Lee J, Kim H, Gautam L *et al*. Study of phase transition in MOCVD grown Ga_2O_3 from κ to β phase by ex situ and in situ annealing. *Photonics* 2021;**8**:8010017.
122. Zhang Y, Mauze A, Speck JS. Anisotropic etching of β-Ga_2O_3 using hot phosphoric acid. *Appl Phys Lett* 2019;**115**:013501.
123. Yadav MK, Mondal A, Sharma SK *et al*. Substrate orientation dependent current transport mechanisms in β-Ga_2O_3/Si based Schottky barrier diodes. *J Vac Sci Technol A* 2021;**39**:033203.
124. Guo Z, Verma A, Wu X *et al*. Anisotropic thermal conductivity in single crystal β-gallium oxide. *Appl Phys Lett* 2015;**106**:111909.
125. Fu H, Chen H, Huang X *et al*. A comparative study on the electrical properties of vertical (-201) and (010) β-Ga_2O_3 schottky barrier diodes on EFG single-crystal substrates. *IEEE Trans Electron Dev* 2018;**65**:3507–3513.
126. Li W, Nomoto K, Hu Z *et al*. Fin-channel orientation dependence of forward conduction in kV-class Ga_2O_3 trench Schottky barrier diodes. *Appl Phys Exp* 2019;**12**:061007.

Downloaded from https://academic.oup.com/ooms/article/2/1/itac004/6581087 by guest on 04 August 2022

127. Zhang Y, Mauze A, Alema F *et al*. Near unity ideality factor for sidewall Schottky contacts on un-intentionally doped β-Ga_2O_3. *Appl Phys Exp* 2019;**12**:044005.
128. Zhang Y, Alema F, Mauze A *et al*. MOCVD grown epitaxial β-Ga_2O_3 thin film with an electron mobility of 176 cm^2/Vs at room temperature. *APL Mater* 2019;**7**:022506.
129. Mu S, Peelaers H, Zhang Y *et al*. Orientation-dependent band offsets between $(AlxGa1-x)_2O_3$ and Ga_2O_3. *Appl Phys Lett* 2020;**117**:252104.
130. Bhuiyan AFMAU, Feng Z, Huang H-L *et al*. Band offsets at metalorganic chemical vapor deposited β-$(AlxGa1-x)_2O_3$/β-Ga_2O_3 interfaces—crystalline orientation dependence. *J Vac Sci Technol A* 2021;**39**:063207.
131. Hadamek T, Posadas AB, Al-Quaiti F *et al*. β-Ga_2O_3 on Si (001) grown by plasma-assisted MBE with γ-Al_2O_3 (111) buffer layer: structural characterization. *AIP Adv* 2021;**11**:045209.
132. Montes J, Kopas C, Chen H *et al*. Deep level transient spectroscopy investigation of ultra-wide bandgap (-201) and (001) β-Ga_2O_3. *J Appl Phys* 2020;**128**:205701.
133. Chen H, Fu H, Huang X *et al*. Characterizations of the nonlinear optical properties for (010) and (201) beta-phase gallium oxide. *Opt Exp* 2018;**26**:3938–3946.
134. Galazka Z, Uecker R, Irmscher K *et al*. Czochralski growth and characterization of β-Ga_2O_3 single crystals. *Cryst Res Technol* 2010;**45**:1229–1236.
135. Matthew DM. Point defects in Ga_2O_3. *J Appl Phys* 2020;**127**: 121101.
136. Jiaye Z, Shi J, Qi D-C *et al*. Recent progress on the electronic structure, defect, and doping properties of Ga_2O_3. *APL Mater* 2020;**8**:020906.
137. Hoshikawa K, Ohba E, Kobayashi T *et al*. Growth of β-Ga_2O_3 single crystals using vertical Bridgman method in ambient air. *J Cryst Growth* 2016;**447**:36–41.
138. Encarnación GV, Shimamura K, Yoshikawa Y *et al*. Large-size β-Ga_2O_3 single crystals and wafers. *J Cryst Growth* 2004; **270**:420–426.
139. Zbigniew G, Ganschow S, Seyidov P *et al*. Two inch diameter, highly conducting bulk β-Ga_2O_3 single crystals grown by the Czochralski method. *Appl Phys Lett* 2022;**120**:152101.
140. Oishi T, Koga Y, Harada K *et al*. High-mobility β-Ga_2O_3 (-201) single crystals grown by edge-defined film-fed growth method and their Schottky barrier diodes with Ni contact. *Appl Phys Exp* 2015;**8**:031101.
141. Yamaguchi H, Kuramata A. Stacking faults in beta-Ga_2O_3 crystals observed by X-ray topography. *J Appl Crystallogr* 2018;**51**:1372–1377.
142. Nakai K, Nagai T, Noami K *et al*. Characterization of defects in β-Ga_2O_3 single crystals. *Jap J Appl Phys* 2015;**54**:051103.
143. Hanada K, Moribayashi T, Koshi K *et al*. Origins of etch pits in β-Ga_2O_3 (010) single crystals. *Jap J Appl Phys* 2016;**55**:1202BG.
144. Kasu M, Oshima T, Hanada K *et al*. Crystal defects observed by the etch-pit method and their effects on Schottky-barrier-diode characteristics on (-201) β-Ga_2O_3. *Jap J Appl Phys* 2017;**56**: 091101.
145. Yuan Y, Hao W, Mu W *et al*. Toward emerging gallium oxide semiconductors: a roadmap. *Fundam Res* 2021;**11**.
146. Fu B, He G, Mu W *et al*. Laser damage mechanism and in situ observation of stacking fault relaxation in a β-Ga_2O_3 single crystal by the EFG method. *CrystEngComm* 2021;**23**: 3724–3730.
147. Alema F, Zhang Y, Osinsky A *et al*. Low 10^{14} cm^{-3} free carrier concentration in epitaxial β-Ga_2O_3 grown by MOCVD. *APL Mater* 2020;**8**:021110.
148. Alema F, Zhang Y, Mauze A *et al*. H_2O vapor assisted growth of β-Ga_2O_3 by MOCVD. *AIP Adv* 2020;**10**:085002.
149. Tadjer MJ, Alema F, Osinsky A *et al*. Characterization of β-Ga_2O_3 homoepitaxial films and MOSFETs grown by MOCVD at high growth rates. *J Phys D Appl Phys* 2021;**54**:034005.
150. Bhattacharyya A, Ranga P, Roy S *et al*. Low temperature homoepitaxy of (010) β-Ga_2O_3 by metalorganic vapor phase epitaxy: expanding the growth window. *Appl Phys Lett* 2020; **117**:142102.
151. Feng Z, Anhar Uddin Bhuiyan AFM, Karim MR *et al*. MOCVD homoepitaxy of Si-doped (010) β-Ga_2O_3 thin films with superior transport properties. *Appl Phys Lett* 2019;**114**:250601.
152. Alema F, Zhang Y, Osinsky A *et al*. Low temperature electron mobility exceeding 10^4 cm^2/Vs in MOCVD grown β-Ga_2O_3. *APL Mater* 2019;**7**:121110.
153. Seryogin G, Alema F, Valente N *et al*. MOCVD growth of high purity Ga_2O_3 epitaxial films using trimethylgallium precursor. *Appl Phys Lett* 2020;**117**:262101.
154. Alema F, Hertog B, Osinsky A *et al*. Fast growth rate of epitaxial β-Ga_2O_3 by close coupled showerhead MOCVD. *J Cryst Growth* 2017;**475**:77–82.
155. Mazzolini P, Falkenstein A, Wouters C *et al*. Substrate-orientation dependence of β-Ga_2O_3 (100), (010), (001), and (-201) homoepitaxy by indium-mediated metal-exchange catalyzed molecular beam epitaxy (MEXCAT-MBE). *APL Mater* 2020;**8**:011107.
156. Itoh T, Mauze A, Zhang Y *et al*. Epitaxial growth of β-Ga_2O_3 on (110) substrate by plasma-assisted molecular beam epitaxy. *Appl Phys Lett* 2020;**117**:152105.
157. Wong MH, Goto K, Murakami H *et al*. Current aperture vertical β-Ga_2O_3 MOSFETs fabricated by N- and Si-ion implantation doping. *IEEE Electron Dev Lett* 2019;**40**:431–434.
158. Wong MH, Higashiwaki M. Vertical β-Ga_2O_3 power transistors: a review. *IEEE Trans Electron Dev* 2020;**67**:3925–3937.
159. Pozina G, Hsu C-W, Abrikossova N *et al*. Doping of β-Ga_2O_3 layers by Zn using halide vapor-phase epitaxy process. *Phys Status Solidi (A) Appl Mater Sci* 2021;**218**:2100486.
160. Higashiwaki M, Sasaki K, Kuramata A *et al*. Development of gallium oxide power devices. *Phys Status Solidi (A) Appl Mater Sci* 2014;**211**:21–26.
161. Sdoeung S, Sasaki K, Masuya S *et al*. Stacking faults: origin of leakage current in halide vapor phase epitaxial (001) β-Ga_2O_3 Schottky barrier diodes. *Appl Phys Lett* 2021;**118**:172106.
162. Sdoeung S, Sasaki K, Masuya S *et al*. Polycrystalline defects—origin of leakage current—in halide vapor phase epitaxial (001) β-Ga_2O_3 Schottky barrier diodes identified via ultrahigh sensitive emission microscopy and synchrotron X-ray topography. *Appl Phys Exp* 2021;**14**:036502.
163. Nickel NH, Geilert K. Hydrogen density-of-states distribution in β-Ga_2O_3. *J Appl Phys* 2021;**129**:195704.
164. Shen H, Baskaran K, Yin Y *et al*. Effect of thickness on the performance of solar blind photodetectors fabricated using PLD grown β-Ga_2O_3 thin films. *J Alloys Compd* 2020;**822**: 153419.
165. Khartsev S, Nordell N, Hammar M *et al*. High-quality Si-doped β-Ga_2O_3 films on sapphire fabricated by pulsed laser deposition. *Phys Status Solidi (B) Basic Res* 2020;**258**:2000362.
166. Leedy KD, Chabak KD, Vasilyev V *et al*. Highly conductive homoepitaxial Si-doped Ga_2O_3 films on (010) β-Ga_2O_3 by pulsed laser deposition. *ApplPhys Lett* 2017;**111**:012103.
167. Saleh M, Varley JB, Jesenovec J *et al*. Degenerate doping in β-Ga_2O_3 single crystals through Hf-doping. *Semicond Sci Technol* 2020;**35**:04LT01.

Downloaded from https://academic.oup.com/ooms/article/2/1/itac004/6581087 by guest on 04 August 2022

168. Siah SC, Brandt RE, Lim K *et al*. Dopant activation in Sn-doped Ga_2O_3 investigated by X-ray absorption spectroscopy. *Appl Phys Lett* 2015;**107**:252103.
169. Zhou W, Xia C, Sai Q *et al*. Controlling n-type conductivity of β-Ga_2O_3 by Nb doping. *Appl Phys Lett* 2017;**111**:242103.
170. Ahmadi E, Koksaldi OS, Kaun SW *et al*. Ge doping of β-Ga_2O_3 films grown by plasma-assisted molecular beam epitaxy. *Appl Phys Exp* 2017;**10**:041102.
171. Víllora EG, Shimamura K, Yoshikawa Y *et al*. Electrical conductivity and carrier concentration control in β-Ga_2O_3 by Si doping. *Appl Phys Lett* 2008;**92**:202120.
172. Ranga P, Bhattacharyya A, Chmielewski A *et al*. Delta-doped β-Ga_2O_3 films with narrow FWHM grown by metalorganic vapor-phase epitaxy. *Appl Phys Lett* 2020;**117**:172105.
173. Gake T, Kumagai Y, Oba F. First-principles study of self-trapped holes and acceptor impurities in Ga_2O_3 polymorphs. *Phys Rev Mater* 2019;**3**:044603.
174. Jesenovec J, Varley J, Karcher SE *et al*. Electronic and optical properties of Zn-doped β-Ga_2O_3 Czochralski single crystals. *J Appl Phys* 2021;**129**:225702.
175. Tadjer MJ, Lyons JL, Nepal N *et al*. Editors' choice—review—theory and characterization of doping and defects in β-Ga_2O_3. *ECS J Solid State Sci Technol* 2019;**8**:Q3187–Q3194.
176. Peelaers H, Lyons JL, Varley JB *et al*. Deep acceptors and their diffusion in Ga_2O_3. *APL Mater* 2019;**7**:022519.
177. Feng Z, Bhuiyan AFMAU, Kalarickal NK *et al*. Mg acceptor doping in MOCVD (010) β-Ga_2O_3. *Appl Phys Lett* 2020;**117**: 222106.
178. Polyakov AY, Nikolaev VI, Tarelkin SA *et al*. Electrical properties and deep trap spectra in Ga_2O_3 films grown by halide vapor phase epitaxy on p-type diamond substrates. *J Appl Phys* 2021;**129**:185701.
179. Islam MM, Liedke MO, Winarski D *et al*. Chemical manipulation of hydrogen induced high p-type and n-type conductivity in Ga_2O_3. *Sci Rep* 2020;**10**:6134.
180. Lyons JL. A survey of acceptor dopants for β-Ga_2O_3. *Semicond Sci Technol* 2018;**33**:05LT02.
181. Lingaparthi R, Sasaki K, Thieu Q-T *et al*. Surface related tunneling leakage in β-Ga_2O_3 (001) vertical Schottky barrier diodes. *Appl Phys Exp* 2019;**12**:074008.
182. Farzana E, Alema F, Ho W Y *et al*. Vertical β-Ga_2O_3 field plate Schottky barrier diode from metal–organic chemical vapor deposition. *Appl Phys Lett* 2021;**118**:162109.
183. Oshima T, Hashiguchi A, Moribayashi T *et al*. Electrical properties of Schottky barrier diodes fabricated on (001) β-Ga_2O_3 substrates with crystal defects. *Jap J Appl Phys* 2017;**56**: 086501.
184. Hong Y-H, Zheng XF, He YL *et al*. The optimized interface characteristics of β-Ga_2O_3 Schottky barrier diode with low temperature annealing. *Appl Phys Lett* 2021;**119**:132103.
185. Lv Y, Liu H, Wang Y *et al*. Oxygen annealing impact on β-Ga_2O_3 MOSFETs: improved pinch-off characteristic and output power density. *Appl Phys Lett* 2020;**117**:133503.
186. Fabris E, Santi C D, Caria A *et al*. Trapping and detrapping mechanisms in β-Ga_2O_3 vertical FinFETs investigated by electro-optical measurements. *IEEE Trans Electron Dev* 2020; **67**:3954–3959.
187. Higashiwaki M, Sasaki K, Kamimura T *et al*. Depletion-mode Ga_2O_3 metal–oxide–semiconductor field-effect transistors on β-Ga_2O_3 (010) substrates and temperature dependence of their device characteristics. *Appl Phys Lett* 2013;**103**:123511.
188. Singh R, Lenka TR, Panda DK *et al*. The dawn of Ga_2O_3 HEMTs for high power electronics—a review. *Mater Sci Semiconduct Process* 2020;**119**:105216.
189. Zhang Y, Neal A, Xia Z *et al*. Demonstration of high mobility and quantum transport in modulation-doped β-(AlxGa1−x)$_2$O$_3$/Ga_2O_3 heterostructures. *Appl Phys Lett* 2018;**112**:173502.
190. Wong MH, Murakami H, Kumagai Y *et al*. Enhancement-mode current aperture vertical Ga_2O_3 MOSFETs. *IEEE Electron Dev Lett* 2019;**41**:296–299.
191. Chatterjee B, Li W, Nomoto K *et al*. Thermal design of multi-fin Ga_2O_3 vertical transistors. *Appl Phys Lett* 2021;**119**: 103502.
192. Masataka H, Sasaki K, Goto K *et al*. Ga_2O_3 Schottky barrier diodes with n-Ga_2O_3 drift layers grown by HVPE. In: 2015 73rd Annual Device Research Conference, 2015. IEEE, Columbus, OH, USA. pp. 29–30. https://doi.org/10.1109/DRC.2015.7175536.
193. Konishi K, Goto K, Murakami H *et al*. 1-kV vertical Ga_2O_3 field-plated Schottky barrier diodes. *Appl Phys Lett* 2017;**110**: 103506.
194. Sasaki K, Higashiwaki M, Kuramata A *et al*. Ga_2O_3 Schottky barrier diodes fabricated by using single-crystal β-Ga_2O_3 (010) substrates. *IEEE Electron Dev Lett* 2013;**34**:493–495.
195. Sasaki K, Wakimoto D, Thieu QT *et al*. First demonstration of Ga_2O_3 trench MOS-type Schottky barrier diodes. *IEEE Electron Dev Lett* 2017;**38**:783–785.
196. Yang J, Ahn S, Ren F *et al*. High reverse breakdown voltage Schottky rectifiers without edge termination on Ga_2O_3. *Appl Phys Lett* 2017;**110**:192101.
197. Yang J, Ahn S, Re F *et al*. High breakdown voltage (-201) β-Ga_2O_3 Schottky rectifiers. *IEEE Electron Dev Lett* 2017;**38**: 906–909.
198. Yang J, Ren F, Tadjer M *et al*. 2300 V reverse breakdown voltage Ga_2O_3 Schottky rectifiers. *ECS J Solid State Sci Technol* 2018;**7**:Q92–Q96.
199. Lv Y, Zhou X, Long S *et al*. Source-field-plated β-Ga_2O_3 MOSFET with record power figure of merit of 50.4 MW/cm^2. *IEEE Electron Dev Lett* 2018;**1**:83–86.
200. Green AJ, Chabak KD, Baldini M *et al*. β-Ga_2O_3 MOSFETs for radio frequency operation. *IEEE Electron Dev Lett* 2017;**38**: 790–793.
201. Jeng-Wei Y, Wu TR, Huang JJ *et al*. 75GHz Ga_2O_3/GaN single nanowire metal oxide–semiconductor field-effect transistors. In: 2010 IEEE Compound Semiconductor Integrated Circuit Symposium, 2010. IEEE, Monterey, CA, USA. pp. 1–4. https://doi.org/10.1109/CSICS.2010.5619673.
202. Ghosh K, Singisetti U. Electron mobility in monoclinic β-Ga_2O_3—effect of plasmon–phonon coupling, anisotropy, and confinement. *J Mater Res* 2017;**32**:4142–4152.
203. Oshima T, Kato Y, Kawano N *et al*. Carrier confinement observed at modulation-doped β-(AlxGa1−x)2O3/Ga_2O_3 heterojunction interface. *Appl Phys Exp* 2017;**10**:035701.
204. Wang D, Mudiyanselage DH, Fu H. Design space of delta-doped β -(AlxGa1−x)$_2$O$_3$/Ga_2O_3 high-electron mobility transistors. *IEEE Trans Electron Dev* 2022;**1**:69–74.
205. Cheng Z, Tanen N, Chang C *et al*. Significantly reduced thermal conductivity in β-(Al0.1Ga0.9)$_2$O$_3$/Ga_2O_3 superlattices. *Appl Phys Lett* 2019;**115**:092105.
206. Cheng Z, Mu F, You T *et al*. Thermal transport across ion-cut monocrystalline beta-Ga_2O_3 thin films and bonded beta-Ga_2O_3–SiC *interfaces*. *ACS Appl Mater Interfaces* 2020;**12**: 44943–44951.
207. Moser N, Liddy K, Islam A *et al*. Toward high voltage radio frequency devices in β-Ga_2O_3. *Appl Phys Lett* 2020;**117**:242101.
208. Kamimura T, Nakata Y, Higashiwaki M. Delay-time analysis in radio-frequency β-Ga_2O_3 field effect transistors. *Appl Phys Lett* 2020;**117**:253501.

Downloaded from https://academic.oup.com/ooms/article/2/1/itac004/6581087 by guest on 04 August 2022

209. Xia Z, Xue H, Joishi C *et al.* β-Ga_2O_3 delta-doped field-effect transistors with current gain cutoff frequency of 27 GHz. *IEEE Electron Dev Lett* 2019;**40**:1052–1055.
210. Watahiki T, Yuda Y, Furukawa A *et al.* Heterojunction p-Cu_2O/n-Ga_2O_3 diode with high breakdown voltage. *Appl Phys Lett* 2017;**111**:222104.
211. Guo XC, Hao NH, Guo DY *et al.* β-Ga_2O_3/p-Si heterojunction solar-blind ultraviolet photodetector with enhanced photoelectric responsivity. *J Alloys Compd* 2016;**660**:136–140.
212. Montes J, Yang C, Fu H *et al.* Demonstration of mechanically exfoliated β-Ga_2O_3/GaN p-n heterojunction. *Appl Phys Lett* 2019;**114**:162103.
213. Hao W, He Q, Zhou K *et al.* Low defect density and small I–V curve hysteresis in NiO/β-Ga_2O_3 pn diode with a high PFOM of 0.65 GW/cm^2. *Appl Phys Lett* 2021;**118**:043501.
214. Armaghani S, Khani S, Danaie M Design of all-optical graphene switches based on a Mach–Zehnder interferometer employing optical Kerr effect. *Superlattice Microstruct* 2019; **135**:106244.
215. Zhou J, Chen H, Fu K *et al.* Gallium oxide-based optical nonlinear effects and photonics devices. *J Mater Res* 2021;**36**: 4832–4845.
216. Kaur D, Kumar M. A Strategic review on gallium oxide based deep-ultraviolet photodetectors: recent progress and future prospects. *Adv Opt Mater* 2021;**9**:2002160.
217. Wang C, Zhang J, Xu S *et al.* Progresses in state-of-the-art technologies of Ga_2O_3 devices. *J Phys D Appl Phys* 2021;**54**: 243001.
218. Cooke J, Sensale-Rodriguez B, Ghadbeigi L. Methods for synthesizing β-Ga_2O_3 thin films beyond epitaxy. *J Phys Photon* 2021;**3**:032005.
219. Hou X, Zou Y, Ding M *et al.* Review of polymorphous Ga_2O_3 materials and their solar-blind photodetector applications. *J Phys D Appl Phys* 2020;**54**:043001.
220. Qian LX, Gu Z, Huang X *et al.* Comprehensively improved performance of beta-Ga_2O_3 solar-blind photodetector enabled by a homojunction with unique passivation mechanisms. *ACS Appl Mater Interfaces* 2021;**13**:40837–40846.
221. Wang F, Han Z, Tong L. Fabrication and characterization of β-Ga_2O_3 optical nanowires. *Phys E Low Dimension Syst Nanostruct* 2005;**30**:150–154.
222. Zhou J, Chen H, Fu H *et al.* Demonstration of low loss β-Ga_2O_3 optical waveguides in the UV–NIR spectra. *Appl Phys Lett* 2019;**115**:251108.
223. Oshima T, Okuno T, Arai N *et al.* Vertical solar-blind deep-ultraviolet Schottky photodetectors based on β-Ga_2O_3 substrates. *Appl Phys Exp* 2008;**1**:011202.
224. Singh Pratiyush A, Krishnamoorthy S, Solanke SV *et al.* High responsivity in molecular beam epitaxy grown β-Ga_2O_3 metal semiconductor metal solar blind deep-UV photodetector. *Appl Phys Lett* 2017;**110**:221107.
225. Guo D, Liu H, Li P *et al.* Zero-power-consumption solar-blind photodetector based on beta-Ga_2O_3/NSTO heterojunction. *ACS Appl Mater Interfaces* 2017;**9**:1619–1628.
226. Chen T, Zhang X, Ma Y *et al.* Self-powered and spectrally distinctive nanoporous Ga_2O_3/GaN epitaxial heterojunction UV photodetectors. *Adv Photon Res* 2021;**2**:2100049.
227. Ma Y, Tang W, Chen T *et al.* Effect of off-axis substrate angles on β-Ga_2O_3 thin films and solar-blind ultraviolet photodetectors grown on sapphire by MOCVD. *Mater Sci Semiconduct Process* 2021;**131**:105856.
228. Ma Y, Feng B, Zhang X *et al.* High-performance β-Ga_2O_3 solar-blind ultraviolet photodetectors epitaxially grown on (110) TiO_2 substrates by metalorganic chemical vapor deposition. *Vacuum* 2021;**191**:110402.
229. Ma YJ, Zhang X, Feng B *et al.* Mis-cut direction of substrate effect on the photoresponse characteristic of β-Ga_2O_3 film. *Vacuum* 2022;**198**:110886.
230. Wang Y, Li L, Wang H *et al.* An ultrahigh responsivity self-powered solar-blind photodetector based on a centimeter-sized beta-Ga_2O_3/polyaniline heterojunction. *Nanoscale* 2020;**12**:1406–1413.
231. Izyumskaya N, Demchenko DO, Das S *et al.* Recent development of boron nitride towards electronic applications. *Adv Electron Mater* 2017;**3**:1600485.
232. Paszkowicz W, Pelka JB, Knapp M *et al.* Lattice parameters and anisotropic thermal expansion of hexagonal boron nitride in the 10–297.5 K temperature range. *Appl Phys A Mater Sci Process* 2002;**75**:431–435.
233. Pauling L. The structure and properties of graphite and boron nitride. *Proc Natl Acad Sci USA* 1966;**56**:1646–1652.
234. Ji Y, Claderon B, Han Y *et al.* Chemical vapor deposition growth of large single-crystal mono-, bi-, tri-layer hexagonal boron nitride and their interlayer stacking. *ACS Nano* 2017; **11**:12057–12066.
235. Wickramaratne D, Weston L, van de Walle CG. Monolayer to bulk properties of hexagonal boron nitride. *J Phys Chem C* 2018;**122**:25524–25529.
236. Marom N, Bernstein J, Garel J *et al.* Stacking and registry effects in layered materials: the case of hexagonal boron nitride. *Phys Rev Lett* 2010;**105**:046801.
237. Pakdel A, Bando Y, Golberg D. Nano boron nitride flatland. *Chem Soc Rev* 2014;**43**:934–959.
238. Du AJ, Smith SC, Lu GQ. First-principle studies of electronic structure and C-doping effect in boron nitride nanoribbon. *Chem Phys Lett* 2007;**447**:181–186.
239. Song L, Ci L, Lu H *et al.* Large scale growth and characterization of atomic hexagonal boron nitride layers. *Nano Lett* 2010;**10**:3209–3215.
240. Gorbachev RV, Riaz I, Nair RR *et al.* Hunting for monolayer boron nitride: optical and Raman signatures. *Small* 2011;**7**: 465–468.
241. Zhi C, Bando Y, Tang C *et al.* Large-scale fabrication of boron nitride nanosheets and their utilization in polymeric composites with improved thermal and mechanical properties. *Adv Mater* 2009;**21**:2889–2893.
242. Lee G-H, Yu Y-J, Lee C *et al.* Electron tunneling through atomically flat and ultrathin hexagonal boron nitride. *Appl Phys Lett* 2011;**99**:243114.
243. Zunger A, Katzir A, Halperin A. Optical properties of hexagonal boron nitride. *Phys Rev B* 1976;**13**:5560–5573.
244. Liu L, Feng P, Shen X. Structural and electronic properties of h-BN. *Phys Rev B* 2003;**68**:104102.
245. Furthmuller J, Hafner J, Kresse G. Ab initio calculation of the structural and electronic properties of carbon and boron nitride using ultrasoft pseudopotentials. *Phys Rev B* 1994;**50**: 15606.
246. Topsakal M, Aktürk E, Ciraci S. First-principles study of two- and one-dimensional honeycomb structures of boron nitride. *Phys Rev B* 2009;**79**:115442.
247. Arnaud B, Lebègue S, Rabiller P *et al.* Huge excitonic effects in layered hexagonal boron nitride. *Phys Rev Lett* 2006;**96**: 026402.
248. Watanabe K, Taniguchi T, Kanda H. Direct-bandgap properties and evidence for ultraviolet lasing of hexagonal boron nitride single crystal. *Nat Mater* 2004;**3**:404–409.

Downloaded from https://academic.oup.com/ooms/article/2/1/itac004/6581087 by guest on 04 August 2022

249. Cassabois G, Valvin P, Gil B. Hexagonal boron nitride is an indirect bandgap semiconductor. *Nat Photon* 2016;**10**:262–266.
250. Ooi N, Rairkar A, Lindsley L *et al*. Electronic structure and bonding in hexagonal boron nitride. *J Phys Condens Matter* 2006;**18**:97–115.
251. Yamanaka A, Okada S. Energetics and electronic structure of h-BN nanoflakes. *Sci Rep* 2016;**6**:30653.
252. Laturia A, Van de Put ML, Vandenberghe WG. Dielectric properties of hexagonal boron nitride and transition metal dichalcogenides: from monolayer to bulk. *NPJ 2D Mater Appl* 2018;**2**:6.
253. Wang L, Pu Y, Soh AK *et al*. Layers dependent dielectric properties of two dimensional hexagonal boron nitride nanosheets. *AIP Adv* 2016;**6**:125126.
254. Hattori Y, Taniguchi T, Watanabe K *et al*. Layer-by-layer dielectric breakdown of hexagonal boron nitride. *ACS Nano* 2015;**9**:916–921.
255. Hattori Y, Taniguchi T, Watanabe K *et al*. Anisotropic dielectric breakdown strength of single crystal hexagonal boron nitride. *ACS Appl Mater Interfaces* 2016;**8**:27877–27884.
256. Kim KK, Hsu A, Jia X *et al*. Synthesis of monolayer hexagonal boron nitride on Cu foil using chemical vapor deposition. *Nano Lett* 2012;**12**:161–166.
257. Shi Y, Hamsen C, Jia X *et al*. Synthesis of few-layer hexagonal boron nitride thin film by chemical vapor deposition. *Nano Lett* 2010;**10**:4134–4139.
258. Gao R, Yin L, Wang C *et al*. High-yield synthesis of boron nitride nanosheets with strong ultraviolet. *J Phys Chem C* 2009; **113**:15160–15165.
259. Yu J, Qin L, Hao Y *et al*. Vertically aligned boron nitride nanosheets: chemical vapor synthesis, ultraviolet light emission, and superhydrophobicity. *ACS Nano* 2010;**4**:414–422.
260. Hua Li L, Chen Y, Cheng B-M *et al*. Photoluminescence of boron nitride nanosheets exfoliated by ball milling. *Appl Phys Lett* 2012;**100**:261108.
261. Pakdel A, Zhi C, Bando Y *et al*. Boron nitride nanosheet coatings with controllable water repellency. *ACS Nano* 2011;**5**: 6507–6515.
262. Tran TT, Bray K, Ford MJ *et al*. Quantum emission from hexagonal boron nitride monolayers. *Nat Nanotechnol* 2016;**11**: 37–41.
263. Duong HNM, Nguyen MAP, Kianinia MK *et al*. Effects of high-energy electron irradiation on quantum emitters in hexagonal boron nitride. *ACS Appl Mater Interfaces* 2018;**10**: 24886–24891.
264. Xu ZQ, Elbadawi C, Tran TT *et al*. Single photon emission from plasma treated 2D hexagonal boron nitride. *Nanoscale* 2018;**10**:7957–7965.
265. Bourrellier R, Meuret S, Tararan A *et al*. Bright UV single photon emission at point defects in h-BN. *Nano Lett* 2016;**16**: 4317–4321.
266. Kim CJ, Brown L, Graham MW *et al*. Stacking order dependent second harmonic generation and topological defects in h-BN bilayers. *Nano Lett* 2013;**13**:5660–5665.
267. Li Y, Rao Y, Mak KF *et al*. Probing symmetry properties of few-layer MoS_2 and h-BN by optical second-harmonic generation. *Nano Lett* 2013;**13**:3329–3333.
268. Kumbhakar P, Kole AK, Tiwary CS *et al*. Nonlinear optical properties and temperature-dependent UV–Vis absorption and photoluminescence emission in 2D hexagonal boron nitride nanosheets. *Adv Opt Mater* 2015;**3**:828–835.
269. Attaccalite C, Grüning M, Amara H *et al*. Two-photon absorption in two-dimensional materials: the case of hexagonal boron nitride. *Phys Rev B* 2018;**98**:165126.
270. Lindsay L, Broido DA. Enhanced thermal conductivity and isotope effect in single-layer hexagonal boron nitride. *Phys Rev B* 2011;**84**:155421.
271. Lin Y, Connell JW. Advances in 2D boron nitride nanostructures: nanosheets, nanoribbons, nanomeshes, and hybrids with graphene. *Nanoscale* 2012;**4**:6908–6939.
272. Peng Q, Ji W, De S. Mechanical properties of the hexagonal boron nitride monolayer: ab initio study. *Comput Mater Sci* 2012;**56**:11–17.
273. Boldrin L, Scarpa F, Chowdhury R *et al*. Effective mechanical properties of hexagonal boron nitride nanosheets. *Nanotechnol* 2011;**22**:505702.
274. Mirnezhad M, Ansari R, Rouhi H. Mechanical properties of multilayer boron nitride with different stacking orders. *Superlattice Microstruct* 2013;**53**:223–231.
275. Li C, Bando Y, Zhi C *et al*. Thickness-dependent bending modulus of hexagonal boron nitride nanosheets. *Nanotechnology* 2009;**20**:385707.
276. Novoselov KS, Geim AK, Morozov SV *et al*. Electric field effect in atomically thin carbon films. *Science* 2004;**306**:666–669.
277. Novoselov KS, Jiang D, Schedin F *et al*. Two-dimensional atomic crystals. *Proc Natl Acad Sci USA* 2005;**102**:10451–10453.
278. Meyer JC, Chuvilin A, Algara-Siller G *et al*. Selective sputtering and atomic resolution imaging of atomically thin boron nitride membranes. *Nano Lett* 2009;**9**:2683–2689.
279. Pacil̆ D, Meyer JC, Girit Ç *et al*. The two-dimensional phase of boron nitride: few-atomic-layer sheets and suspended membranes. *Appl Phys Lett* 2008;**92**:133107.
280. Jin C, Lin F, Suenaga K *et al*. Fabrication of a freestanding boron nitride single layer and its defect assignments. *Phys Rev Lett* 2009;**102**:195505.
281. Li LH, Chen Y, Behan G *et al*. Large-scale mechanical peeling of boron nitride nanosheets by low-energy ball milling. *J Mater Chem* 2011;**21**:11862–11866.
282. Deepika, Li LH, Glushenkov AM *et al*. High-efficient production of boron nitride nanosheets via an optimized ball milling process for lubrication in oil. *Sci Rep* 2014;**4**:7288.
283. Han WQ, Wu L, Zhu Y *et al*. Structure of chemically derived mono- and few-atomic-layer boron nitride sheets. *Appl Phys Lett* 2008;**93**:223103.
284. Warner JH, Rümmeli MH, Bachmatiuk A *et al*. Atomic resolution imaging and topography of boron nitride sheets produced by chemical exfoliation. *ACS Nano* 2010;**4**:1299–1304.
285. Li X, Hao X, Zhao M *et al*. Exfoliation of hexagonal boron nitride by molten hydroxides. *Adv Mater* 2013;**25**:2200–2204.
286. Kim KS, Zhao Y, Jang H *et al*. Large-scale pattern growth of graphene films for stretchable transparent electrodes. *Nature* 2009;**457**:706–710.
287. Xia J, Huang X, Liu L-Z *et al*. CVD synthesis of large-area, highly crystalline $MoSe_2$ atomic layers on diverse substrates and application to photodetectors. *Nanoscale* 2014;**6**: 8949–8955.
288. Wang S, Wang X, Warner JH. All chemical vapor deposition growth of MoS_2:h-BN vertical van der Waals heterostructures. *ACS Nano* 2015;**9**:5246–5254.
289. Paffett MT, Simonson RJ, Papin P *et al*. Borazine adsorption and decomposition at Pt(111) and Ru(001) surfaces. *Surf Sci* 1990;**232**:286–296.
290. Tay RY, Griep MH, Mallick G *et al*. Growth of large single-crystalline two-dimensional boron nitride hexagons on electropolished copper. *Nano Lett* 2014;**14**:839–846.
291. Auwärter W, Kreutz TJ, Greber T *et al*. XPD and STM investigation of hexagonal boron nitride on Ni(111). *Surf Sci* 1999; **429**:229–236.

Downloaded from https://academic.oup.com/ooms/article/2/1/itac004/6581087 by guest on 04 August 2022

292. Auwärter W, Suter HU, Sachdev H *et al*. Synthesis of one monolayer of hexagonal boron nitride on Ni(111) from B-Trichloroborazine $(ClBNH)_3$. *Chem Mater* 2004;**16**:343–345.
293. Auwärter W, Muntwiler M, Osterwalder J *et al*. Defect lines and two-domain structure of hexagonal boron nitride films on Ni(1 1 1). *Surf Sci* 2003;**545**:735–740.
294. Stehle Y, Meyer HM, Unocic RR *et al*. Synthesis of hexagonal boron nitride monolayer: control of nucleation and crystal morphology. *Chem Mater* 2015;**27**:8041–8047.
295. Lu G, Wu T, Yuan Q *et al*. Synthesis of large single-crystal hexagonal boron nitride grains on Cu–Ni alloy. *Nat Commun* 2015;**6**:6160.
296. Lee JS, Choi SH, Yun SJ *et al*. Wafer-scale single-crystal hexagonal boron nitride film via self-collimated grain formation. *Science* 2018;**362**:817–821.
297. Song X, Gao J, Nie Y *et al*. Chemical vapor deposition growth of large-scale hexagonal boron nitride with controllable orientation. *Nano Res* 2015;**8**:3164–3176.
298. Ismach A, Chou H, Ferrer DA *et al*. Toward the controlled synthesis of hexagonal boron nitride films. *ACS Nano* 2012;**6**:6378–6385.
299. Sajjad M, Ahmadi M, Guinel MJF *et al*. Large scale synthesis of single-crystal and polycrystalline boron nitride nanosheets. *J Mater Sci* 2013;**48**:2543–2549.
300. Sajjad M, Morell G, Feng P. Advance in novel boron nitride nanosheets to nanoelectronic device applications. *ACS Appl Mater Interfaces* 2013;**5**:5051–5056.
301. Olander J, Ottosson LM, Heszler P *et al*. Laser-assisted atomic layer deposition of boron nitride thin films. *Chem Vap Deposit* 2005;**11**:330–337.
302. Sutter P, Lahiri J, Zahl P *et al*. Scalable synthesis of uniform few-layer hexagonal boron nitride dielectric films. *Nano Lett* 2013;**13**:276–281.
303. Camilli L, Sutter E, Sutter P. Growth of two-dimensional materials on non-catalytic substrates: H-BN/Au (111). *2D Mater* 2014;**1**:025033.
304. Wang H, Zhang X, Liu H *et al*. Synthesis of large-sized single-crystal hexagonal boron nitride domains on nickel foils by ion beam sputtering deposition. *Adv Mater* 2015;**27**:8109–8115.
305. Wang H, Zhang X, Meng J *et al*. Controlled growth of few-layer hexagonal boron nitride on copper foils using ion beam sputtering deposition. *Small* 2015;**11**:1542–1547.
306. Ohta J, Fujioka H. Sputter synthesis of wafer-scale hexagonal boron nitride films via interface segregation. *APL Mater* 2017;**5**:076107.
307. Nakhaie S, Wofford JM, Schumann T *et al*. Synthesis of atomically thin hexagonal boron nitride films on nickel foils by molecular beam epitaxy. *Appl Phys Lett* 2015;**106**:213108.
308. Wofford JM, Nakhaie S, Krause T *et al*. A hybrid MBE-based growth method for large-area synthesis of stacked hexagonal boron nitride/graphene heterostructures. *Sci Rep* 2017;**7**:43644.
309. Sasama Y, Komatsu K, Moriyama S *et al*. High-mobility diamond field effect transistor with a monocrystalline h-BN gate dielectric. *APL Mater* 2018;**6**:111105.
310. Yang TH, Brown J, Fu K *et al*. AlGaN/GaN metal–insulator–semiconductor high electron mobility transistors (MISHEMTs) using plasma deposited BN as gate dielectric. *Appl Phys Lett* 2021;**118**:072102.
311. Guo N, Wei J, Jia Y *et al*. Fabrication of large area hexagonal boron nitride thin films for bendable capacitors. *Nano Res* 2013;**6**:602–610.
312. Dean CR, Young AF, Meric I *et al*. Boron nitride substrates for high-quality graphene electronics. *Nat Nanotechnol* 2010;**5**:722–726.
313. Yang W, Chen G, Shi Z *et al*. Epitaxial growth of single-domain graphene on hexagonal boron nitride. *Nat Mater* 2013;**12**:792–797.
314. Lee GH, Cui X, Kim YD *et al*. Highly stable, dual-gated MoS_2 transistors encapsulated by hexagonal boron nitride with gate-controllable contact, resistance, and threshold voltage. *ACS Nano* 2015;**9**:7019–7026.
315. Sajjad M, Jadwisienczak WM, Feng P. Nanoscale structure study of boron nitride nanosheets and development of a deep-UV photo-detector. *Nanoscale* 2014;**6**:4577–4582.
316. Li J, Majety S, Dahal R *et al*. Dielectric strength, optical absorption, and deep ultraviolet detectors of hexagonal boron nitride epilayers. *Appl Phys Lett* 2012;**101**:171112.
317. Aldalbahi A, Feng P. Development of 2-D boron nitride nanosheets UV photoconductive detectors. *IEEE Trans Electron Dev* 2015;**62**:1885–1890.
318. Tran TT, Zachreson C, Berhane AM *et al*. Quantum emission from defects in single-crystalline hexagonal boron nitride. *Phys Rev Appl* 2016;**5**:034005.
319. Gottscholl A, Kianinia M, Soltamov V *et al*. Initialization and read-out of intrinsic spin defects in a van der Waals crystal at room temperature. *Nat Mater* 2020;**19**:540–545.
320. Lin Z, Mcnamara A, Liu Y *et al*. Exfoliated hexagonal boron nitride-based polymer nanocomposite with enhanced thermal conductivity for electronic encapsulation. *Compos Sci Technol* 2014;**90**:123–128.
321. Song WL, Wang P, Cao L *et al*. Polymer/boron nitride nanocomposite materials for superior thermal transport performance. *Angew Chem Int Ed* 2012;**51**:6498–6501.
322. Cho H-B, Tokoi Y, Tanaka S *et al*. Modification of BN nanosheets and their thermal conducting properties in nanocomposite film with polysiloxane according to the orientation of BN. *Compos Sci Technol* 2011;**71**:1046–1052.
323. Yu J, Huang X, Wu C *et al*. Interfacial modification of boron nitride nanoplatelets for epoxy composites with improved thermal properties. *Polymer* 2012;**53**:471–480.
324. Wang X, Pakdel A, Zhang J *et al*. Large-surface-area BN nanosheets and their utilization in polymeric composites with improved thermal and dielectric properties. *Nanoscale Res Lett* 2012;**7**:662.
325. Zhou Q, Wu H, Li H *et al*. Barrier inhomogeneity of Schottky diode on nonpolar AlN grown by physical vapor transport. *IEEE J Electron Dev Soc* 2019;**7**:662–667.
326. Yadav SK, Wang J, Liu XY. Ab initio modeling of zincblende AlN layer in Al–AlN–TiN multilayers. *J Appl Phys* 2016;**119**:224304.
327. Carsten H, Wollweber J, Dittmar A *et al*. Preparation of bulk AlN seeds by spontaneous nucleation of freestanding crystals. *Jap J Appl Phys* 2013;**52**:08JA06.
328. Yu R, Liu G, Wang G *et al*. Ultrawide-bandgap semiconductor AlN crystals: growth and applications. *J Mater Chem C* 2021;**9**:1852–1873.
329. Zeman OEO, Moudrakovski IL, Hartmann C *et al*. Local electronic structure in AlN studied by single-crystal (27)Al and (14)N NMR and DFT calculations. *Molecules* 2020;**25**:469.
330. Zhuang D, Herro ZG, Schlesser R *et al*. Seeded growth of AlN single crystals by physical vapor transport. *J Cryst Growth* 2006;**287**:372–375.
331. Makarov YN, Avdeev OV, Barash IS *et al*. Experimental and theoretical analysis of sublimation growth of AlN bulk crystals. *J Cryst Growth* 2008;**310**:881–886.

Downloaded from https://academic.oup.com/ooms/article/2/1/itac004/6581087 by guest on 04 August 2022

332. Nagashima T, Kubota Y, Kinoshita T *et al*. Structural and optical properties of carbon-doped AlN substrates grown by hydride vapor phase epitaxy using AlN substrates prepared by physical vapor transport. *Appl Phys Exp* 2012;**5**:125501.
333. Rafael D, Craft HS, Britt J *et al*. High quality AlN single crystal Ssubstrates for AlGaN-based devices. *Mater Sci Forum* 2018; **924**:923–926.
334. Slack GA, McNelly TF *et al*. Growth of high purity MN crystals. *J Cryst Growth* 1976;**34**:263–379.
335. Hartmann C, Dittmar A, Wollweber J *et al*. Bulk AlN growth by physical vapor transport. *Semiconduct Sci Technol* 2014;**29**: 084002.
336. Sumathi RR, Gille P. Sublimation growth of c-plane AlN single crystals on SiC substrates. *Cryst Res Technol* 2012;**47**:237–246.
337. Xu X, Wu HS , Zhang CJ *et al*. Morphological properties of AlN piezoelectric thin films deposited by DC reactive magnetron sputtering. *Thin Solid Films* 2001;**388**:62–67.
338. Sumathi RR, Gille P. Development and progress in bulk c-plane AlN single-crystalline template growth for large-area native seeds. *Jap J Appl Phys* 2013;**52**:08JA02.
339. Liu L, Liu B, Edgar JH *et al*. Raman characterization and stress analysis of AlN grown on SiC by sublimation. *J Appl Phys* 2002;**92**:5183–5188.
340. Reeber RR, Wang K Thermal expansion of GaN and AlN. *Mater Res Soc* 2002;**482**:863.
341. Sumathi RR. Bulk AlN single crystal growth on foreign substrate and preparation of free-standing native seeds. *CrystEngComm* 2013;**15**:2232–2240.
342. Hu W, Guo L, Guo Y *et al*. Growing AlN crystals on SiC seeds: effects of growth temperature and seed orientation. *J Cryst Growth* 2020;**541**:125654.
343. Dalmau R, Sitar Z. AlN bulk crystal growth by physical vapor transport. *Cryst Growth Vap* 2010;**24**:821–843.
344. Lu P, Edgar JH, Cao C *et al*. Seeded growth of AlN on SiC substrates and defect characterization. *J Cryst Growth* 2008;**310**: 2464–2470.
345. Gamov I, Hartmann C, Straubinger T *et al*. Photochromism and influence of point defect charge states on optical absorption in aluminum nitride (AlN). *J Appl Phys* 2021;**129**: 113103.
346. Demir I, Li H, Robin Y *et al*. Sandwich method to grow high quality AlN by MOCVD. *J Phys D Appl Phys* 2018;**51**: 085104.
347. Yin X, Zhang Q, Zhao S. Molecular beam epitaxial growth of AlN thin films on Si through exploiting low Al adatom migration and the nitrogen-rich environment on a nanowire template. *Cryst Growth Design* 2021;**21**:3645–3649.
348. Wang W, Yang W, Liu Z *et al*. Interfacial reaction control and its mechanism of AlN epitaxial films grown on Si (111) substrates by pulsed laser deposition. *Sci Rep* 2015;**5**:11480.
349. Xiao S, Suzuki R, Miyake H *et al*. Improvement mechanism of sputtered AlN films by high-temperature annealing. *J Cryst Growth* 2018;**502**:41–44.
350. Hevia DF, Stampfl C, Viñes F *et al*. Microscopic origin ofn-type behavior in Si-doped *AlN*. *Phys Rev B* 2013;**88**:085202.
351. Ive T, Brandt O, Kostial H *et al*. Controlled n-type doping of AlN:Si films grown on 6H-SiC(0001) by plasma-assisted molecular beam epitaxy. *Appl Phys Lett* 2005;**86**:024106.
352. Kakanakova-Georgieva A, Nilsson D, Janzén E. High-quality AlN layers grown by hot-wall MOCVD at reduced temperatures. *J Crystal Growth* 2012;**338**:52–56.
353. Kim DH, Min SJ, Oh JM *et al*. Fabrication and characterization of oxygenated AlN/4H-SiC heterojunction diodes. *Materials (Basel*) 2020;**13**:4335.
354. Yusoff MZM, Mahyuddin A, Hassan Z *et al*. Plasma-assisted MBE growth of AlN/GaN/AlN heterostructures on Si (111) substrate. *Superlattice Microstruct* 2013;**60**:500–507.
355. Aissa KA, Achour A , Camus J *et al*. Comparison of the structural properties and residual stress of AlN films deposited by dc magnetron sputtering and high-power impulse magnetron sputtering at different working pressures. *Thin Solid Films* 2014;**550**:264–267.
356. Hartmann C, Matiwe L, Wollweber J *et al*. Favourable growth conditions for the preparation of bulk AlN single crystals by PVT. *CrystEngComm* 2020;**22**:1762–1768.
357. An J, Dai X, Guo R *et al*. Ab initio study for molecular-scale adsorption, decomposition and desorption on AlN surfaces during MOCVD growth. *Sci Rep* 2020;**10**:17840.
358. Chen Y, Song H, Li D *et al*. Influence of the growth temperature of AlN nucleation layer on AlN template grown by high-temperature MOCVD. *Mater Lett* 2014;**114**:26–28.
359. Irokawa Y, Víllora EAG, Shimamura K. Shottky barrier diodes on AlN free-standing substrates. *Jap J Appl Phys* 2012; **51**:040206.
360. Ben J, Sun X, Jia Y *et al*. Defect evolution in AlN templates on PVD-AlN/sapphire substrates by thermal annealing. *CrystEngComm* 2018;**20**:4623–4629.
361. Bryan I, Bryan Z, Washiyama S *et al*. Doping and compensation in Al-rich AlGaN grown on single crystal AlN and sapphire by MOCVD. *Appl Phys Lett* 2018;**112**:062102.
362. Fu H, Baranowski I, Huang X *et al*. Demonstration of AlN Schottky barrier diodes with blocking voltage Over 1 kV. *IEEE Electron Dev Lett* ;**38**:1286–1289.
363. Fu H, Huang X, Chen H *et al*. Fabrication and characterization of ultra-wide bandgap AlN-based Schottky diodes on sapphire by MOCVD. *IEEE J Electron Dev Soc* 2017;**5**:518–524.
364. He C, Zhao W, Wu H *et al*. High-quality AlN film grown on sputtered AlN/sapphire via growth-mode modification. *Cryst Growth Design* 2018;**18**:6816–6823.
365. Massimiliano B, Cannata D, Pictrantonio DF *et al*. Growth of AlN piezoelectric film on diamond for high-frequency surface acoustic wave devices. *IEEE Trans Ultrason Ferroelectr Freq Contr* 2018;**52**:1806.
366. Jackson N, Keeney L, Mathewson A. Flexible-CMOS and biocompatible piezoelectric AlN material for MEMS applications. *Smart Mater Struct* 2013;**22**:115033.
367. Jackson N, Mathewson A. Enhancing the piezoelectric properties of flexible hybrid AlN materials using semi-crystalline parylene. *Smart Mater Struct* 2017;**26**:045005.
368. Kaun SW, Wong MH, Dasgupta S *et al*. Effects of threading dislocation density on the gate leakage of AlGaN/GaN heterostructures for high electron mobility transistors. *Appl Phys Exp* 2011;**4**:024101.
369. Mino T, Hirayama H, Takano T *et al*. Characteristics of epitaxial lateral overgrowth AlN templates on (111) Si substrates for AlGaN deep-UV LEDs fabricated on different direction stripe patterns. *Phys Status Solidi (C) Curr Topics Solid State Phys* 2012;**9**:802–805.
370. Long H, Dai J, Zhang Y *et al*. High quality 10.6 μm AlN grown on pyramidal patterned sapphire substrate by MOCVD. *Appl Phys Lett* 2019;**114**:042101.
371. Washiyama S, Guan Y, Mita S *et al*. Recovery kinetics in high temperature annealed AlN heteroepitaxial films. *J Appl Phys* 2020;**127**:115301.
372. Dalmau R, Moody B, Schlesser R *et al*. Growth and characterization of AlN and AlGaN epitaxial films on AlN single crystal substrates. *J Electrochem Soc* 2011;**158**:H530–H535.

Downloaded from https://academic.oup.com/ooms/article/2/1/itac004/6581087 by guest on 04 August 2022

373. Mansurov VG, Nikitin AY, Galitsyn YG *et al*. AlN growth on sapphire substrate by ammonia MBE. *J Cryst Growth* 2007; **300**:145–150.
374. Nemoz M, Dagher R, Matta S *et al*. Dislocation densities reduction in MBE-grown AlN thin films by high-temperature annealing. *J Cryst Growth* 2017;**461**:10–15.
375. Bellucci A, Orlando S, Girolami M *et al*. Aluminum (Oxy)nitride thin films grown by fs-PLD as electron emitters for thermionic applications. In: The 1st International Conference on Innovations for Computing, Engineering and Materials, 2021, ICEM, 2021.
376. Dutheil P, Orlianges JC, Crunteanu A *et al*. AlN, ZnO thin films and AlN/ZnO or ZnO/AlN multilayer structures deposited by PLD for surface acoustic wave applications. *Phys Status Solidi (A)* 2015;**212**:817–825.
377. Basillais A, Benzerga R, Sanchez H *et al*. Improvement of the PLD process assisted by RF plasma for AlN growth. *Appl Phys A* 2005;**80**:851–859.
378. Shojiki K, Uesugi K, Kuboya S *et al*. Reduction of threading dislocation densities of N-polar face-to-face annealed sputtered AlN on sapphire. *J Cryst Growth* 2021;**574**:126309.
379. Liu Z, Guo Y, Yan J *et al*. Polarity tuning of crystalline AlN films utilizing trace oxygen involved sputtering and post-high-temperature annealing. *Appl Phys Exp* 2021;**14**:085501.
380. Son NT, Bickermann M, Janzén E. Shallow donor and DX states of Si in AlN. *Appl Phys Lett* 2011;**98**:092104.
381. Zeisel R, Bayerl MW, Gönnenwein STB *et al*. DX-behavior of Si in AlN. *Phys Rev B* 2000;**61**:24.
382. Goennenwein STB, Zeisel R, Ambacher O *et al*. Generation–recombination noise of DX centers in AlN:Si. *Appl Phys Lett* 2001;**79**:2396–2398.
383. Taniyasu Y, Kasu M, Kobayashi N. Intentional control of n-type conduction for Si-doped AlN and AlxGa1−xN ($0.42 \leqslant x < 1$). *Appl Phys Lett* 2002;**81**:1255–1257.
384. Harris JS, Baker JN, Gaddy BE *et al*. On compensation in Si-doped AlN. *Appl Phys Lett* 2018;**112**:152101.
385. Gordon L, Lyons JL, Janotti A *et al*. Hybrid functional calculations of DX centers in AlN and GaN. *Phys Rev B* 2014;**89**: 085204.
386. Breckenridge MH, Bagheri P, Guo Q *et al*. High n-type conductivity and carrier concentration in Si-implanted homoepitaxial AlN. *Appl Phys Lett* 2021;**118**:112104.
387. Neugebauer J, Van de Walle CG. Chemical trends for acceptor impurities in GaN. *J Appl Phys* 1999;**85**:3003–3005.
388. Götz W, Johnson NM, Bour DP. Deep level defects in Mg-doped, p-type GaN grown by metalorganic chemical vapor deposition. *Appl Phys Lett* 1996;**68**:3470–3472.
389. Taniyasu Y, Kasu M, Makimoto T. An aluminium nitride light-emitting diode with a wavelength of 210 nanometres. *Nature* 2006;**441**:325–328.
390. Laaksonen K, Ganchenkova MG, Nieminen RM. Vacancies in wurtzite GaN and AlN. *J Phys Condens Matter* 2009;**21**:015803.
391. Nam KB, Nakarmi ML, Li J *et al*. Mg acceptor level in AlN probed by deep ultraviolet photoluminescence. *Appl Phys Lett* 2003;**83**:878–880.
392. Ahmad H, Lindemuth J, Engel Z *et al*. Substantial p-type conductivity of AlN achieved via beryllium doping. *Adv Mater* 2021;**33**:e2104497.
393. Wahl U, David BE, Amorim LM *et al*. Lattice sites of implanted Na in GaN and AlN in comparison to other light alkalis and alkaline earths. *J Appl Phys* 2020;**128**:045703.
394. Fei C, Liu X, Zhu B *et al*. AlN piezoelectric thin films for energy harvesting and acoustic devices. *Nano Energy* 2018;**51**:146–161.
395. Guido F, Qualtieri A, Algieri L *et al*. AlN-based flexible piezoelectric skin for energy harvesting from human motion. *Microelectron Eng* 2016;**159**:174–178.
396. Sukriti M, Talley KR, Gorai P *et al*. Enhanced piezoelectric response of AlN via CrN alloying. *Phys Rev Appl* 2018;**9**:034026.
397. Qiu Y, Gigliotti JV, Wallace M *et al*. Piezoelectric micromachined ultrasound transducer (PMUT) arrays for integrated sensing, actuation and imaging. *Sensors* 2015;**15**:8020–8041.
398. Piazza G, Stephanou PJ, Pisano AP. Piezoelectric aluminum nitride vibrating contour-mode MEMS resonators. *J Microelectromech Syst* 2006;**15**:1406–1418.
399. Kinoshita T, Nagashima T, Obata T *et al*. Fabrication of vertical Schottky barrier diodes on n-type freestanding AlN substrates grown by hydride vapor phase epitaxy. *Appl Phys Exp* 2015;**8**:061003.
400. Chen H, Fu H, Zhou J *et al*. Study of crystalline defect induced optical scattering loss inside photonic waveguides in UV-visible spectral wavelengths using volume current method. *Opt Exp* 2019;**27**:27262.
401. Chen H, Zhou J, Li D *et al*. Supercontinuum generation in high order waveguide mode with near-visible pumping using aluminum nitride waveguides. *ACS Photon* 2021;**8**: 1344–1352.
402. Weber JR, Koehl WF, Varley JB *et al*. Quantum computing with defects. *Proc Natl Acad Sci USA* 2010;**107**:8513–8518.
403. Sipahigil A, Goldman ML, Togan E *et al*. Quantum interference of single photons from remote nitrogen-vacancy centers in diamond. *Phys Rev Lett* 2012;**108**:143601.
404. Xue Y, Wei T, Chang H *et al*. Experimental optical properties of single-photon emitters in aluminum nitride films. *J Phys Chem C* 2021;**125**:11043–11047.
405. Xue Y, Wang H, Xie N *et al*. Single-photon emission from point defects in aluminum nitride films. *J Phys Chem Lett* 2020;**11**:2689–2694.
406. Berhane AM, Jeong KY, Bradac C *et al*. Photophysics of GaN single-photon emitters in the visible spectral range. *Phys Rev B* 2018;**97**:165202.
407. Bishop SG, Hadden JP, Alzahrani FD *et al*. Room-temperature quantum emitter in aluminum nitride. *ACS Photon* 2020;**7**: 1636–1641.
408. Lu TJ, Lienhard B, Jeong KY *et al*. Bright high-purity quantum emitters in aluminum nitride integrated photonics. *ACS Photon* 2020;**7**:2650–2657.
409. Wan NH, Lu TJ, Chen KC *et al*. Large-scale integration of artificial atoms in hybrid photonic circuits. *Nature* 2020;**583**: 226–231.
410. Lu TJ, Fanto M, Choi H *et al*. Aluminum nitride integrated photonics platform for the ultraviolet to visible spectrum. *Opt Exp* 2018;**26**:11147–11160.
411. Kim S, Duong NMH, Nguyen M *et al*. Integrated on chip platform with quantum emitters in layered materials. *Adv Opt Mater* 2019;**7**:1901132.

Downloaded from https://academic.oup.com/ooms/article/2/1/itac004/6581087 by guest on 04 August 2022